



# MODELING AND SIMULATION OF MAGNETIC TRANSMISSION LINES

---



by

Muhammad Shamaas  
2018-MS-EE-4

Research Supervisor:  
Dr. Muhammad Asghar Saqib

2021

---

Department of Electrical Engineering  
University of Engineering and Technology, Lahore

# MODELING AND SIMULATION OF MAGNETIC TRANSMISSION LINES

by

MUHAMMAD SHAMAAS

A THESIS

presented to the university of engineering and technology, Lahore

in partial fulfillment of the requirements for the degree of

Master of Science

in

**ELECTRICAL ENGINEERING**

APPROVED BY:

---

[Primary Advisor/Internal Examiner]  
[Official Title & Department]

---

[External Examiner]  
[Official Title & Department]

---

[Chairman of the Department]

---

[Dean of Faculty]

**Approval Date**

DEPARTMENT OF ELECTRICAL ENGINEERING  
UNIVERSITY OF ENGINEERING & TECHNOLOGY, LAHORE

© 2020

Muhammad Shamaas

All Rights Reserved.

Any part of this thesis cannot be copied, reproduced or published without the written  
approval of the Scholar.

## ABSTRACT

Magnetic Transmission Line is the dual counterpart of Electric Transmission Line. Its theory encompasses a diverse range of applications including Transformers, Dynamic Machines, Microwave Generators, Tuners, Couplers, Isolators, Power Dividers etc. Intrinsically, Magnetic Transmission Line is made from a non-conducting magnetic material, with a high permeability. It transmits Magnetic Flux as the effective Magnetic charge. Time varying magnetic flux results in a Magnetic Displacement Current inside the Transmission Line. This produces a gradient Magnetic Field; with Fields Lines that spread radially outwards. The magnetic displacement current and magnetic voltage due to this Magnetic Field is measured in Volts and Amperes respectively. Although, the operation of a Magnetic Transmission Line does not involve electric charges, Magnetic Displacement Current produces an Electric Field with closed Field Lines encircling the Magnetic Transmission Line. Together, the Electric and Magnetic Fields transmit Energy along the direction of propagation. These relations were modeled using Reluctance Model, Permeance-Capacitance Model and Magnetic Transmission Line Model to study the time and frequency domain behavior of Magnetic Transmission Lines. Furthermore, Finite Difference Time Domain, Electromagnetic Field Simulations were carried out in MEEP Simulator for saturated, gyromagnetic Transmission Lines using the Linearized Landau-Lifshitz-Gilbert Model to study the effects of frequency and Gilbert damping constant on Magnetic Transmission Line parameters.

## **ACKNOWLEDGMENTS**

First of all, thanks to Allah who made it possible for me to complete this thesis. I am thankful to my supervisors Dr. Muhammad Asghar Saqib, Dr. Syed Abdul Rehman Kashif and Dr. Syed Shah Irfan Hussain whose stimulating suggestions supported me throughout the research for this thesis. I would like to give my special thanks to my teachers whose care and struggle enabled me to stay focused in my quest for knowledge. My former colleagues supported me in my research work. I want to thank them for all their help, support, interest and valuable hints. Especially I am obliged to my friends and family for their support.

## **STATEMENT OF ORIGINALITY**

It is stated that the research work presented in this thesis consists of my own ideas and research work. The contributions and ideas from others have been duly acknowledged and cited in the dissertation. This complete thesis is written by me.

**Muhammad Shamaas**

## TABLE OF CONTENTS

	Page
ABSTRACT .....	iv
ACKNOWLEDGMENTS .....	v
STATEMENT OF ORIGINALITY .....	vi
TABLE OF CONTENTS.....	vii
LIST OF FIGURES .....	ix
LIST OF TABLES .....	xii
NOMENCLATURE .....	xiii
 1. INTRODUCTION.....	 1
1.1. NATURE OF MAGNETIC MATERIALS .....	2
1.2. AC LOSSES IN MAGNETIC MATERIALS.....	16
1.3. LITERATURE REVIEW .....	21
 2. WAVE PROPAGATION IN MAGNETIC MATERIALS .....	 26
2.1. PLANE WAVE PROPAGATION .....	26
2.2. POWER FLOW ANALYSIS.....	30
 3. MAGNETIC CIRCUIT MODELING.....	 33
3.1. RELUCTANCE MODEL .....	34
3.1.1. Application.....	36
3.2. PERMEANCE-CAPACITANCE MODEL.....	42
3.2.1. Application.....	45
3.3. MAGNETIC TRANSMISSION LINE MODEL.....	58



4.	COMPUTATIONAL ELECTROMAGNETICS .....	71
4.1.	METHODS FOR SOLVING MAXWELL’S EQUATIONS .....	71
4.2.	INTRODUCTION TO FINITE DIFFERENCE TIME DOMAIN METHOD .....	75
4.3.	INTRODUCTION TO MEEP SIMULATOR .....	79
5.	MAGNETIC TRANSMISSION LINE SIMULATION.....	85
5.1.	SIMULATION OF DISPERSIVE MAGNETIC TRANSMISSION LINE .....	86
5.1.1.	Visualization Of Electromagnetic Fields.....	92
5.1.2.	Variation Of Permeability With Frequency .....	94
5.1.3.	Attenuation Of Magnetic Field Along The Direction Of Propagation .....	96
5.1.4.	Skin Effect In Magnetic Transmission Line .....	97
5.1.5.	Evolution Of Magnetic Displacement Current And Voltage.....	99
5.1.6.	Intrinsic Wave Impedance Of Magnetic Transmission Line .....	101
5.1.7.	Attenuation Constant And Phase Constant Of Magnetic Transmission Line .....	102
5.1.8.	Magnetic Admittance Of Magnetic Transmission Line .....	104
5.1.9.	Magnetic Impedance Of Magnetic Transmission Line .....	105
5.2.	SIMULATION OF GYROMAGNETIC TRANSMISSION LINE.....	106
6.	CONCLUSION .....	118
	BIBLIOGRAPHY .....	120
	APPENDICES.....	128
	APPENDIX A. MEEP CODE.....	128
	APPENDIX B. MATLAB CODE .....	138
	VITA.....	141

## LIST OF FIGURES

Figure	Page
Figure 1.1 Magnetic Transmission through Transfer of Torque .....	4
Figure 1.2 A Minimum Energy State Configurations Achieved by Cooperation of Neighboring Domains .....	6
Figure 1.3 Transition of Spin Direction at Domain Boundary .....	10
Figure 1.4 Effect of Applied Field on Magnetic Domains .....	11
Figure 1.5 Variation of Magnetic Susceptibility with Applied Magnetic Field .....	13
Figure 1.6 Hysteresis Loop for a Non-linear Ferromagnetic Material .....	14
Figure 1.7 Dielectric Circuit Model for Ferromagnetic Material.....	18
Figure 1.8 Lorentzian Resonance of Permeability .....	20
Figure 3.1 A Magnetic Core Excited by Electric Current .....	34
Figure 3.2 Reluctance Model for Magnetic Core.....	35
Figure 3.3 Model for Cumulatively Compounded DC Motor .....	36
Figure 3.4 Simulink Model for Cumulatively Compounded DC Generator .....	38
Figure 3.5 Simulink Model for Non-linear Permeance .....	39
Figure 3.6 Evolution of Field Currents, Net MMF, Generated EMF and Terminal Voltage .....	40
Figure 3.7 Variation of Terminal Voltage with Rotor Speed .....	41
Figure 3.8 Gyrator Model for Power Invariant Transformation of Electric and Magnetic Quantities.....	43
Figure 3.9 Permeance-Capacitance Model for Transformer.....	44

Figure 3.10 Electrical Circuit for Full Bridge Isolated Buck Converter .....	45
Figure 3.11 Equivalent Converter Circuit with Gytrators and Non-linear Core Permeance .....	49
Figure 3.12 Simulink Model for Non-linear Core Permeance .....	50
Figure 3.13 Variation of Permeance Flux versus Permeance Magnetic Voltage .....	51
Figure 3.14 Transformer Voltage and Current Response for Sinusoidal Excitation and Resistive Load .....	52
Figure 3.15 Simulink Model for Full Bridge Isolated Buck Converter.....	53
Figure 3.16 Simulink Model for Primary Winding Gyrator .....	54
Figure 3.17 Simulink Model for Secondary Winding Gyrator .....	54
Figure 3.18 Primary Winding Voltage and Current .....	55
Figure 3.19 Load Voltage and Current .....	56
Figure 3.20 Permeance Voltage and Current .....	57
Figure 3.21 A Section of Magnetic Transmission Line Transmitting Flux in z-direction	60
Figure 3.22 Equivalent Circuit Model for Magnetic Transmission Line .....	63
Figure 3.23 Equivalent Circuit Model for Cross-talk between Neighbouring Magnetic Transmission Lines .....	68
Figure 4.1 Location of Different Field Components in a Yee Cell .....	75
Figure 5.1 Overview of MEEP Algorithm for Simulation of Magnetic Transmission Line .....	89
Figure 5.2 Geometry of Simulated Magnetic Transmission Line and Current Source .....	91
Figure 5.3 Variation of Relative Permeability with Applied Magnetic Field Frequency .	94
Figure 5.4 Discrete Fourier Transform of Gaussian Pulse .....	95

Figure 5.5 Evolution of Pulse Wave front Across the Length of Transmission Line .....	96
Figure 5.6 A Transverse Slice of the Magnetic Transmission Line .....	97
Figure 5.7 Decay of Electromagnetic Fields inside Lossy Magnetic Material .....	98
Figure 5.8 Evolution of Magnetic Displacement Current and Magnetic Voltage upon Application of Gaussian Pulse .....	100
Figure 5.9 Variation of Wave Impedance Magnitude and Angle with Frequency .....	101
Figure 5.10 Variation of Attenuation Constant, Phase Constant and Phase Velocity with Frequency .....	102
Figure 5.11 Variation of Phase Velocity with Frequency .....	103
Figure 5.12 Variation of Magnetic Conductance, Magnetic Reluctance and Magnetic Capacitance with Frequency .....	104
Figure 5.13 Variation of Magnetic Inductance with Frequency .....	105
Figure 5.14 Ferromagnetic Resonance of Susceptibility Tensor Element $\chi_{12}$ .....	107
Figure 5.15 The $H_x$ and $H_y$ Components Precess Around the $H_z$ Bias .....	108
Figure 5.16 The Magnetic Field Polarization Changes from Linear to Circular .....	108
Figure 5.17 Fourier Transform of Gaussian Pulse .....	109
Figure 5.18 Gyromagnetic Resonance at Larmor Frequency of 30 GHz .....	110
Figure 5.19 Gyromagnetic Precession Due to Gaussian Source .....	111
Figure 5.20 Plot of Intrinsic Wave Impedance vs Gilbert Damping Constant. ....	112
Figure 5.21 Plot of Wave Attenuation Constant vs Gilbert Damping Constant .....	113
Figure 5.22 Plot of Longitudinal Magnetic Admittance vs Gilbert Damping Constant..	114
Figure 5.23 Plot of Transverse Magnetic Impedance vs Gilbert Damping Constant.....	115

## LIST OF TABLES

Table	Page
Table 3.1 Switching Table for Transistors and Diodes .....	45
Table 3.2 Design Parameters for Full Bridge Isolated Buck Converter .....	46
Table 3.3 Comparison of Electric and Magnetic Transmission Lines .....	66
Table 3.4 Comparison of Three Magnetic Circuit Models .....	69
Table 4.1 Techniques for Solving Electromagnetic Problems .....	71
Table 4.2 Conversion from SI Units to MEEP Units .....	83
Table 5.1 Longitudinal Field Components .....	92
Table 5.2 Transverse Field Components .....	93

## NOMENCLATURE

Symbol	Description
$A$	Surface area, cross section area of magnetic core
$a$	Atomic spacing
$\alpha$	Temperature exponent for susceptibility, attenuation constant
$\alpha_x, \alpha_y, \alpha_z$	Direction cosines
$B$	Magnetic flux density vector
$B_{\max}$	Magnetic saturation flux density
$b_0$	Bias vector for gyromagnetic precession
$\beta$	Temperature exponent for magnetization, phase constant
$C_T, C_L, C_{\text{filter}}$	Transverse capacitance of electric transmission line, longitudinal capacitance of magnetic transmission line, filter capacitance
$c$	Speed of light
$\chi_m$	Magnetic susceptibility
$D$	Electric flux density vector
$D$	Duty cycle
$d\mathbf{l}$	Infinitesimal length vector
$d$	Width of magnetic strip
$\Delta B$	Maximum change in magnetic flux
$\delta$	Skin depth
$E$	Electric field intensity vector
$E$	Energy, generated electromotive force

$E_M, E_{MCA},$	Magnetostatic energy, magneto-crystalline anisotropy energy,
$E_{MS}, E_{DW}$	Magnetostriction energy, domain wall energy
$e$	Electric charge
$\epsilon, \epsilon_0, \epsilon', \epsilon'',$	Electrical permittivity, electrical permittivity of free space,
$\epsilon_r, \epsilon_\infty$	real part of electrical permittivity, imaginary part of electrical permittivity, relative permittivity, permittivity at infinite frequency
$\eta, \eta_0$	Intrinsic impedance, free space intrinsic impedance
$F_{EM}, F_{loop}$	Lorentz force vector, force on current loop
$F$	Force, force between magnetic poles
$f$	Frequency
$F_m, F_{net}, F_F,$	Magnetomotive force, net magnetomotive force, shunt field
$F_F, F_{SE}, F_{AR}$	magnetomotive force, series field magnetomotive force, armature reaction magnetomotive force
$G_L$	Longitudinal conductance of magnetic transmission line
$g$	Momentum density of wave
$g_L, g_S$	Orbital angular momentum g-factor, spin angular momentum g-factor
$\gamma, \gamma_0$	Propagation constant, oscillator damping ratio at resonance frequency
$H$	Magnetization field vector
$\hbar$	Reduced Planck constant
$I$	Wave intensity
$I, I_A, I_L, I_F,$	Electric conduction current, armature current, load current, shunt

$I_F^*, I_e, I_{m,disp}$	field winding current, net field current, electric conduction current, magnetic displacement current
$J, J_{ij}, J_{bound}$	Electric conduction current density vector, Heisenberg exchange constant between two states, bound electric conduction current
$J_s$	Surface current density
$K_a$	Anisotropy constant
$k$	Voltage constant
$L$	Orbital angular momentum
$L_m, L_{filter},$	Magnetic inductance, filter inductance, transverse inductance of
$L_T, L_L$	of magnetic transmission line, longitudinal inductance of electric transmission line
$l, l_m$	Length of magnetic core, mean path length of magnetic core
$\lambda, \lambda_o, \lambda_{ms},$	Wavelength, free space wavelength, magnetostriction constant
$\lambda_p$	Flux linkage of primary winding
$m$	Magnetic dipole moment vector
$m_e$	Electron mass
$M$	Magnetization
$M_0$	Spontaneous magnetization
$\mu, \mu_B, \mu_0, \mu',$	Magnetic permeability, Bohr magneton, free space permeability, real part
$\mu'', \mu_r, \mu_\infty$	of magnetic permeability, imaginary part of magnetic permeability, relative permeability, permeability at infinite frequency
$u_o$	Free space phase velocity



$N, N_F, N_{SE}$	Gyration constant, shunt field winding turns, series field winding turns
$\hat{n}$	Surface normal vector
$\omega, \omega_m, \omega_0$	Radian frequency, rotor mechanical speed, resonance frequency
$P$	Radiation pressure, polarization vector
$p$	Momentum
$P_H, P_e, P_m,$	Hysteresis density, eddy current loss density/ electric power, magnetic
$P_{av}, P_{loss}, P$	power/ magnetic permeance, average power, dissipated power, wave power
$\Phi_m, \Phi_e, \Phi_{Pm}$	Magnetic flux, electric flux, magnetic flux stored in permeance
$\emptyset$	Phase angle of magnetic reluctance
$q$	Strength of magnetic poles
$R_F, R_A, R_S,$	Shunt field winding resistance, armature resistance, series field winding
$R_m, R_c$	resistance, magnetic reluctance, resistance of core
$r$	Distance between magnetic poles
$\rho_v, \rho_s, \rho$	Volume charge density, surface charge density, electrical resistivity
$S$	Spin angular momentum, Poynting vector
$\sigma, \sigma_s, \sigma_D,$	Electric conductivity , mechanical stress, electric conductivity
$\sigma_B, \sigma_0$	Magnetic conductivity, oscillator strength at resonance frequency
$T$	Torque vector
$T, T_c, T_s$	Temperature, Curie temperature, switching period
$\delta_d, \delta_b, \delta_H,$	Dielectric loss angle, diamagnetic loss angle, hysteresis loss angle, eddy
$\delta_E, \delta_r, \delta$	current loss angle, residual loss angle, total loss angle

$u$	Phase velocity
$v$	Velocity vector
$V_T, V_e, V_m,$	Generator terminal voltage, electrical voltage, magnetic voltage
$V_p, V_s, v_{Pm},$	voltage of primary winding, source voltage, magnetic voltage of
$V_{Diode,on}$	permeance, turn on voltage of diode
$W_H, W_e, W_m$	Hysteresis loss energy, electric energy, magnetic energy
$Z_w$	Intrinsic wave impedance

# 1. INTRODUCTION

The first chapter is dedicated to a brief review of the nature of magnetic materials and the transmission of magnetic information using magnetic dipoles. Section 1.1 presents a summary of magnetic dipoles and bulk magnetization. Section 1.2 discusses the AC properties and losses of magnetic materials [1], [2], [3]. Section 1.3 presents a literature review of magnetic transmission lines [4], [5], [6], [7], [8] with major emphasis on the recent research on giant magnetoresistance [9], magnetic capacitance [10], [11], magnetic memory [12], spintronic and nano-magnetic logic devices [13], [14], [15], [16], [17], [18], [19], [20], [21].

Magnetic transmission lines [4], [5], [6], [7], [8] are designed to transmit electromagnetic energy using strong magnetic fields. They are made of magnetic materials having very high magnetic permeability and a strong affinity for magnetic flux. When an external magnetic field is applied, magnetic dipoles react to align with it. This large scale cooperation enhances the magnetic flux density inside the magnetic material. When the applied field is varied, the changing magnetic flux density transmits the magnetic information across the magnetic material [22]. This phenomenon is called magnetic transmission [4], [5], [6], [7], [8].

It is important to note that charge transport is not involved in magnetic communication. Isolated magnetic charges do not exist and magnetic conduction current can never flow in a magnetic transmission line [4], [5], [6], [7], [8]. Magnetic transmission is only possible through the alignment of magnetic dipoles in response to a stimulating magnetomotive force. This is termed as magnetic displacement current.

Magnetic transmission does not involve the flow of electric charges either. Magnetic materials are very poor electric conductors; hence electric currents cannot transmit information across a magnetic transmission line [4], [5], [6], [7], [8]. Changing magnetic fields produce electric fields which are transmitted through electric displacement currents. This causes polarization of atoms in the dielectric [23] magnetic medium which transmits electric information across the magnetic material. Together, the electric and magnetic fields transmit electromagnetic energy along the direction of propagation [24]. The following sections will elaborate on the subject of magnetic materials. A brief account on the losses [1], [2], [3] in magnetic transmission lines [4], [5], [6], [7], [8] will be given as well.

### **1.1. NATURE OF MAGNETIC MATERIALS**

The basic building blocks of magnetic materials are fictitious magnetic monopoles which can be considered as magnetic charge carriers. In nature, magnetic monopoles always exist in pairs called magnetic dipoles. A monopole can have either positive or negative charge which is responsible for the magnetic field around it. The force between monopoles is proportional to the strength of the poles ( $q$ ) and inversely proportional to the square of distance ( $r$ ) between them; as expressed in Equation 1.1.

$$F \propto \frac{q_1 q_2}{r^2} \quad (1.1)$$

Dipoles result from the microscopic bound currents due to the electrons circulating around the nucleus. The effect of each tiny magnet is similar to the effect of a current

flowing in a loop. The identification of the north and south poles is dictated by the Flemming's right hand rule.

Whenever a moving charge  $q$  is placed in an electromagnetic field, it experiences a force called Lorentz force [24]. The direction of the force represents the direction of least pressure in the electromagnetic field. Lorentz force depends on the velocity of the charge and the strength of the electric and magnetic fields; as expressed in Equation 1.2.

$$\mathbf{F}_{EM} = e(\mathbf{E} + \mathbf{v} \times \mathbf{B}) \quad (1.2)$$

If an orbiting electron is placed in a magnetic field, the net Ampere force on the current loop is proportional to the current and magnetic field strength; as expressed in Equation 1.3.

$$\mathbf{F}_{loop} = \oint I d\mathbf{l} \times \mathbf{B} \quad (1.3)$$

The force will produce a torque which will rotate the tiny magnet in the direction of applied field resulting in the transmission of magnetic information; as shown in Figure 1.1 **Error! Reference source not found..** The torque can be represented in terms of the magnetic dipole moment normal to the current loop using Equation 1.4.

$$\mathbf{T} = \mathbf{m} \times \mathbf{B} \quad (1.4)$$

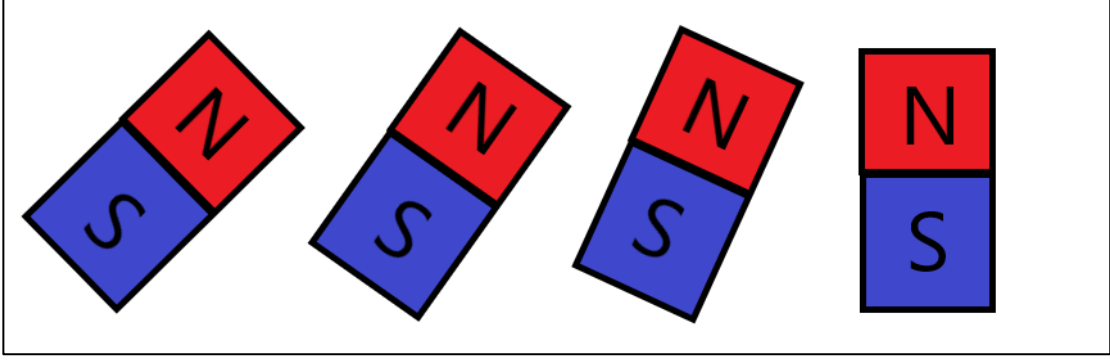


Figure 1.1 Magnetic Transmission through Transfer of Torque

The magnetic dipole moment  $\hat{\mu}$  of an orbiting/spinning electron is related to the  $g$ -factors for the spin and orbital angular momentum, the spin angular momentum operator  $\hat{\mathbf{S}}$  and the orbital angular momentum operator  $\hat{\mathbf{L}}$  [25], [18] by the relation expressed in Equation 1.5.

$$\mathbf{m} = \mu_B(g_L\mathbf{L} + g_S\mathbf{S}) \quad (1.5)$$

$$\text{where } g_L = 1, g_S = 2.0023, \mu_B = \frac{q\hbar}{2m_e}.$$

The magnetic field of the orbiting electron interacts with its spin to produce intrinsic spin-orbit interaction [18]. Hence the moment attains discrete values depending on the spin and orbital quantum numbers [14]. The net magnetic moment of an atom or ion is the vector sum of the orbital and spin moments of all electrons in its outer shell. The energy levels of

an electron split in a magnetic field due to Zeeman splitting and Heisenberg exchange interaction [18], [25] as expressed in Equation 1.6 and Equation 1.7 respectively.

$$E = -\mathbf{m} \cdot \mathbf{B} \quad (1.6)$$

$$E = -\sum_{ij} J_{ij} \mathbf{S}_i \cdot \mathbf{S}_j + \mu_B g_S \sum_j \mathbf{S}_j \cdot \mathbf{B} \quad (1.7)$$

where  $J_{ij}$  is the exchange constant between state  $i$  and  $j$ .

Two dipoles attract each other if unlike poles are close to each other. On the other hand, two dipoles repel each other if like poles are closer. Inside an unmagnetized material, the magnetic dipoles are optimally oriented hence the net torque is zero. Only a few orientations can result in a net zero torque on all the dipoles in a magnetic material. One such orientation is shown in Figure 1.2. Dipoles tend to align parallel to neighboring dipoles due to positive exchange interactions so that the lowest energy state can be achieved.

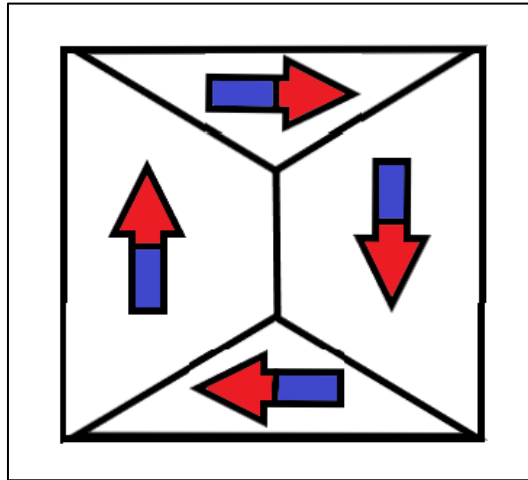


Figure 1.2 A Minimum Energy State Configurations Achieved by Cooperation of Neighboring Domains

Atoms contain orbitals with discrete levels of energy for accommodating electrons. Electrons try to occupy the lowest energy orbitals first to minimize the energy of the system. An electron with clockwise spin can pair with an electron having anticlockwise spin. Hence, the clockwise spin cancels the effect of anticlockwise spin and no magnetic moment results [18].

An external magnetic field can cause a mechanical torque on a magnetic dipole. The moment tries to turn the dipole in the direction that decreases the overall energy of the system. Only unpaired spins contribute to the net magnetic moment. The resulting spin and orbital moments add up to produce a net magnetization vector field inside the magnetic material [18]. This field is proportional to the magnetic susceptibility of the material  $\chi_m$ ; as expressed in Equation 1.8.

$$\mathbf{M} = \chi_m \mathbf{H} \quad (1.8)$$



The magnetic field inside a magnetic material can be represented by a flow of magnet field lines [22]. The number of lines passing through a region of space is called magnetic flux. It is equivalent to magnetic charge. Magnetic flux density expressed in Equation 1.9 represents the number of flux lines per unit area.

$$\mathbf{B} = \mu_0(\mathbf{H} + \mathbf{M}) \quad (1.9)$$

Iron, Nickel and Cobalt contain 4, 3 and 2 unpaired electrons per atom respectively [26]. Hence, the effect of magnetization is very strong in these special elements and their alloys. Large scale cooperation between magnetic dipoles causes an enhanced magnetic moment. Due to the high magnetic susceptibility, they are used in the production of ferromagnetic and ferrimagnetic materials [26].

The microscopic bound current responsible for producing magnetic dipoles cancels out inside a uniformly magnetized material. A net bound current flows at the surface of the material. If the magnetization is non-uniform, the bound current will be non-zero inside the material as well. The relation between the bound current, magnetization and magnetic field is expressed in Equation 1.10 and Equation 1.11.

$$\mathbf{J}_{bound} = \nabla \times \mathbf{M} \quad (1.10)$$

$$\nabla \cdot \mathbf{H} = -\nabla \cdot \mathbf{M} \quad (1.11)$$

The parallel alignment of magnetic dipoles causes the creation of magnetic domains [27] to reduce the magnetic potential energy stored in the magnetic flux lines. The magnetic energy consists of magnetostatic energy, magneto-crystalline anisotropy energy, magnetostrictive energy and domain wall energy.

The magnetostatic energy needed to place the magnetic poles in a specific geometric configuration e.g. magnetized state [27] is proportional to the width of the magnetic strip ( $d$ ) and the value of applied magnetic field intensity ( $H$ ); as expressed in Equation 1.12. Transformers are made using insulated sheets of steel having high electrical resistance [28], [27]. Rolling of the sheets aligns the magnetic domains and reduces the magnetostatic energy [27].

$$E_M \propto H^2 d \quad (1.12)$$

For crystalline structures with repeating atomic units, the domain magnetization tends to align along one direction more easily than other directions. Magneto-crystalline anisotropy energy is greater in hard direction as compared to the easy direction [27]. It depends on the anisotropy constants ( $K_a$ ) and direction cosines ( $\alpha_i$ ) which project magnetization on the different axes; as expressed in Equation 1.13.

$$E_{MCA} = K_a (\alpha_x \alpha_y + \alpha_y \alpha_z + \alpha_z \alpha_x) \quad (1.13)$$

Magnetization and demagnetization can cause changes in the dimensions of the magnetic materials [27]. These stresses are caused by shifting of atomic planes e.g. during alignment of domains. Magnetostrictive energy represents the elastic potential energy stored in the constricted atomic configuration. As expressed in Equation 1.14, it is proportional to the magnetostriction constant  $\lambda_{ms}$  and applied stress  $\sigma_s$ .

$$E_{MS} \propto \frac{3}{2} \lambda_{ms} \sigma_s \quad (1.14)$$

A domain wall is a region where the magnetization in one domain gradually changes to the direction of a neighboring domain [27]; as in Figure 1.3. domain wall energy represents the energy in the transition region. It is related to anisotropy constant ( $K_a$ ), Curie point ( $T_c$ ) and atomic spacing ( $a$ ) by the relation in Equation 1.15.

$$E_{DW} \propto \sqrt{\frac{K_a T_c}{a}} \quad (1.15)$$

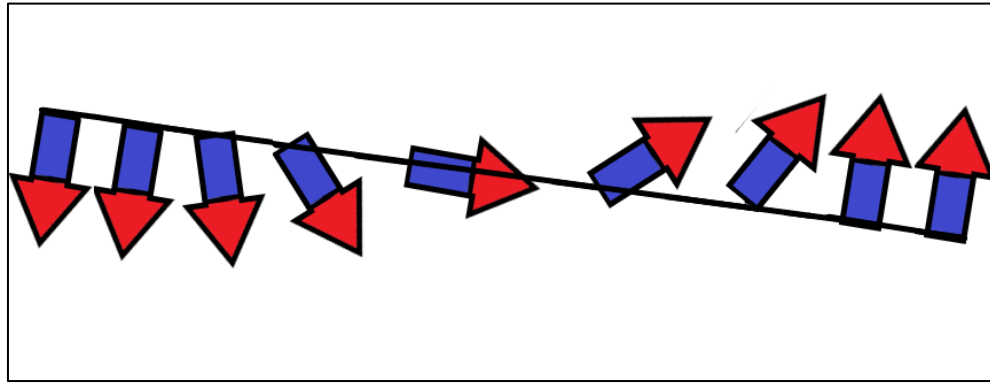


Figure 1.3 Tansition of Spin Direction at Domain Boundary

Naturally, the size and direction of magnetic domains [27] is chosen to minimize the overall magnetic energy of the system. If an unmagnetized material is placed in an external magnetic field, the domains may have to align in a hard direction for magnetization of the material. Work will be done to align the domains in the special configuration so that the preferable domains grow in size while the unfavorable domains shrink. This will involve displacement of atomic planes and domain boundaries. Hence the overall stored magnetic energy of the system will increase during magnetization [27].

When a demagnetized material is placed in an increasing Magnetic Field, the domain walls will start reversible movements and rotations. The Magnetization will start to increase slowly as shown in the Figure 1.4 below. This corresponds to the elastic phase with minimum magnetic susceptibility. Later on, the domain wall motions increase greatly. Large scale irreversible atomic plane displacements correspond to the partial magnetism phase in magnetization curve. During this phase, the material exhibits the highest magnetic susceptibility. Soon the majority of domains get aligned with the magnetic field. In the last phase, a large amount of energy is needed to rotate the remaining domain magnetization

hence the material exhibits a saturating magnetic susceptibility. At high fields, the magnetic flux density saturates at  $B_{\text{max}}$ .

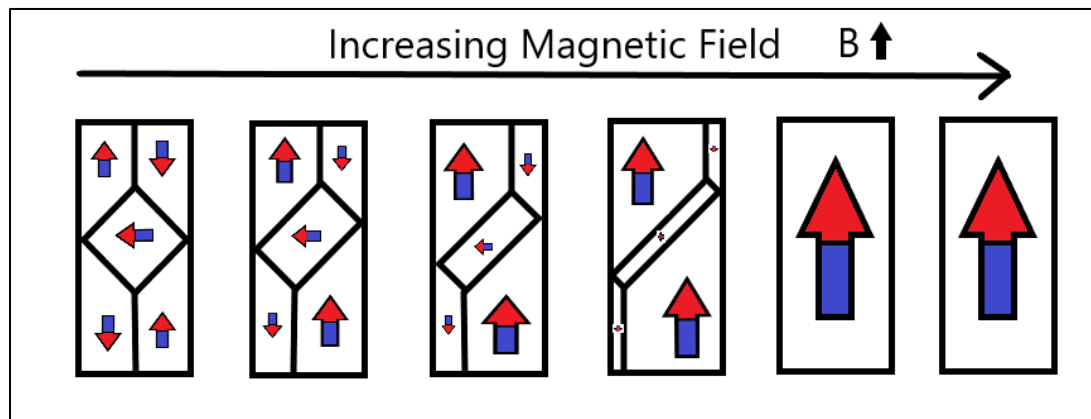


Figure 1.4 Effect of Applied Field on Magnetic Domains

If the applied field of the saturated material is decreased, the magnetic domains start to reverse their direction [27]. Initially, the material exhibits a small magnetic susceptibility. This resistance results because the majority of domains are aligned in the easy direction. The favorable domains had shrunk during the magnetization. Work must be done to expand the favorable domain walls in the reverse direction. As a result, demagnetization does not follow the curve of the original magnetization. When the applied field is decreased further, the magnetic susceptibility of the material starts to increase as more domains start to align in the reverse direction [29].

The induction lags the applied field hence some remnant induction remains when applied field is reduced to zero. In order to demagnetize the material, some extra amount

must be applied. This amount is called the coercive force. As the field keeps decreasing, the domains start aligning in the hard direction. Once all the domains have aligned, the material saturates in the reverse direction.

If the material is now magnetized again, the response will contain all the phases described earlier. The induced field will start to increase slowly, followed by a phase of large magnetic susceptibility and end by saturating.

Hysteresis [30], [31], [32] can also be experienced in a single domain particle as dictated by the Stoner-Wohlfarth model [29], [33]. In actual anisotropic materials, susceptibility is represented by a tensor [33]. When a ferromagnetic material is magnetized, the susceptibility follows the blue curve. In order to reduce its magnetization to zero, the applied field is decreased. The anisotropic behavior can explain the hysteresis in ferromagnetic materials.

When the material is saturated, the magnetic susceptibility becomes zero; as shown in Figure 1.5. Hence the permeability reduces to  $\mu_0$ . Besides magnetic field intensity, permeability is strongly dependent on chemical composition, crystal structure, stress, temperature and time after magnetization [29].

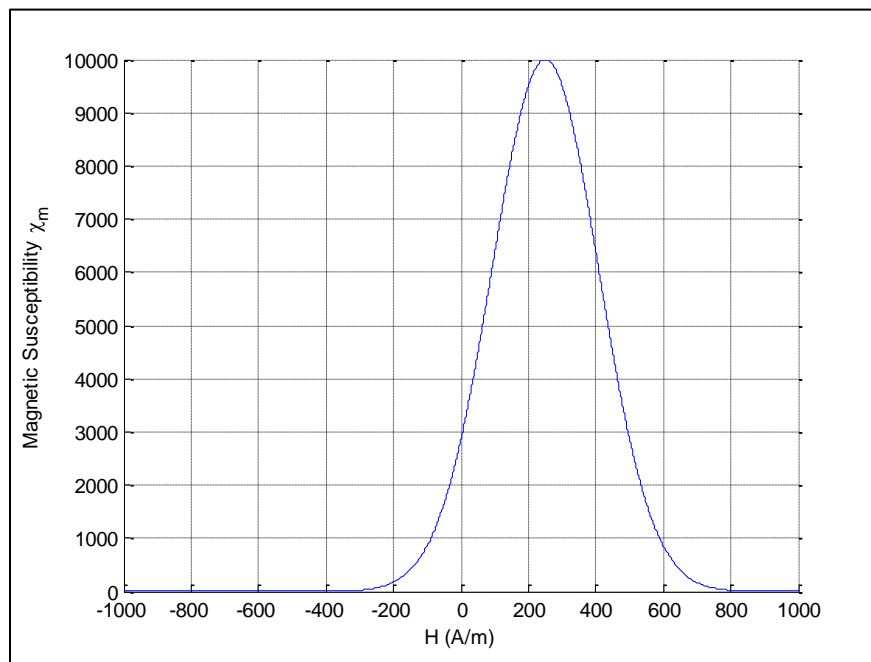


Figure 1.5 Variation of Magnetic Susceptibility with Applied Magnetic Field

A characteristic hysteresis loop is shown in Figure 1.6.

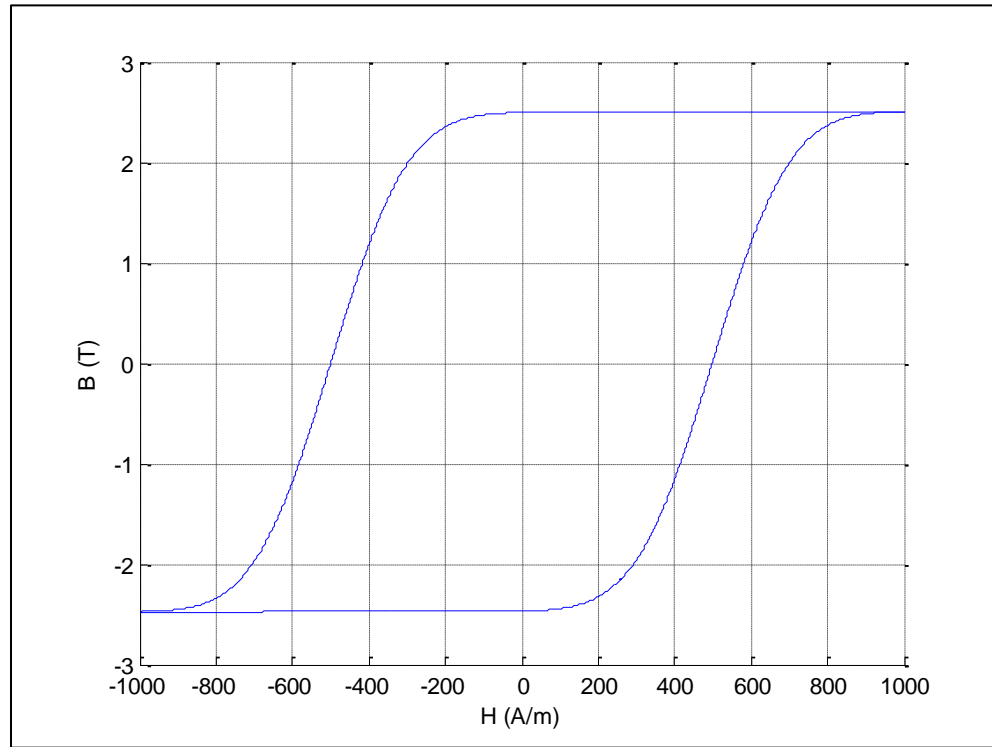


Figure 1.6 Hysteresis Loop for a Non-linear Ferromagnetic Material

The slope of the B-H curve is called permeability [29]. It is closely related to the magnetic susceptibility  $\chi_m$ ; as expressed in Equation 1.16.

$$\mu = \frac{B}{H} = \mu_0(1 + \chi_m) \quad (1.16)$$



According to the Curie Weiss law [25], the susceptibility decreases rapidly when the temperature is increased beyond the Curie temperature  $T_c$ , and the ferromagnet becomes a paramagnet. The relation is expressed in Equation 1.17.

$$\chi_m \propto \frac{1}{T - T_c} \quad (1.17)$$

According to the Landau mean-field theory for ferromagnetism [34], [25], the magnetization is related to temperature by Equation 1.18.

$$M \propto \sqrt{(T_c - T)} \quad (1.18)$$

The spin wave theory of Felix Bloch [18], [25] states that magnons carry quantized energy and momentum at  $T > 0$  K. Each magnon has spin  $\hbar$ . Their exchange interactions are responsible for the delocalized spin transitions inside the ferromagnet which reduce the magnetization from the maximum value  $\lim_{T \rightarrow 0 K} M = M_0$ . The Bloch relation for the magnetization is given in Equation 1.19.

$$M = M_0 \left( 1 - \sqrt{\frac{3}{2}} \sqrt{\frac{T}{T_c}} \right) \quad (1.19)$$

The experimental results deviate from the theoretical formulas near the Curie temperature. From experiments, it has been concluded that ferromagnetic materials have

exponential relations for susceptibility and magnetization near Curie temperature [18], [25]; as expressed in Equation 1.20 and Equation 1.21 respectively.

$$\chi_m \propto \frac{1}{(T - T_c)^\alpha} \quad (1.20)$$

$$M \propto (T - T_c)^\beta \quad (1.21)$$

## 1.2. AC LOSSES IN MAGNETIC MATERIALS

After the brief introduction of magnetic transmission in the last section, this section will explain the different mechanisms of AC losses [1], [2], [3] in ferromagnetic materials.

The cyclic magnetization of a magnetic material causes many energy losses [1], [2], [29]. The atomic plane displacements and domain wall rotations cause mechanical losses in the material. Induced voltages cause circulating currents and electrical losses. At microwave frequencies, magnetic resonance and complex permeability [35], [36], [29], [1], [2], [37], [38] can cause a significant increase in the losses [1], [2]. The various loss mechanisms [3] are hysteresis loss, eddy current loss and residual loss.

During the traversal of magnetization loop, energy is lost as heat during irreversible domain changes [29], [1], [2], [33], [30], [31], [32]. The permeability changes with position, the applied field strength, time after demagnetization, frequency and temperature [1], [2], [29], [3], [30], [31], [32]. Fields inside anisotropic media can be represented by a 3×3 permeability/ magnetic susceptibility tensor [29] as in Equation 1.22.

$$\begin{bmatrix} \mathbf{B}_x \\ \mathbf{B}_y \\ \mathbf{B}_z \end{bmatrix} = \begin{bmatrix} \mu_{xx} & \mu_{xy} & \mu_{xz} \\ \mu_{yx} & \mu_{yy} & \mu_{yz} \\ \mu_{zx} & \mu_{zy} & \mu_{zz} \end{bmatrix} \begin{bmatrix} \mathbf{H}_x \\ \mathbf{H}_y \\ \mathbf{H}_z \end{bmatrix} \quad (1.22)$$

This hysteresis loss [30], [31], [32] is equal to the area inside the DC hysteresis loop [33], [29] as expressed in Equation 1.23.

$$W_H = \int \mathbf{B} \, d\mathbf{H} \quad (1.23)$$

Hysteresis loss increases with the applied field strength and frequency [29], [3], [30], [31], [32]. The empirical formula for hysteresis loss density [33] is expressed in Equation 1.24.

$$P_H \propto B_{max}^n f \quad (1.24)$$

Ferromagnetic materials are semiconductors with resistivity ( $\rho$ ) ranging from  $0.1\Omega\text{m}$  to greater than  $1\text{M}\Omega\text{m}$ . The associated permittivity causes dielectric losses [23], [1], [2]. Whenever a changing electromagnetic field is impressed induced voltages are developed in the material [24]. These generate circulating eddy currents in the material and produce ohmic losses [3], [1], [2], [29]. These losses can be reduced by using thin laminated magnetic films or magnetic grains for manufacturing. The eddy current losses

[1], [2], [3] depend on the frequency, the applied field intensity and the conductivity ( $\sigma = \frac{1}{\rho}$ ) [29]. The empirical formula for eddy current loss density is expressed in Equation 1.25.

$$P_e \propto \frac{(B_{max}f)^2}{\rho} \quad (1.25)$$

The equivalent circuit model for the ferromagnetic material is shown in Figure 1.7. The dielectric nature can be expressed using a parasitic resistance and capacitance.

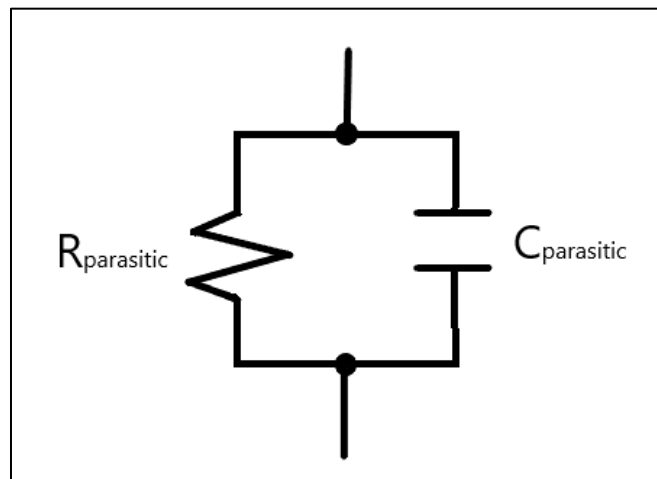


Figure 1.7 Dielectric Circuit Model for Ferromagnetic Material

The Eddy Current Losses [3] can be enhanced at high frequencies due to dimensional resonance [37], [22], [1], [2]. If a dimension of the magnetic material is equal to a quarter multiple of the electromagnetic wavelength, a standing wave can develop inside it. Under this condition, the in-phase flux cancels the anti-phase flux so the observed permittivity and permeability drops to zero [24]. The resulting eddy current loss shows a peak during resonance [29], [37]. We can represent complex permittivity and complex permeability [35], [36] as in Equation 1.26 and 1.27 respectively.

$$\varepsilon = \varepsilon_0(\varepsilon' - j(\varepsilon'' + \frac{\sigma}{\omega})) \quad (1.26)$$

$$\mu = \mu_0(\mu' - j\mu'') \quad (1.27)$$

The real part is responsible for the displacement current, whereas the imaginary part contributes to the conduction current. During dimensional resonance [37], the electric conductance of the magnetic material increases greatly. Hence the material acts like an electric conductor with a very low resistivity [29]. Although magnetic conduction currents do not exist, magnetic displacement currents can flow inside a magnetic material [22]. When the real permeability drops, the magnetic displacement currents are restricted and the magnetic susceptibility falls. This causes failure of the magnetic system. The associated loss tangents are expressed in Equation 1.28 and Equation 1.29.

$$\tan\delta_d = \frac{\varepsilon''}{\varepsilon'} \quad (1.28)$$

$$\tan\delta_b = \frac{\mu''}{\mu'} \quad (1.29)$$

The permeability is generally a complex function of frequency as expressed in Figure 1.8. During Lorentzian resonance, the imaginary part becomes very high and the magnetic losses increase greatly.

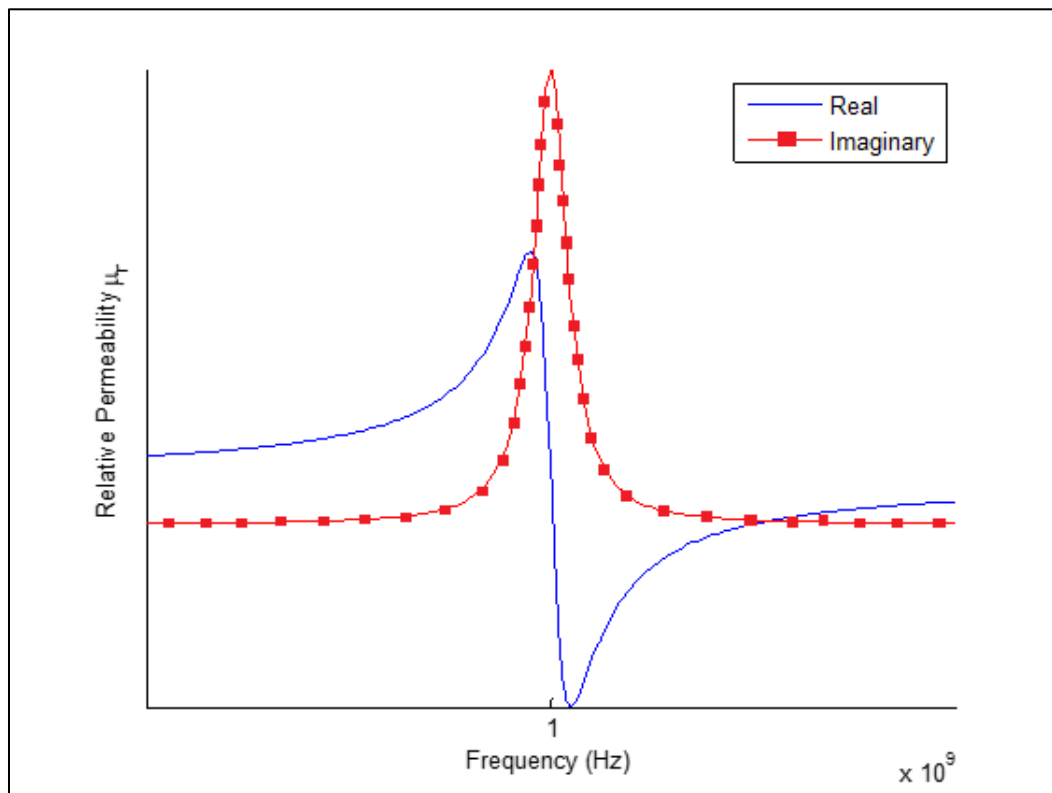


Figure 1.8 Lorentzian Resonance of Permeability

Besides hysteresis loss [33], [30], [31], [32] and eddy current loss, several processes can contribute to losses [1], [2], [22], [3] when the eddy currents are negligible and the applied flux density is extremely small. These stray losses [39] are independent of the flux density but they increase with frequency [29]. The associated loss tangent is  $\tan\delta_r$ . The total loss tangent due to hysteresis loss [33], [30], [31], [32], eddy current loss and residual loss [39], [3] is expressed in Equation 1.30.

$$\tan\delta = \tan\delta_H + \tan\delta_E + \tan\delta_r \quad (1.30)$$

In conclusion, the losses due to hysteresis [33], [30], [31], [32], eddy currents [1], [2], piezomagnetism [1], [2], magnetoresistance [9], magnetostriction [1], [2] and other residual loss mechanisms [39], [3] can be expressed as heat losses across an effective resistance or conductance.

### 1.3. LITERATURE REVIEW

This section presents a literature review of magnetic transmission lines [4], [5], [6], [7], [8] in context of the recent research on giant magnetoresistance [9], magnetic capacitance [10], [11], magnetic memory [12], spintronic and nano-magnetic logic devices [13], [14], [15], [16], [17], [18], [19], [20].

Faria [4], [5], [6], [7], [8] presented a time and frequency domain theory of multi-wire magnetic transmission lines based on the matrix theory of multi-conductor electric transmission lines [40]. For magnetic transmission lines, transverse impedance and the longitudinal admittance determine the propagation constants for the wave modes [4], [5],

[6], [7], [8]. Simulations showed that they exhibit super-luminal phase velocity and almost zero attenuation dispersion [35], [38]. He also established a relationship between voltages and currents at the multi-conductor transmission line ports by employing the transmission matrix techniques. Mathematical models were developed for studying the frequency domain behavior of non-uniform magnetic transmission lines [4], [5], [6], [7], [8]. Solutions to electromagnetic equations were presented in the form of a superposition of natural modes of propagation [24]. The magnetic transmission line exhibited the behavior of a high pass filter, blocking all DC signals. DC signals produce the most severe transients in electric transmission lines [41]; which behave like a low pass filter. Moreover, he developed a model for ideal transformers using magnetic transmission line theory [4], [5], [6], [7], [8], [42].

Antonini [43] presented an in-depth analysis of meta-material transmission lines [42]. The ladder network structure of the transmission line was used to obtain dominant zeros and poles. This lead to a rational form of the two port network transfer function. The rational form of the transfer functions provided an efficient time-domain macro model; which accurately captured the physics of composite meta-material transmission lines [43], [42].

Caloz and Itoh [44] also presented non-linear [45] electromagnetic meta-material transmission lines [42] focusing on their complex permittivity and permeability [35]. They used the transmission matrix method to formulate equations for the dispersive [35], [38], distributed non-linear system [45], [46]. These results are very useful in understanding the complex dispersive [35] and radiative nature of magnetic transmission lines [4], [5], [6], [7], [8].



Edwards and Steer [18] compared Copper, ferrite meta-conductor and magnetized Permalloy meta-conductor based coplanar waveguides. Magnetized ferrite layer provided some skin effect suppression compared to Copper waveguide; however, Permalloy provided the most uniform current profile. Some applications of ferrite materials are high frequency phase shifters, circulators and isolators [26], [47], [27]. Phase shifters used in test and measurement systems can be controlled using the bias magnetic field. Electronically controlled phase shifters are used in phase array antennas for steering antenna beam in space. Microwave circulators [29] use ferrites to separate received and transmitted waves in radar systems [47], [38], [26]. Magnetized films also act as radio frequency selective limiters. Microwave ferrite isolators are used for unidirectional transmission in plasma systems [48], [38], [27]. Their blocking capability protects precious microwave sources [49].

Neuber et al. [38], [28] presented gyromagnetic non-linear transmission lines [34], [50], [51] constructed out of Nickel-Zinc (NiZn), Magnesium-Zinc (MgZn), Manganese-Zinc (MnZn) and Yttrium Iron garnet (YIG) ferrites [29], [26], [47], [27]. Biased anisotropic magnetic transmission lines [4], [5], [6], [7], [8] functioned as microwave sources [49] because of gyromagnetic precession [51], [34], [50], [49]. Their performance strongly depended on magnetic saturation experienced at high biasing field strengths.

Paul [52] has presented time domain and frequency domain lumped inductive-capacitive coupling circuits [53], [54] for cross talk between different electric transmission line conductors. The generator-receptor model is well suited for studying radiated/conducted emissions and susceptibility. Such models must be developed for magnetic

transmission lines [4], [5], [6], [7], [8] as well; to study their electromagnetic interference and electromagnetic compatibility [24].

Paul, Whites and Nasar [24] have presented a step-by-step method to solve the Maxwell's equations in sinusoidal steady state; due to a given current distribution in a homogeneous, linear, isotropic medium. First, magnetic potential field is calculated at all desired points in space, due to the current distribution. The curl of the magnetic potential field is used to obtain the magnetic field. The divergence of the magnetic potential field is used to obtain the scalar electric potential. In turn, the magnetic potential field and the gradient of the electric potential are used to derive the Electric field. The procedure is much more complicated for waveguides in inhomogeneous, anisotropic, and non-linear media [45], [46]; hence, numerical methods [55] are suggested where a closed form solution is not possible.

Er-Ping [55] has discussed a wide range of standard time and frequency domain computational electromagnetics [56], [37], [55] methodologies. Time domain methods [53] include analytical methods, finite difference methods (FDTD) [57], [58], [41], finite integral methods (FIT), finite volume methods (FVTD), fast multipole method (FMM), partial element equivalent circuit method (PEEC), transmission line method (TLM) [58] etc. Frequency domain methods include method of moments (MoM), finite element method (FEM), geometric theory of diffraction (GTD), physical theory of diffraction (PTD) etc. He compared finite difference methods, method of moments and finite element method, in respect of principle, geometry materials, meshing, matrix equation and boundary treatment. He gave a list of commercially available simulators along with some common applications like high-speed electronics [29], photonics [37], [18], microwave circuits [38], integrated

circuits and antennas. The finite difference method can obtain response over a broad band of frequencies for many non-linear [45], [46] and inhomogeneous media without using matrix equations [41], [58]. This method is well suited for simulation of dispersive [35], [38], non-uniform magnetic transmission lines [4], [5], [6], [7], [8].

This chapter discussed the nature of magnetic materials and the transmission of magnetic information using magnetic dipoles and bulk magnetization. The AC losses [3] of magnetic materials include hysteresis losses [33], [30], [31], [32], eddy current losses and residual losses [39] due to complex permeability and permittivity [1], [2], [35], [36]. A literature review of magnetic transmission lines [4], [5], [6], [7], [8] in context of recent research on ferromagnetic modeling and simulation [54].

Chapter 2 will discuss the propagation of electromagnetic waves in anisotropic, inhomogeneous, dispersive [35], [30], [31], [32], [38] ferromagnetic materials as dictated by the Maxwell's equations [24].

Chapter 3 presents three different models for ferromagnetic materials: reluctance model [44], permeance-capacitance model [11], [30], [31], [32], [59], [60], [61] and the magnetic transmission line model [4], [5], [6], [7], [8].

Chapter 4 is dedicated to computational electrodynamics [55] i.e. the low frequency and high frequency methods for solving Maxwell's equations [24]. An overview of finite difference time domain method [62], [63], [57], [58], [53], [41] is presented which solves partial differential equation using leapfrog method. The MEEP [64] simulator uses this method for evolving electromagnetic fields in anisotropic, inhomogeneous, dispersive [35], [38] ferromagnetic materials.

## 2. WAVE PROPAGATION IN MAGNETIC MATERIALS

This chapter will discuss the propagation of electromagnetic waves in anisotropic, inhomogeneous, dispersive [35], [38] ferromagnetic materials as dictated by the Maxwell's equations [24]. Section 2.1 discusses plane wave propagation in ferromagnetic materials. Section 2.2 is devoted to the power flow analysis of electromagnetic waves travelling through magnetic materials.

### 2.1. PLANE WAVE PROPAGATION

Ideal magnetic transmission lines [4], [5], [6], [7], [8] can be modeled as linear, isotropic, homogeneous media which follow Maxwell's equations [24]. Ampere's Law [24] is expressed in Equation 2.1; Faraday's Law [24] is expressed in Equation 2.2; while Gauss' Laws [24] are expressed in Equation 2.3 and Equation 2.4.

$$\nabla \times \mathbf{H} = \sigma \mathbf{E} + \frac{d\mathbf{D}}{dt} \quad (2.1)$$

$$\nabla \times \mathbf{E} = -\mu_0 \frac{d\mathbf{B}}{dt} \quad (2.2)$$

$$\nabla \cdot \mathbf{D} = \rho_v \quad (2.3)$$

$$\nabla \cdot \mathbf{B} = 0 \quad (2.4)$$

At the boundary, the perpendicular components of  $\mathbf{B}$  and  $\mathbf{D}$  follow the relation in Equation 2.5; while the parallel components of  $\mathbf{H}$  and  $\mathbf{E}$  follow the relation in Equation 2.6.

$$B_{\perp 1} = B_{\perp 2} \text{ and } D_{\perp 1} - D_{\perp 2} = \rho_s \quad (2.5)$$

$$H_{\parallel 1} - H_{\parallel 2} = J_s \text{ and } E_{\parallel 1} = E_{\parallel 2} \quad (2.6)$$

The solution of Maxwell's equations is given by the Helmholtz equations [24] expressed in Equation 2.7 and Equation 2.8.

$$\nabla \times \nabla \times \mathbf{E} = -\frac{\partial(\nabla \times \mathbf{B})}{\partial t} = \mu\sigma \frac{\partial \mathbf{E}}{\partial t} + \mu\epsilon \frac{\partial^2 \mathbf{E}}{\partial t^2} \quad (2.7)$$

$$\nabla \times \nabla \times \mathbf{H} = \sigma(\nabla \times \mathbf{E}) + \frac{\partial(\nabla \times \mathbf{D})}{\partial t} = \mu\sigma \frac{\partial \mathbf{H}}{\partial t} + \mu\epsilon \frac{\partial^2 \mathbf{H}}{\partial t^2} \quad (2.8)$$

For sinusoidal steady state, Equation 2.7 and Equation 2.8 can be simplified and expressed compactly as in Equation 2.9 and Equation 2.10. The wave propagation constant is expressed in Equation 2.11.

$$\nabla^2 \mathbf{E} = \gamma^2 \mathbf{E} \quad (2.9)$$

$$\nabla^2 \mathbf{H} = \gamma^2 \mathbf{H} \quad (2.10)$$

$$\gamma = \sqrt{j\omega\mu\sigma - \omega^2\mu\varepsilon} = \alpha + j\beta \quad (2.11)$$

The propagation constant ( $\gamma$ ) dictates the wave propagation in the medium. The attenuation constant ( $\alpha$ ) represents the loss or attenuation of fields. The skin depth ( $\delta$ ) is defined in Equation 2.12. It is the penetration measured from the surface at which the amplitude reduces by a factor of  $1/e$ .

$$\delta = \frac{1}{\alpha} = \sqrt{\frac{2}{\omega\mu\sigma}} \quad (2.12)$$

The phase constant  $\beta$  dictates the phase velocity and wavelength. The relations are expressed in Equation 2.13 and Equation 2.14 respectively.

$$u = \frac{\omega}{\beta} \quad (2.13)$$

$$\lambda = \frac{2\pi}{\beta} \quad (2.14)$$

The ratio of matching electric field intensity  $\mathbf{E}$  and magnetic field intensity  $\mathbf{H}$  determines the intrinsic impedance of the material. The solution is expressed in Equation 2.15.

$$\eta = \frac{j\omega\mu}{\gamma} = \sqrt{\frac{j\omega\mu}{\sigma_e + j\omega\epsilon}} \quad (2.15)$$

For lossless magnetic materials with very small  $\sigma_e$ , the phase constant, phase velocity wavelength and intrinsic impedance can be expressed using Equation 2.16, Equation 2.17, Equation 2.18 and Equation 2.19 respectively.

$$\beta \approx \beta_o \sqrt{\mu_r \epsilon_r} \quad (2.16)$$

$$u \approx \frac{u_o}{\sqrt{\mu_r \epsilon_r}} \quad (2.17)$$

$$\lambda \approx \frac{\lambda_o}{\sqrt{\mu_r \epsilon_r}} \quad (2.18)$$

$$\eta \approx \eta_o \sqrt{\frac{\mu_r}{\epsilon_r}} \quad (2.19)$$

where  $\beta_o$ ,  $u_o$ ,  $\lambda_o$  and  $\eta_o$  represent the free space phase constant, phase velocity wavelength and intrinsic impedance respectively.

Considering plane wave propagation in the  $z$  direction, the solution for the electric and magnetic field is expressed in Equation 2.20 and Equation 2.21 respectively.

$$E_x(z) = E_m^+ e^{-\alpha z - j\beta z + j\theta^+} + E_m^- e^{\alpha z + j\beta z + j\theta^-} \quad (2.20)$$

$$H_y(z) = \frac{E_m^+}{\eta} e^{-\alpha z - j\beta z + j\theta^+ - j\theta_\eta} - \frac{E_m^-}{\eta} e^{\alpha z + j\beta z + j\theta^- - j\theta_\eta} \quad (2.21)$$

## 2.2. POWER FLOW ANALYSIS

The power flow density of an electromagnetic wave is given by the Poynting vector  $\mathbf{S}$ . It has the units of  $\text{W/m}^2$ . The Poynting flux is indicative of the amount of power flowing across a surface as expressed in Equation 2.22 and Equation 2.23.

$$\oint \mathbf{S} \cdot \hat{\mathbf{n}} dS = \int (\mathbf{E} \times \mathbf{H}) dS \quad (2.22)$$

$$\oint \mathbf{S} \cdot \hat{\mathbf{n}} dS = \nabla \cdot (\mathbf{E} \times \mathbf{H}) \quad (2.23)$$

The expression can be expanded as in Equation 2.24 and Equation 2.25.

$$\nabla \cdot (\mathbf{E} \times \mathbf{H}) = -\mathbf{E} \cdot (\nabla \times \mathbf{H}) + \mathbf{H} \cdot (\nabla \times \mathbf{E}) \quad (2.24)$$

$$\nabla \cdot (\mathbf{E} \times \mathbf{H}) = -\mathbf{E} \cdot \left( \mathbf{J} + \frac{\partial \mathbf{D}}{\partial t} \right) + \mathbf{H} \cdot \left( -\frac{\partial \mathbf{B}}{\partial t} \right) \quad (2.25)$$



The flow of Poynting flux can be separated into the ohmic power dissipation, electric power flow and magnetic power flow; as in Equation 2.26.

$$-\oint \mathbf{S} dS = \frac{1}{2} \int \mathbf{E} \cdot \mathbf{J} dV + \int \mathbf{E} \cdot \frac{\partial \mathbf{D}}{\partial t} dV + \int \mathbf{H} \cdot \frac{\partial \mathbf{B}}{\partial t} dV \quad (2.26)$$

From these expressions, it is clear that the electric energy and magnetic energy of a system can be expressed as in Equation 2.27 and Equation 2.28 respectively.

$$W_e = \int \mathbf{D} \cdot \mathbf{E} dV \quad (2.27)$$

$$W_m = \int \mathbf{B} \cdot \mathbf{H} dV \quad (2.28)$$

The average power transported per unit area is the intensity of the electromagnetic wave. It is expressed as the average Poynting vector in Equation 2.29.

$$\mathbf{I} = \langle \mathbf{S} \rangle \quad (2.29)$$

Electromagnetic waves also carry momentum and the momentum density stored in the fields is expressed in Equation 2.30.

$$\mathbf{g} = \frac{1}{c^2} \mathbf{S} \quad (2.30)$$

The momentum transferred to a surface results in a radiation pressure expressed in Equation 2.31.

$$\mathbf{P} = \frac{F}{A} = \frac{1}{A} \frac{\Delta p}{\Delta t} = \frac{1}{A} \frac{\langle \mathbf{g} \rangle A c \Delta t}{\Delta t} = \langle \mathbf{g} \rangle A c \quad (2.31)$$

This chapter was dedicated to the propagation of electromagnetic waves in anisotropic, inhomogeneous, dispersive [35], [38] ferromagnetic materials as dictated by the Maxwell's equations [24], and the power flow analysis of electromagnetic waves travelling through magnetic materials. The next chapter will focus on the magnetic circuit modeling for ferromagnetic materials.

### 3. MAGNETIC CIRCUIT MODELING

In this chapter, three different magnetic circuit models for the magnetic core shown in Figure 3.1 will be presented: The reluctance model [44], The permeance-capacitance model [11], [30], [31], [32], [59], [60], [61] and the magnetic transmission line model [4], [5], [6], [7], [8]. It is understood that magnetic monopoles do not exist and magnetic conduction current cannot flow. Any reference to the flow of magnetic current is meant to indicate the flow of magnetic displacement current i.e. the rate of change of magnetic flux.

The reluctance model [44] is the oldest and most popular model, even though it is not a power invariant model [65]. It only has one component called the magnetic reluctance which resists the flow of magnetic flux [44]. The model does not have energy storage elements.

The permeance-capacitance model [11], [30], [31], [32], [59], [65], [60], [61] overcomes the weaknesses of the reluctance model [44] by considering the rate of change of magnetic flux as the magnetic displacement current. It is a power invariant model [65] because it correctly encompasses the transformation of magnetic and electric energy [59]. This model has the shortcoming that it does not incorporate electric energy storage in a magnetic material [1], [2], [3].

The magnetic transmission line [4], [5], [6], [7], [8] model improves the permeance-capacitance model [11], [30], [31], [32], [59], [60], [61], [65] by including a component for electric energy storage and a component for magnetization, polarization and conduction losses [1], [2], [3].

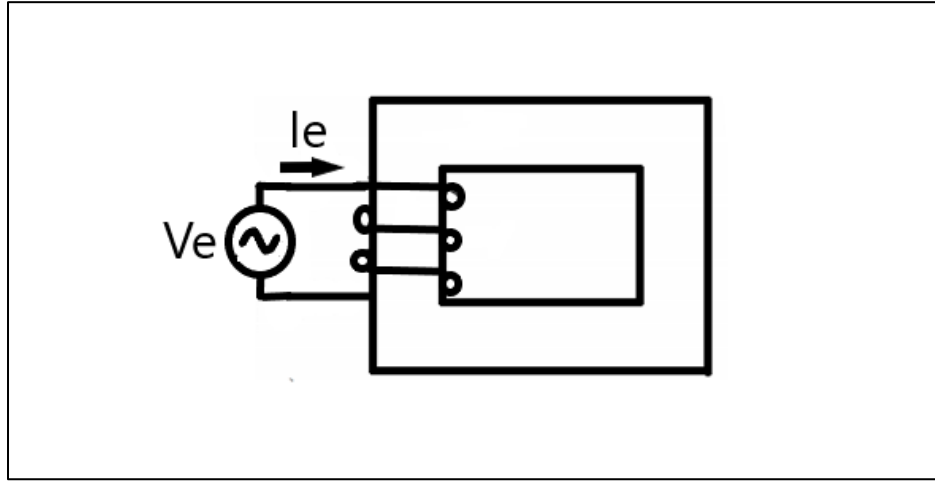


Figure 3.1 A Magnetic Core Excited by Electric Current

### 3.1. RELUCTANCE MODEL

This section discusses the age old reluctance model [44] for magnetic elements. The model contains a single element for representing the relationship between magnetic voltage and magnetic flux.

H. A. Rowland's law (1873) [24] is the counterpart of G. Ohm's law (1827) for magnetic circuits [44]. Complex reluctance model magnetic reluctance in Equation 3.1 is defined as the ratio of sinusoidal magnetomotive force and sinusoidal magnetic flux [44].

$$\mathcal{R}_m = \frac{\mathcal{F}_m}{\Phi_m} = \frac{\oint \mathbf{H} \cdot d\mathbf{l}}{\int \mathbf{B} \cdot d\mathbf{S}} = |\mathcal{R}_m| e^{j\phi} \quad (3.1)$$

Lossy complex magnetic reluctance is non-linear and varies with the magnetic field. It resists both magnetic flux and changes in magnetic flux [44]. The characteristic model is shown in Figure 3.2, where the reluctance is represented as a resistance.

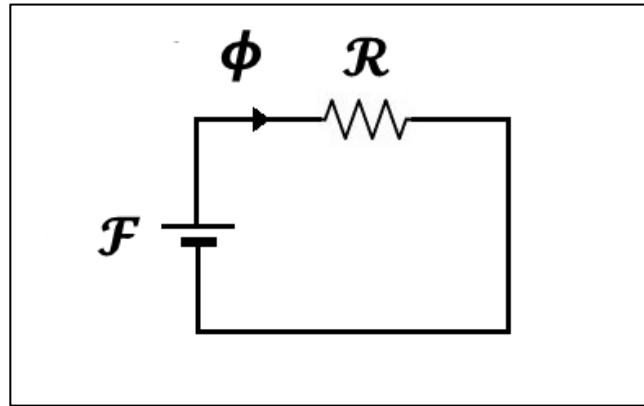


Figure 3.2 Reluctance Model for Magnetic Core

In 1969, R. W. Buntenbach proved that the reluctance model [44], [24] is not power invariant [65]. Reluctance power Loss cannot be calculated using Joule heating law (1842) analogy due to dimensional inconsistency [65] expressed in Equation 3.2 and Equation 3.3. Hence this is not an accurate model for power and energy flow.

$$[P_e] = [I_e^2][R_e] = \text{Ampere.Volt} \quad (3.2)$$

$$[P_m] \neq [\phi_m^2][\mathcal{R}_m] = \text{Volt.Second.Ampere} \quad (3.3)$$

### 3.1.1. Application

This section presents the reluctance model for a compounded DC generator [44], [66] with both a series and a shunt field winding. The circuit model is shown in Figure 3.3. The series field inductance  $L_S$  has  $N_{SE}$  turns. The series field winding resistance is represented by  $R_S$ . The shunt field winding inductance  $L_F$  has  $N_F$  turns. The shunt field winding resistance is represented by  $R_F$ . The armature winding resistance is represented by  $R_A$ .

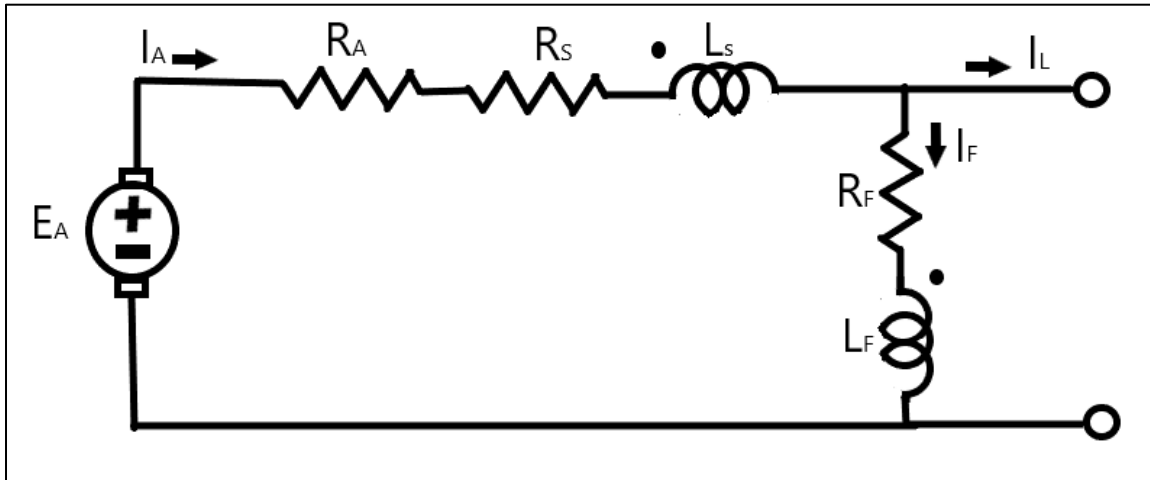


Figure 3.3 Model for Cumulatively Compounded DC Motor

The electric circuit relations are expressed in Equation 3.4, Equation 3.5 and Equation 3.6.

$$V_T = E_A - I_A(R_A + R_S) \quad (3.4)$$

$$I_L + I_F = I_A \quad (3.5)$$

$$I_F = \frac{V_T}{R_F} \quad (3.6)$$

The magnetic circuit relations are expressed in Equation 3.7 and Equation 3.8.

$$\mathcal{F}_{net} = \mathcal{F}_F \pm \mathcal{F}_{SE} - \mathcal{F}_{AR} \quad (3.7)$$

$$N_F I_F^* = N_F I_F \pm N_{SE} I_A - \mathcal{F}_{AR} \quad (3.8)$$

The generated electric voltage is related to the magnetic flux and rotor speed by the Equation 3.9.

$$E_A = k\phi\omega_m \quad (3.9)$$

Ferromagnetic materials are non-linear [33], [46], [53] as their permeability varies with the strength of applied field intensity. At high magnetic field intensity, the material saturates, limiting further increase of magnetic flux [33]. Hence, the susceptibility decreases rapidly.

A compounded DC generator was simulated in Simulink as shown in Figure 3.4.

The generator parameters were the following:  $R_A=0.19\ \Omega$ ,  $R_S=0.02\ \Omega$ ,  $R_F=20\text{-}50\Omega$ ,  $N_F=1000$  turns,  $N_S=20$  turns and rated speed=1800 rpm.

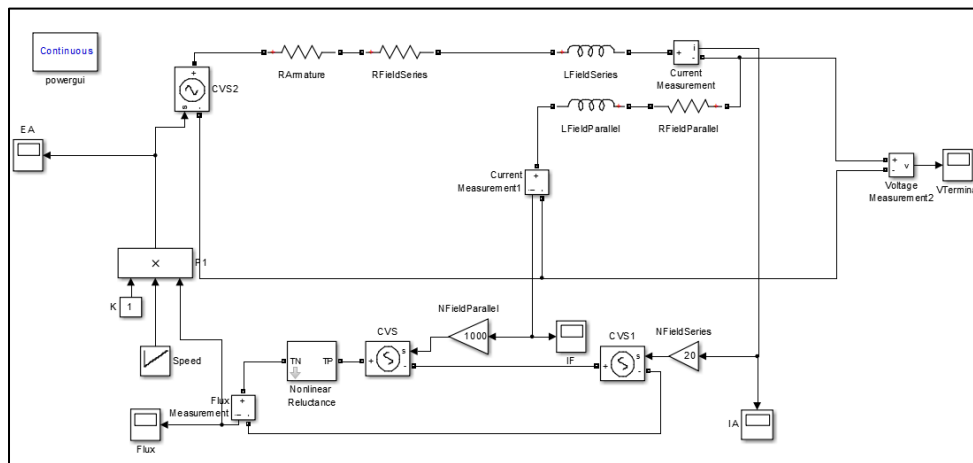


Figure 3.4 Simulink Model for Cumulatively Compounded DC Generator



The reluctance model preserves the integrity of the machine's geometry [44]. It decouples the electrical system from the magnetic system. The magnetic paths in the core are represented using an equivalent nonlinear reluctance element shown in Figure 3.5.

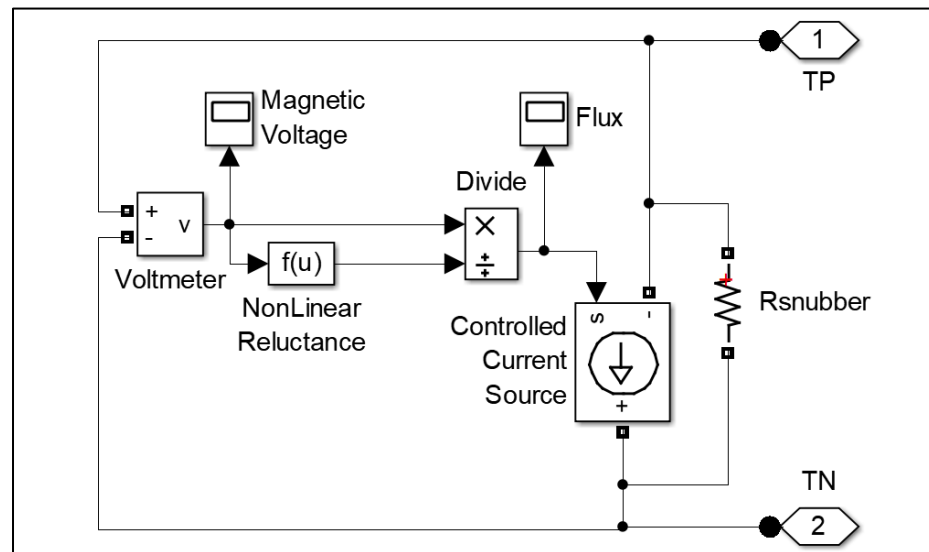


Figure 3.5 Simulink Model for Non-linear Permeance

The rotor mechanical speed was increased from 500 to 2000 rpm in steps of 500rpm as shown in Figure 3.6. The field currents, generated magnetomotive force, electromotive force and terminal voltage are also shown. Clearly, the results do not increase linearly with speed.

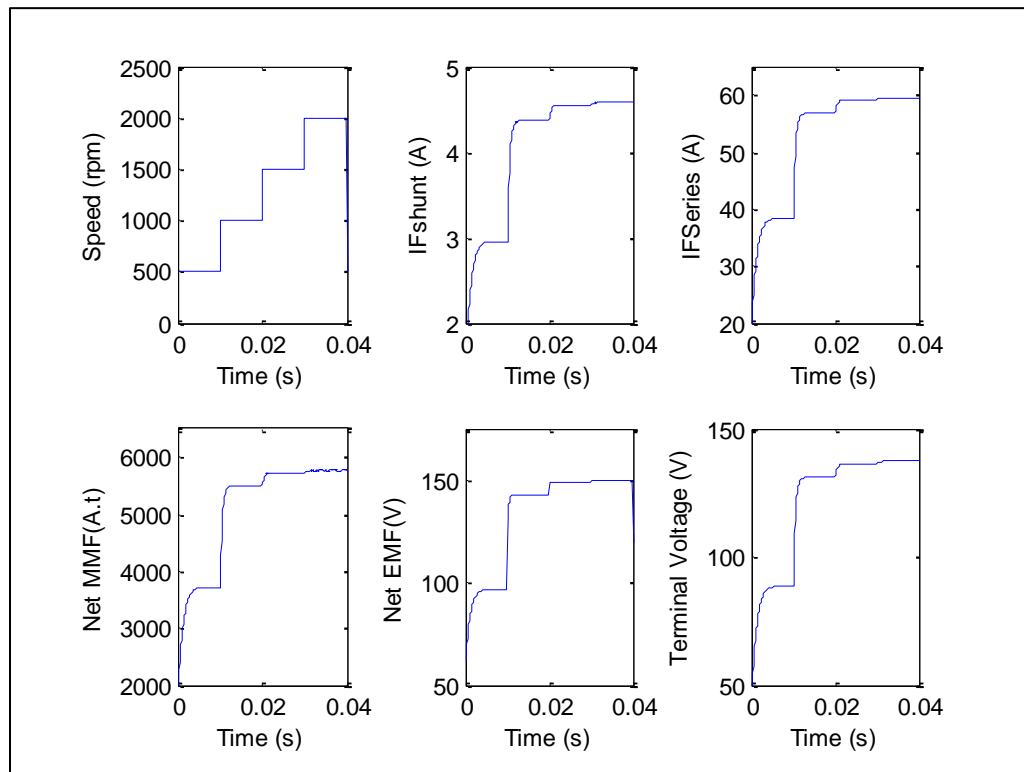


Figure 3.6 Evolution of Field Currents, Net MMF, Generated EMF and Terminal Voltage

The terminal voltage versus rotor speed curve is shown in Figure 3.7. The nonlinear behavior results due to the saturation of magnetic core.

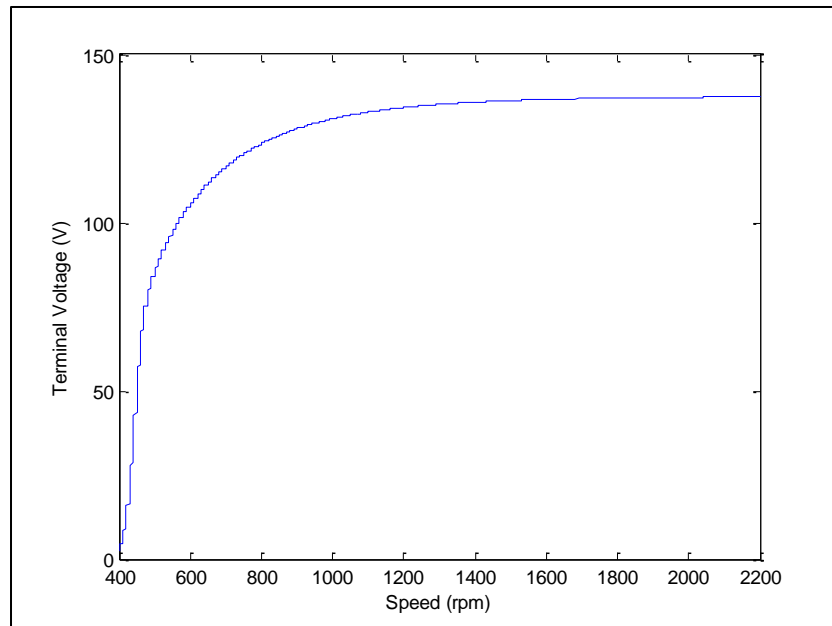


Figure 3.7 Variation of Terminal Voltage with Rotor Speed

Clearly, the reluctance model is only suitable for steady state simulations of machines if the reluctance profile of the magnetic core and the voltage constant is already known.

### 3.2. PERMEANCE-CAPACITANCE MODEL

This section presents the power invariant permeance-capacitance model [11], [30], [31], [32], [59], [65], [60], [61] for a transformer based on the gyrator theory. The model is valuable for modeling nonlinear magnetic materials with hysteresis losses.

In 1948, B. Tellegen's gyrator theory was devised to describe power invariant transformation of magnetic and electric quantities in a transformer [59], [61], [65]. The dual effort and flow quantities are related by the gyration constant (N). According to M. Faraday's law (1831) [24], electric voltage is responsible for producing magnetic displacement current which is defined as the rate of change of magnetic flux in Equation 3.10 and Equation 3.11.

$$V_e = -N \frac{d\phi_m}{dt} \quad [Volt] \quad (3.10)$$

$$\begin{aligned} \oint \mathbf{E} \cdot d\mathbf{l} &= -\frac{d}{dt} \int \mathbf{B} \cdot d\mathbf{S} \\ &= -\mu_0 \frac{d}{dt} \int \mathbf{H} \cdot d\mathbf{S} - \mu_0 \frac{d}{dt} \int \mathbf{M} \cdot d\mathbf{S} \end{aligned} \quad (3.11)$$

Magnetic displacement current is the rate of change of magnetic flux which results from the polarization of magnetic dipoles. For a magnetic core, the magnetic displacement current and magnetomotive force are related by Equation 3.12.

$$I_{m,disp} = \frac{d\phi_m}{dt} = -\frac{1}{N} V_e \quad [Volt] \quad (3.12)$$

According to A. Ampere's law (1861) [24], magnetic voltage is responsible for producing electric conduction current [24].

$$V_m = \mathcal{F}_m = NI_e \quad [Ampere] \quad (3.13)$$

R. W. Buntenbach proposed power invariant permeance-capacitance model in 1969 [11], [30], [31], [32], [59], [65], [60], [61] to replace reluctance model. It is shown in Figure 3.8.

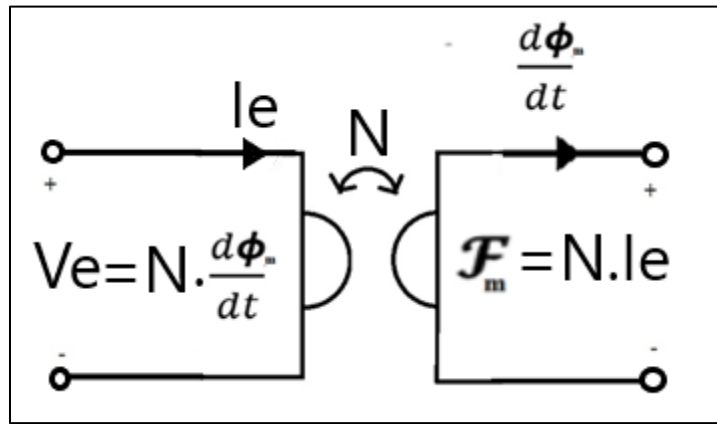


Figure 3.8 Gyrator Model for Power Invariant Transformation of Electric and Magnetic Quantities

Magnetic permeance [30], [31], [32], [59], [60], [61] is defined in Equation 3.14 as a magnetic capacitor which stores magnetic flux; measured in volt-seconds.

$$\Phi_{Pm}(t) = P_m v_{Pm}(t) \quad [Volt.s] \quad (3.14)$$

The permeance resists changes in magnetic voltage as expressed in Equation 3.15.

$$i_{Pmdisp}(t) = P_m \frac{dv_{Pm}(t)}{dt} \quad [Volt] \quad (3.15)$$

This permeance is measured in units of Henry. It is closely related to magnetic reluctance and magnetic inductance of the core.

$$P_m = \frac{1}{\mathcal{R}_m} = \frac{L_m}{N^2} = \mu \frac{A}{l} \quad [Henry] \quad (3.16)$$

The resulting permeance-capacitance model for a two winding transformer is shown in Figure 3.9.

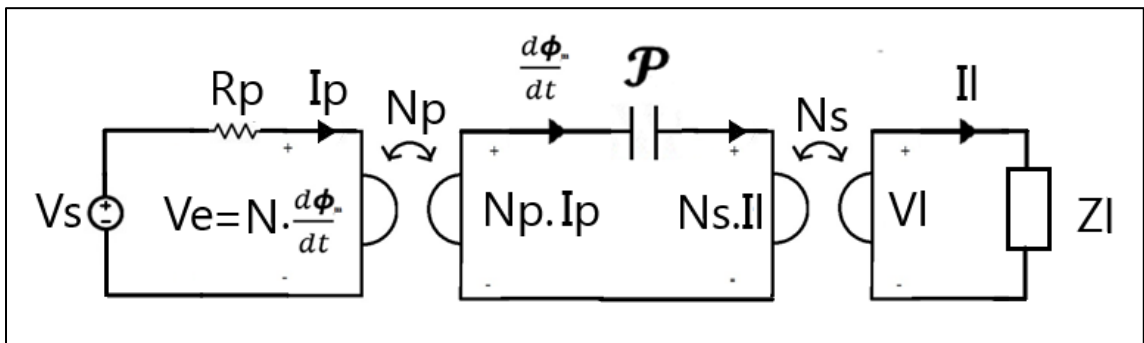


Figure 3.9 Permeance-Capacitance Model for Transformer

### 3.2.1. Application

This section presents a permeance-capacitance model [11], [30], [31], [32], [59], [60], [61] for a full bridge isolated buck converter. The electrical circuit is shown in Figure 3.10. The switching technique for the switches and diodes is given in Table 3.1 below.

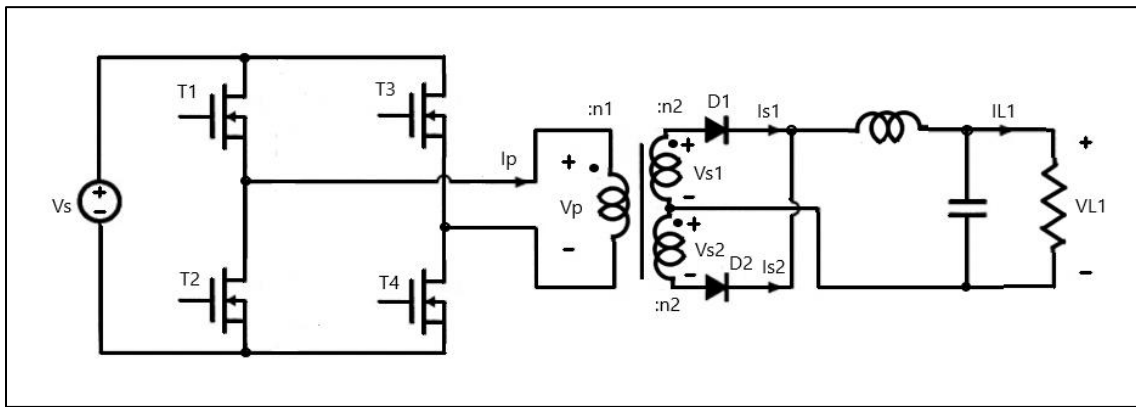


Figure 3.10 Electrical Circuit for Full Bridge Isolated Buck Converter

Table 3.1 Switching Table for Transistors and Diodes

Time Interval	Transistors				Diodes	
	T1	T2	T3	T4	D1	D2
$0 < t \leq DT_s$	ON	OFF	OFF	ON	ON	OFF
$DT_s < t \leq T_s$	OFF	ON	OFF	ON	ON	ON
$T_s < t \leq (1 + D)T_s$	OFF	ON	ON	OFF	OFF	ON
$(1 + D)T_s < t \leq 2T_s$	ON	OFF	ON	OFF	ON	ON

The design parameters are given in the Table 3.2 below.

Table 3.2 Design Parameters for Full Bridge Isolated Buck Converter

Parameter	Symbol	Value
Source Voltage	$V_s$	160 V
Load Voltage	$V_{L1}$	5 V $\pm$ 5%
Load Current	$I_{L1}$	100 A $\pm$ 5%
Core cross-sectional area	$A_c$	2.26cm <sup>2</sup>
Core Magnetic Path Length	$l_m$	9.58 cm
Peak Flux Density	$\Delta B$	0.08 T
Core relative Permeability	$\mu$	3500
Core Resistivity	$\rho$	0.02 $\Omega$ m
Switching Frequency	$F_s$	150 kHz
Duty Cycle	D	0.75

The Design procedure had the following steps:

1. Applied primary winding flux was calculated using Equation 3.17.

$$\begin{aligned}
 \lambda_p &= \int_0^{T_s} V_p(t) dt = DT_s V_s = (0.75) \left( \frac{1}{150 \text{ kHz}} \right) (160 \text{ V}) \\
 &= 8 \times 10^{-4} \text{ V.s}
 \end{aligned} \tag{3.17}$$



2. Turns of primary winding were calculated using Equation 3.18.

$$n_1 = \frac{\lambda_p}{2\Delta BA_c} = \frac{(8 \times 10^{-4} \text{ V.s})}{2(0.08 \text{ T})(2.26 \times 10^{-4} \text{ m}^2)} \approx 22 \quad (3.18)$$

3. Turns of secondary windings were calculated using Equation 3.19.

$$n_2 = \frac{V_{L1} + V_{Diode,on}}{V_S} n_1 = \frac{(5 + 2) \times 22}{160} \approx 1 \quad (3.19)$$

4. Maximum core permeance and minimum core permeance was calculated using Equation 3.20 and Equation 3.21 respectively.

$$P_{m,max} = \frac{\mu A_c}{l_m} = \frac{(3500 \times 4\pi \times 10^{-7})(2.26 \times 10^{-4} \text{ m}^2)}{(9.58 \times 10^{-2} \text{ m})} = 10.3 \mu H \quad (3.20)$$

$$P_{m,min} = \frac{\mu_o A_c}{l_m} = \frac{(4\pi \times 10^{-7})(2.26 \times 10^{-4} \text{ m}^2)}{(9.58 \times 10^{-2} \text{ m})} = 2.94 \text{ nH} \quad (3.21)$$

5. Core resistance was calculated using Equation 3.22.

$$R_c = \frac{\rho l_m}{A_c} = \frac{(0.02 \Omega \text{ m})(9.58 \times 10^{-2} \text{ m})}{(2.26 \times 10^{-4} \text{ m}^2)} = 8.48 \Omega \quad (3.22)$$

6. Load filter inductance and capacitance was calculated using the Equation 3.23 and Equation 3.24 respectively

$$L_{filter} = \frac{(1-D)T_s}{\Delta I_{L1}} V_{L1} = \frac{(0.25) \left( \frac{1}{150 \text{ kHz}} \right)}{\left( \frac{5}{100} \times 100 \text{ A} \right)} (5 \text{ V}) = 1.7 \mu H \quad (3.23)$$

$$C_{filter} = \frac{(1-D)T_s}{\Delta V_{L1}} I_{L1} = \frac{(0.25) \left( \frac{1}{150 \text{ kHz}} \right)}{\left( \frac{5}{100} \times 5 \text{ V} \right)} (100 \text{ A}) = 67 \text{ nF} \quad (3.24)$$

The equivalent circuit for the converter is shown in Figure 3.11. It shows the primary voltage as a PWM Voltage source  $V_p$ . The primary winding resistance is represented by  $R_p$ . The primary current is converted to magnetomotive force across the gyrator with gyration constant  $n_1$ . The nonlinear core permeance is represented by element  $P$ . The secondary side consists of two gyrators with gyration constant  $n_2$ . Each gyrator senses the magnetic voltage and generates proportional secondary current. The secondary side circuit consists of a rectifier circuit and a filter circuit to provide constant voltage and current to the load.

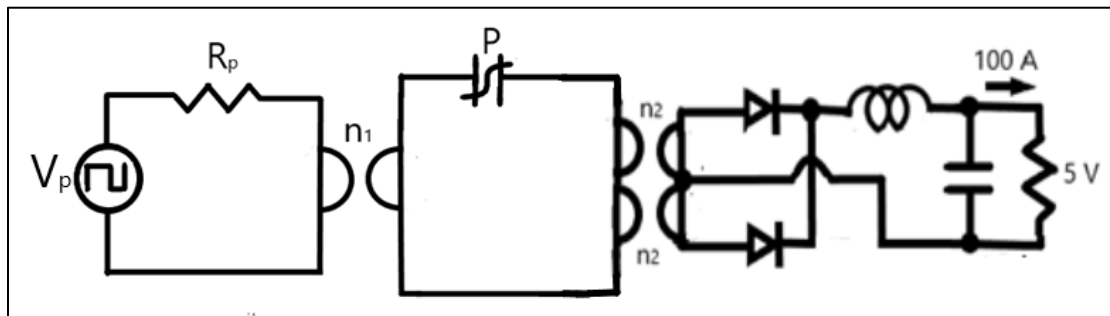


Figure 3.11 Equivalent Converter Circuit with Gyration and Non-linear Core Permeance



The flux response of non-linear permeance for voltage variation is recorded in Figure 3.13. The slope of the flux-voltage curve gives the instantaneous permeance. The area between the two curves represents the magnetic hysteresis loss across the resistance  $R_m$ .

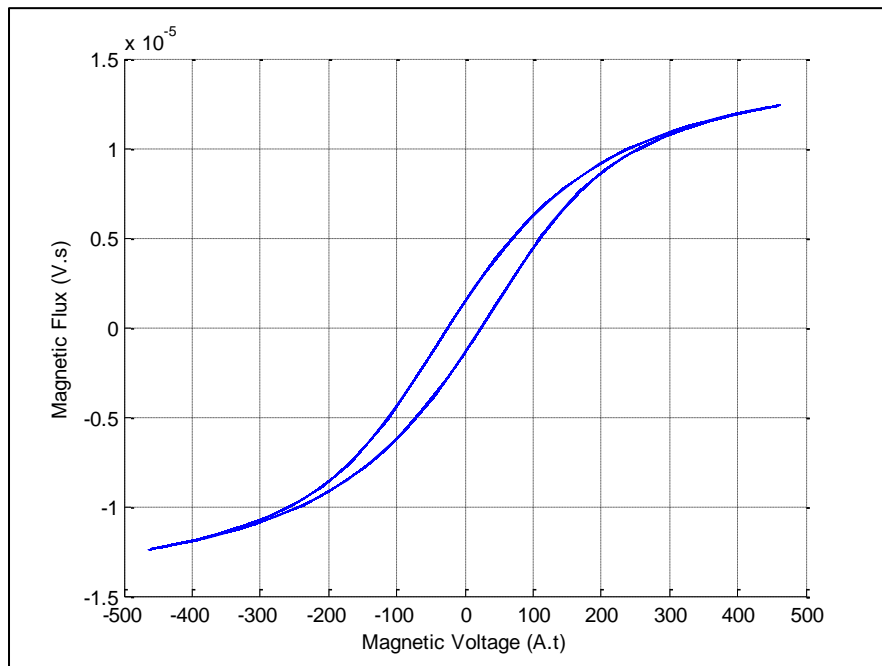


Figure 3.13 Variation of Permeance Flux versus Permeance Magnetic Voltage

The designed transformer was excited by a sinusoidal voltage source of amplitude 100 V as shown in Figure 3.14. The transformer was loaded with a resistive load of  $1\ \Omega$ . The output voltage and current are plotted below. As seen, the output voltage and current shows large spikes when the permeance experiences large voltages.

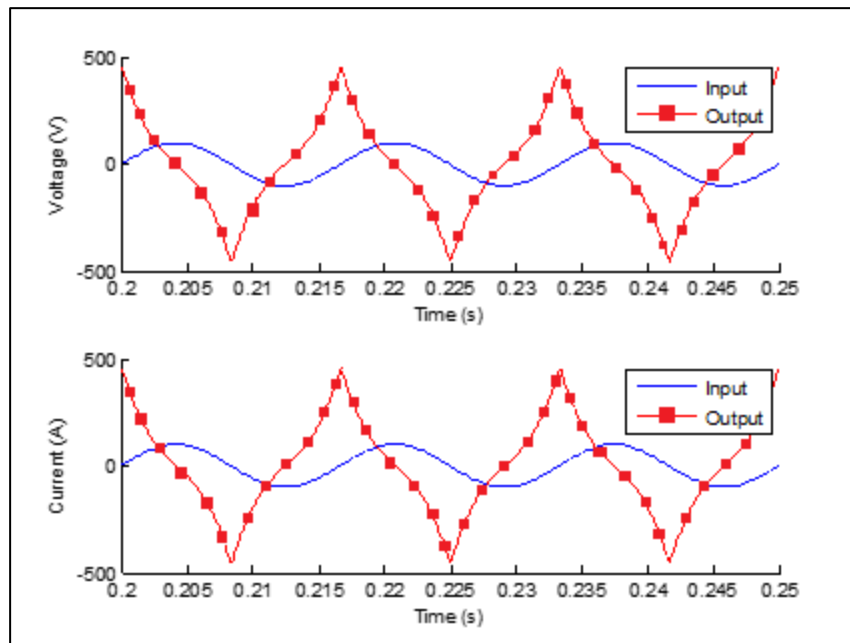


Figure 3.14 Transformer Voltage and Current Response for Sinusoidal Excitation and Resistive Load

The Simulink model for isolated buck converter is shown in Figure 3.15. The full bridge is fed by a block that generates gate signals for electronic switches. The output of the full bridge is fed to the primary winding gyrator which converts electrical current to magnetomotive force. The magnetic core is represented by a nonlinear permeance block. The current of the permeance is fed to the secondary winding gyrator which converts it into electromotive force. The secondary side consists of a full bridge rectifier and a low pass filter. This ensures constant voltage and current supply to the load.

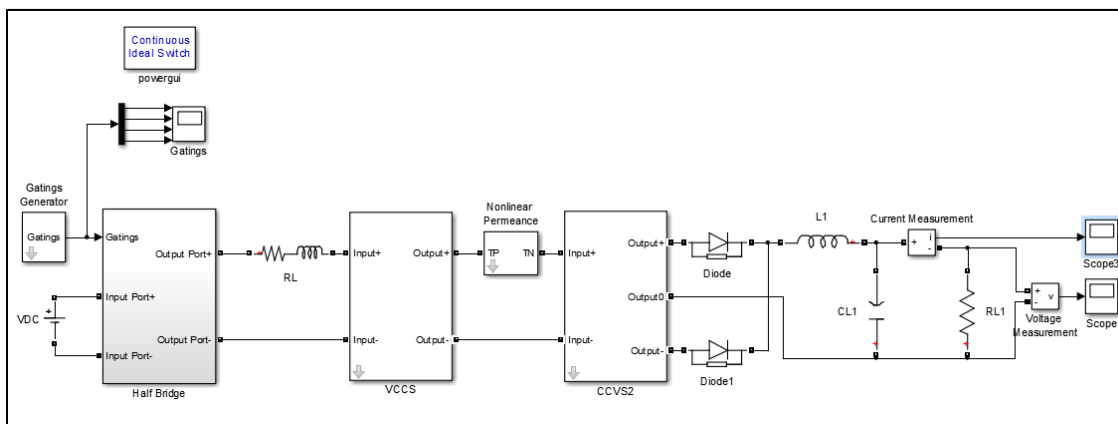


Figure 3.15 Simulink Model for Full Bridge Isolated Buck Converter

The Simulink models for primary and secondary winding gyrators are shown in Figure 3.16 and Figure 3.17 respectively. They convert electric current to magnetomotive force and magnetic displacement current to electromotive force respectively.

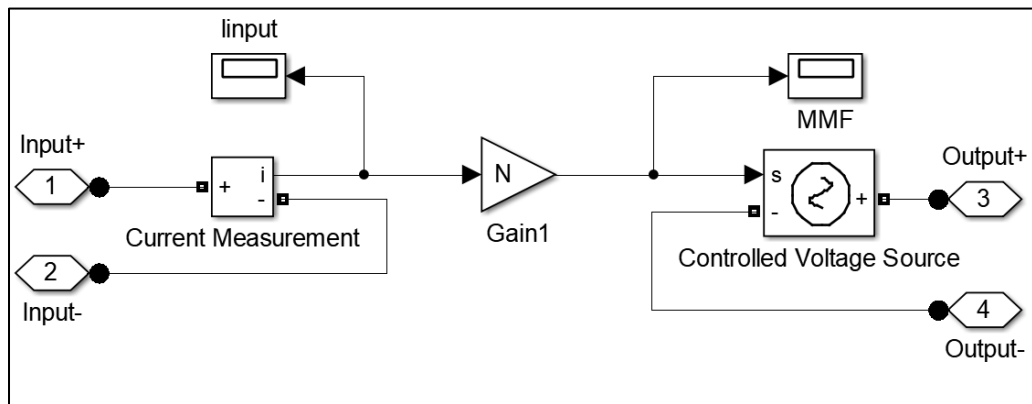


Figure 3.16 Simulink Model for Primary Winding Gyrator

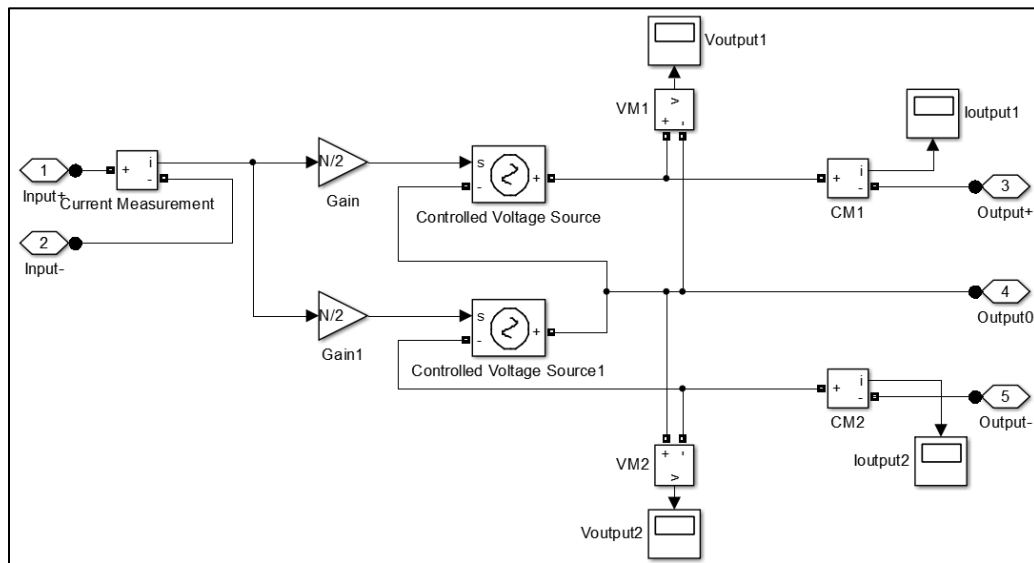


Figure 3.17 Simulink Model for Secondary Winding Gyrator



The primary winding electric voltage and electric current are plotted in Figure 3.18. As desired, the voltage and current waveforms are sinusoidal waveforms.

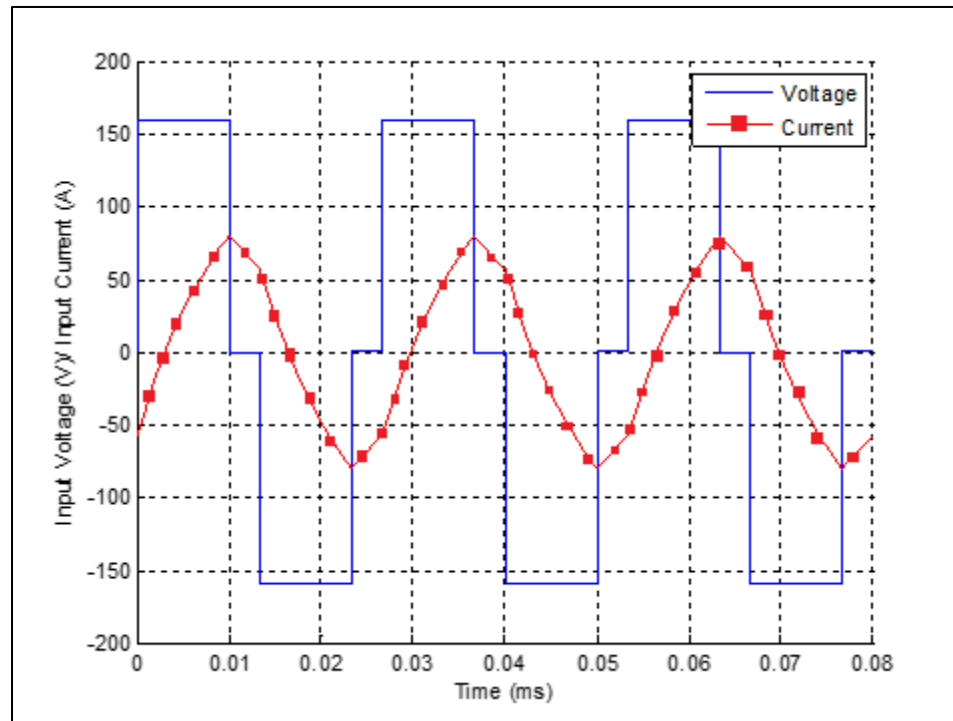


Figure 3.18 Primary Winding Voltage and Current

The load electric voltage and electric current are plotted in Figure 3.19. The load voltage has a mean value of 5 V and the load current has a mean value of 100 A. As desired, the voltage and current ripple is almost 5 percent for the load voltage and load current.

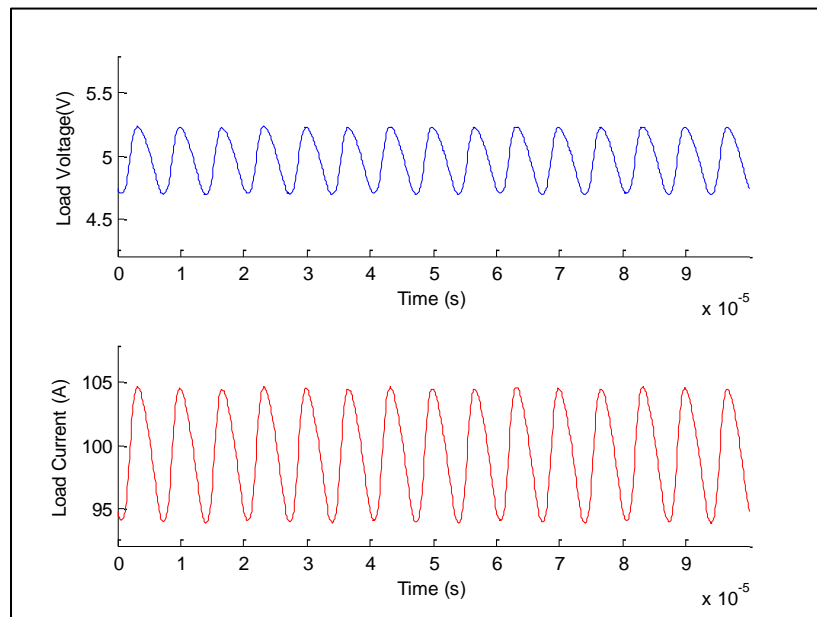


Figure 3.19 Load Voltage and Current

The permeance magnetic voltage and magnetic displacement current are plotted in Figure 3.20. The permeance saturates when the magnetic voltage becomes high hence magnetic current spikes are seen.

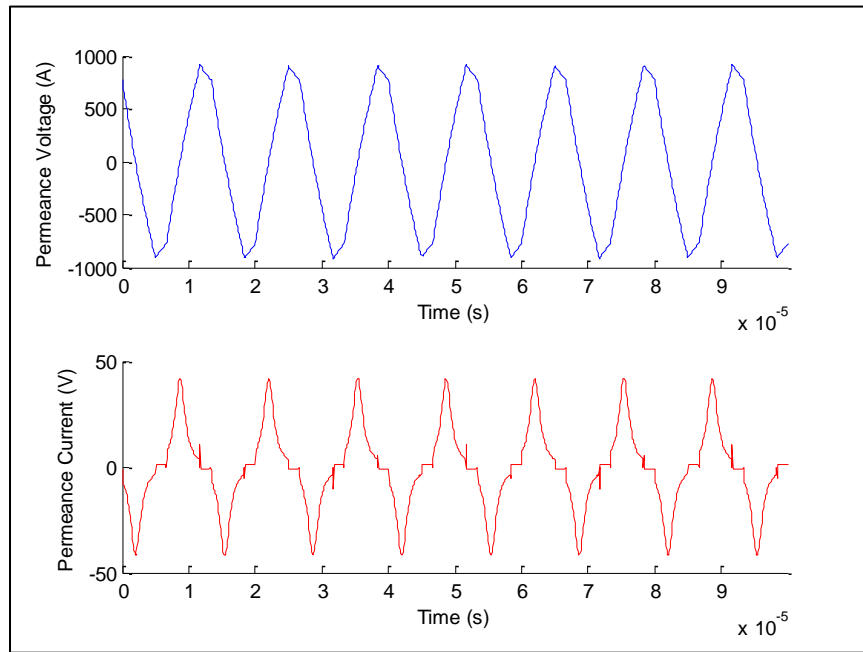


Figure 3.20 Permeance Voltage and Current

This section presented the power invariant permeance-capacitance model for a transformer used in a full bridge isolated buck converter. The permeance-capacitance model is valuable for simulation of hysteresis in nonlinear cores at low frequency. The next section will discuss the high frequency magnetic transmission line model.

### 3.3. MAGNETIC TRANSMISSION LINE MODEL

This section presents the third model for magnetic elements called the magnetic transmission line model [4], [5], [6], [7], [8]. This model is based on the electric transmission line model [4], [5], [6], [7], [8]. Like the permeance-capacitance model, it also considers flux rate as the effective magnetic displacement current whereby magnetic permeability plays a similar role to electric conductivity by enhancing the magnetic displacement current inside the magnetic material.

In 2012, J. Faria and M. Pires presented magnetic transmission line model [4], [5], [6], [7], [8] based on electric transmission line model. The propagation of electromagnetic waves is governed by the Maxwell's equations [24] presented below.

$$\oint \mathbf{H} \cdot d\mathbf{l} = \oint \mathbf{J}_e \cdot d\mathbf{S} + \frac{d}{dt} \int \mathbf{D} \cdot d\mathbf{S} = \oint \mathbf{J}_e \cdot d\mathbf{S} - \epsilon_0 \frac{d}{dt} \int \mathbf{E} \cdot d\mathbf{S} - \epsilon_0 \frac{d}{dt} \int \mathbf{E} \cdot d\mathbf{S} \quad (3.25)$$

$$\oint \mathbf{E} \cdot d\mathbf{l} = -\frac{d}{dt} \int \mathbf{B} \cdot d\mathbf{S} = -\mu_0 \frac{d}{dt} \int \mathbf{H} \cdot d\mathbf{S} - \mu_0 \frac{d}{dt} \int \mathbf{M} \cdot d\mathbf{S} \quad (3.26)$$

$$\oint \mathbf{B} \cdot d\mathbf{S} = 0 \quad (3.27)$$

$$\oint \mathbf{D} \cdot d\mathbf{S} = \iiint \rho_e \cdot dV \quad (3.28)$$

Analogous to the scalar electric potential, scalar magnetic potential  $V_m$  can be defined as in Equation 3.29 and Equation 3.30.

$$V_m = \int_a^b \mathbf{H} \cdot d\mathbf{l} \quad (3.29)$$

$$\mathbf{H} = \nabla V_m \quad (3.30)$$

The magnetic displacement current  $I_m$  is defined as the rate of change of magnetic flux  $\Phi_m$ ; as expressed in Equation 3.31 and Equation 3.32.

$$\oint \mathbf{E} \cdot d\mathbf{l} = - \int \frac{d\mathbf{B}}{dt} \cdot d\mathbf{S} = - \oint \mathbf{J}_m \cdot d\mathbf{S} = - \frac{d\Phi_m}{dt} = I_m \quad (3.31)$$

$$\nabla \times \mathbf{E} = -\mathbf{J}_m \quad (3.32)$$

The per unit length transverse magnetic inductance  $L_T$  represents a magnetic energy storage element. It is defined in terms of per unit length magnetic charge  $\Phi_m$  and scalar magnetic voltage  $V_m$  in Equation 3.33.

$$\Phi_m = L_T V_m \quad (3.33)$$

The per unit length longitudinal capacitance  $C_L$  represents an electric energy storage element [11]. It is defined in terms of electric displacement flux  $\Psi_e$  and magnetic displacement current  $I_m$  in Equation 3.34.

$$\Phi_e = C_L I_m \quad (3.34)$$

Assuming TEM-guided propagation in z-direction ( $E_y = E_z = H_x = H_z = 0, \rho_e = J_e = 0$ ), as shown in Figure 3.21, the relation between the magnetic voltage and magnetic displacement current for a homogeneous magnetic transmission line [4], [5], [6], [7], [8] was derived. The results are given in Equation 3.35 and Equation 3.36.

$$\frac{d}{dz} \int \mathbf{E}_x dx = -\mu \frac{d}{dt} \int \mathbf{H}_y dy \quad (3.35)$$

$$\frac{d}{dz} \int \mathbf{H}_y dy = -\varepsilon \frac{d}{dt} \int \mathbf{E}_x dx \quad (3.36)$$

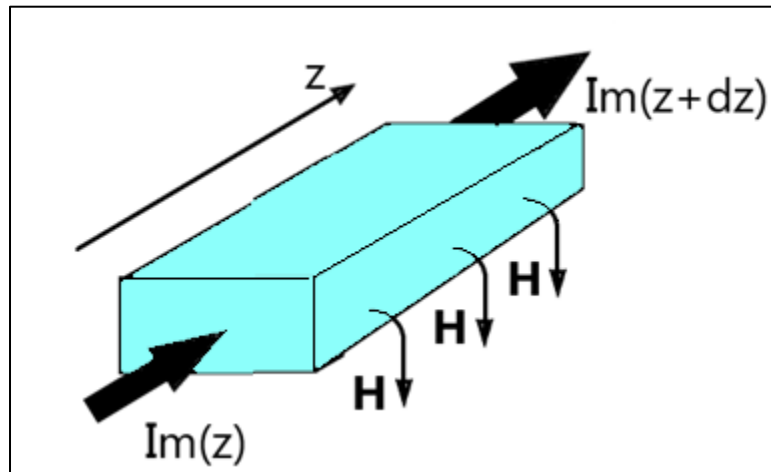


Figure 3.21 A Section of Magnetic Transmission Line Transmitting Flux in z-direction

The resulting transmission line equations are given in Equation 3.37 and Equation 3.38.

$$\frac{dI_m}{dz} = -L_T \frac{dV_m}{dt} \quad (3.37)$$

$$\frac{dV_m}{dz} = -C_L \frac{dI_m}{dt} \quad (3.38)$$

A forward travelling and a backward travelling wave can simultaneously exist on the transmission line. The solution for the magnetic voltage and magnetic displacement current is given in Equation 3.39 and Equation 3.40 respectively.

$$V_m(z) = V_m^+ e^{-j\beta z + j\theta^+} + V_m^- e^{j\beta z + j\theta^-} \quad (3.39)$$

$$I_m(z) = \frac{V_m^+}{Z_o} e^{-j\beta z + j\theta^+ - j\theta_z} - \frac{V_m^-}{Z_o} e^{j\beta z + j\theta^- - j\theta_z} \quad (3.40)$$

The formula for propagation constant is given in Equation 3.41.

$$\beta = \sqrt{L_T C_L} \quad (3.41)$$

The characteristic impedance is the ratio of magnetic displacement current to the magnetic voltage. It is defined in Equation 3.42.

$$Z_m = \frac{I_m(z)}{V_m(z)} = \sqrt{\frac{L_T}{C_L}} \quad (3.42)$$

The average power flow in the magnetic transmission line [4], [5], [6], [7], [8] can be represented in terms of three distinct components: the average power in the forward travelling wave, the average power in the backward travelling wave and the dissipated power.

$$P_{av}(z) = \frac{1}{2} \text{Re}(V(z)I^*(z)) \quad (3.43)$$

$$P_{av}(z) = \frac{1}{2} \text{Re} \left( (V_m^+ e^{-\alpha z - j\beta z + j\theta^+} + V_m^- e^{\alpha z + j\beta z + j\theta^-}) \left( \frac{V_m^+}{Z_o} e^{-\alpha z + j\beta z - j\theta^+ + j\theta_z} - \frac{V_m^-}{Z_o} e^{\alpha z - j\beta z - j\theta^- + j\theta_z} \right) \right) \quad (3.44)$$

$$P_{av}(z) = P_{av}^+(z) + P_{av}^-(z) + P_{loss}(z) \quad (3.45)$$

In a non-ideal magnetic transmission line [4], [5], [6], [7], [8], magnetic voltage drop can be accounted by including magnetic reluctance/ conductance. It represents all the magnetization, polarization and conduction losses [3] due to electric conductivity, complex



permittivity and complex permeability [35], [36], [1], [2]. Magnetic inductance and magnetic capacitance are energy storage elements in this model [10], [11]. The resultant magnetic transmission line circuit is shown in Figure 3.22.

$$G_L = \frac{\mathcal{R}_m}{j\omega} = \frac{V_m}{I_m} = \frac{\int \mathbf{H} \cdot d\mathbf{l}}{\oint \mathbf{E} \cdot d\mathbf{l}} \quad [Ohm] \quad (3.46)$$

$$L_T = \frac{\phi_m}{V_m} = \frac{\int \mathbf{B} \cdot d\mathbf{S}}{\int \mathbf{H} \cdot d\mathbf{l}} \quad [Henry] \quad (3.47)$$

$$C_L = \frac{\phi_e}{I_m} = \frac{\int \mathbf{D} \cdot d\mathbf{S}}{\oint \mathbf{E} \cdot d\mathbf{l}} \quad [Farad] \quad (3.48)$$

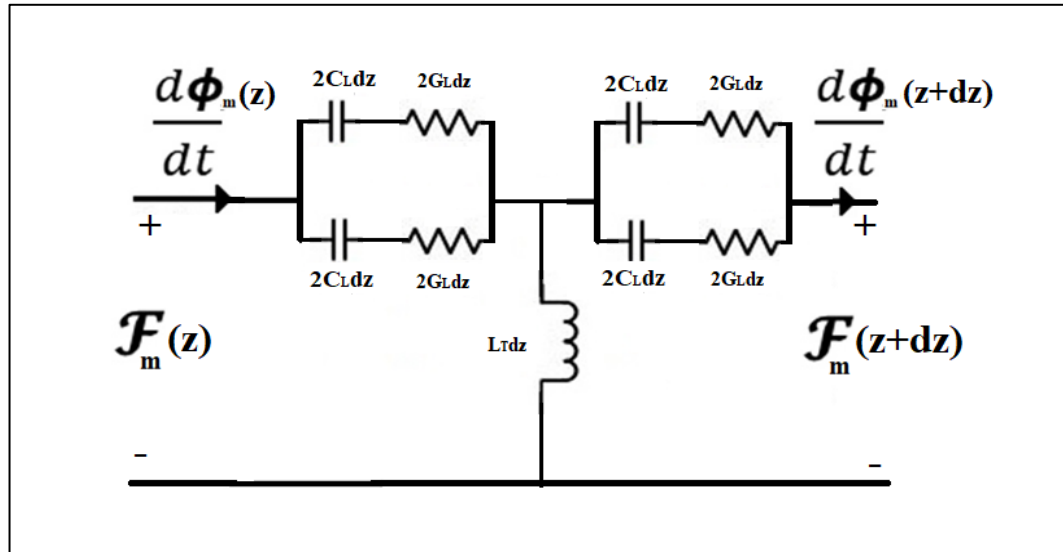


Figure 3.22 Equivalent Circuit Model for Magnetic Transmission Line

Energy is dissipated in magnetic conductance according to Equation 3.49.

$$P_{loss} = I_m^2 G_L \quad [Watt] \quad (3.49)$$

Electrical energy is stored in magnetic capacitance [10], [11]; and magnetic energy is stored in magnetic inductance [4], [5], [6], [7], [8] according to Equation 3.50 and Equation 3.51 respectively.

$$W_e = \frac{1}{2} C_L V_m^2 = \frac{1}{2} \int \mathbf{B} \cdot \mathbf{H} \, dV \quad (3.50)$$

$$W_m = \frac{1}{2} L_T I_m^2 = \frac{1}{2} \int \mathbf{D} \cdot \mathbf{E} \, dV \quad (3.51)$$

The resulting magnetic transmission line equations [4], [5], [6], [7], [8] are given below.

$$\frac{dI_m}{dz} = -L_T \frac{dV_m}{dt} \quad (3.52)$$

$$\frac{dV_m}{dz} = -G_L I_m - C_L \frac{dI_m}{dt} \quad (3.53)$$

$$\frac{d^2 V_m}{dz^2} = L_T C_L \frac{d^2 V_m}{dt^2} + L_T G_L \frac{dV_m}{dt} \quad (3.54)$$

$$\frac{d^2 I_m}{dz^2} = L_T G_L \frac{d^2 I_m}{dt^2} + L_T C_L \frac{dI_m}{dt} \quad (3.55)$$

Assuming sinusoidal steady state, the equations can be expressed in terms of phasor quantities as in Equation 3.56 and Equation 3.57.

$$\frac{d^2 V_m}{dz^2} = -\omega^2 L_T C_L V_m + j\omega L_T G_L V_m = (-\omega^2 L_T C_L + j\omega L_T G_L) V_m \quad (3.56)$$

$$\frac{d^2 I_m}{dz^2} = -\omega^2 L_T G_L I_m + j\omega L_T C_L I_m = (-\omega^2 L_T G_L + j\omega L_T C_L) I_m \quad (3.57)$$

The magnetic transmission line equations [4], [5], [6], [7], [8] can be solved just like electric transmission line equations. The solutions are compared in the Table 3.3.

Table 3.3 Comparison of Electric and Magnetic Transmission Lines

Electric Transmission Line	Magnetic Transmission Line
$\frac{dI_e}{dz} = -G_T V_e - C_T \frac{dV_e}{dt}$ $\frac{dV_e}{dz} = -R_L I_e - L_L \frac{dI_e}{dt}$	$\frac{dI_m}{dz} = -L_T \frac{dV_m}{dt}$ $\frac{dV_m}{dz} = -G_L I_m - C_L \frac{dI_m}{dt}$
$\frac{d^2 I_e}{dz^2} = L_L C_T \frac{d^2 I_e}{dt^2} + (L_L G_T + R_L C_T) \frac{dI_e}{dt} + R_L G_T I_e$ $\frac{d^2 V_e}{dz^2} = L_L C_T \frac{d^2 V_e}{dt^2} + (L_L G_T + R_L C_T) \frac{dV_e}{dt} + R_L G_T V_e$	$\frac{d^2 I_m}{dz^2} = L_T G_L \frac{d^2 I_m}{dt^2} + L_T C_L \frac{dI_m}{dt}$ $\frac{d^2 V_m}{dz^2} = L_T C_L \frac{d^2 V_m}{dt^2} + L_T G_L \frac{dV_m}{dt}$
$V_e(z) = V_{e_i}(0)e^{-\gamma z} + V_{e_r}(0)e^{+\gamma z}$ $I_e(z) = I_{e_i}(0)e^{-\gamma z} - I_{e_r}(0)e^{+\gamma z}$	$V_m(z) = V_{m_i}(0)e^{-\gamma z} + V_{m_r}(0)e^{+\gamma z}$ $I_m(z) = I_{m_i}(0)e^{-\gamma z} - I_{m_r}(0)e^{+\gamma z}$
$\gamma = \sqrt{(R_e + j\omega L_L)(G_e + j\omega C_T)}$ $\gamma = \sqrt{(\rho + j\omega\mu)(\sigma + j\omega\varepsilon)}$ $\gamma = \alpha + j\beta$	$\gamma = \sqrt{(j\omega L_T)(G_L + j\omega C_L)}$ $\gamma = \sqrt{(j\omega\mu)(\sigma + j\omega\varepsilon)}$ $\gamma = \alpha + j\beta$
$Z_w = \frac{V_e(z)}{I_e(z)} = \sqrt{\frac{R_L + j\omega L_L}{G_T + j\omega C_T}}$	$Z_w = \frac{I_m(z)}{V_m(z)} = \sqrt{\frac{j\omega L_T}{G_L + j\omega C_L}}$

For electric transmission lines of same geometry described by  $L_L$  and  $C_T$  matrices, the magnetic transmission line parameter matrices are closely related; as in the Equation 3.58, Equation 3.59, Equation 3.60 and Equation 3. 61 below.

$$L_T L_L = \mu_0^2 \quad (3.58)$$

$$L_T C_L = \mu_0 \varepsilon \quad (3.59)$$

$$\varepsilon_0 L_T = \mu_0 C_T \quad (3.60)$$

$$C_T C_L = \varepsilon_0 \varepsilon \quad (3.61)$$

Magnetic cores are often manufactured using layers of laminated magnetic sheets to prevent the flow of eddy currents. In such materials, magnetic flux from one transmission line can link with a neighboring magnetic transmission line [4], [5], [6], [7], [8] and disturb the information [55]. The magnetic transmission line model [4], [5], [6], [7], [8] can be extended to the generator-receptor magnetic transmission line model [4], [5], [6], [7], [8] as shown in Figure 31. This is well suited for studying electromagnetic coupling of magnetic transmission lines [4], [5], [6], [7], [8] which are in close proximity.

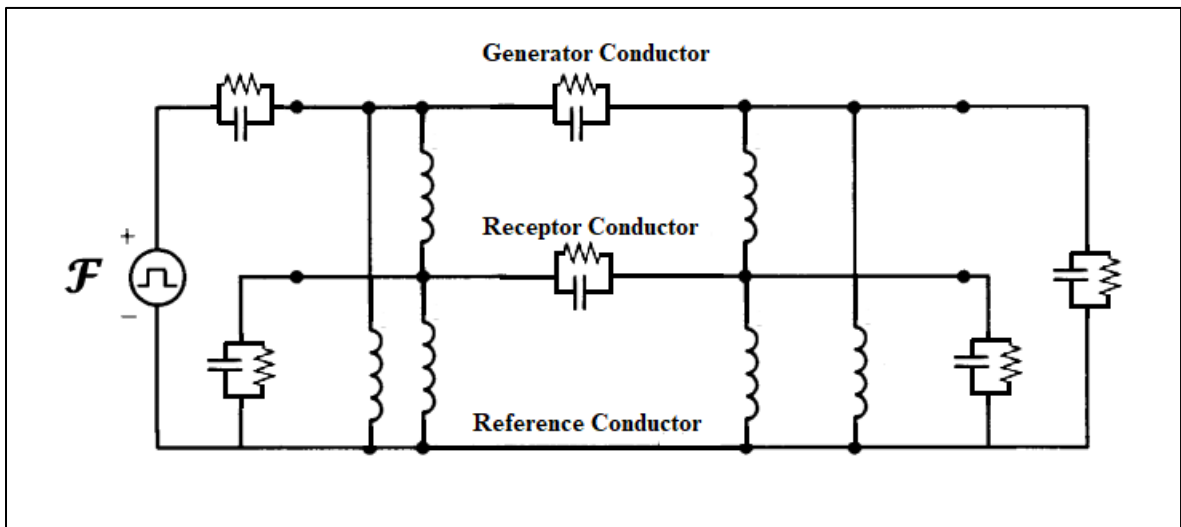


Figure 3.23 Equivalent Circuit Model for Cross-talk between Neighbouring Magnetic Transmission Lines

The three models are summarized in the Table 3.4 below.

Table 3.4 Comparison of Three Magnetic Circuit Models

	<b>Reluctance Model</b>	<b>Permeance- Capacitance Model</b>	<b>Transmission Line Model</b>
<b>Conserved Quantity</b>	?	Magnetic Flux	Magnetic Flux
<b>Flow Variable</b>	Magnetic Flux	Magnetic Flux Rate	Magnetic Flux Rate
<b>Effort Variable</b>	Magnetomotive Force	Magnetomotive Force	Magnetomotive Force
<b>Dissipation Element</b>	Magnetic Reluctance	?	Magnetic Conductance
<b>Electrical Energy Storage Element</b>	?	?	Magnetic Capacitance
<b>Magnetic Energy Storage Element</b>	?	Magnetic Permeance	Magnetic Inductance

This chapter presented three different models for modeling magnetic elements. The age-old reluctance model based on the ohm's law analogy was found to violate power invariance property. It is only suitable for steady state simulations of magnetic cores with known reluctance profile. The permeance-capacitance model uses a nonlinear permeance to model nonlinearity and hysteresis losses of magnetic materials. It is valuable for

simulating transient behavior of ferromagnetic elements like RF inductors, transformers and filters. The third model was the magnetic transmission line model which is the most accurate model for modeling dispersive, inhomogeneous and lossy magnetic cores. It uses transmission line theory to predict magnetic parameters of ferromagnetic core.



## 4. COMPUTATIONAL ELECTROMAGNETICS

This chapter discusses the different time domain and frequency domain methods for solving Maxwell's equations [24], [55], [53], [67]. Section 4.1 introduces different popular methods for computational electrodynamics. Section 4.2 discusses finite difference time domain method which will be used for simulating magnetic transmission lines in MEEP simulator [64] introduced in Section 4.3.

### 4.1. METHODS FOR SOLVING MAXWELL'S EQUATIONS

The Maxwell's equations can be solved in time domain and frequency domain by solving partial differential equations or integral equations [24], [53]. Some of the methods are listed in the Table 4.1 below.

Table 4.1 Techniques for Solving Electromagnetic Problems

Method	Remark
<b>Adaptive Integral Method (AIM)</b>	Provides efficient iterative procedure for matrix algebra for linearized version of Maxwell's equations.
<b>Analytical Closed Form Techniques</b>	Approximate methods are used in cases with high degree of symmetry. Closed form solutions are not always possible.
<b>Bi-conjugate Gradient Method with Fast Fourier Transform (BCG-FFT)</b>	Useful in solving complex matrix equations resulting from the interactions of electromagnetic waves with surfaces.

<b>Boundary Element Method (BEM)</b>	Discretizes boundary elements to solve low frequency or steady state AC problems.
<b>Conjugate Gradient Method (CGM)</b>	Uses iterative method of conjugate gradients to solve systems involving large and sparse matrices.
<b>Fast Multipole Method (FMM)</b>	Uses approximations to solve for far field scalar potential.
<b>Finite Difference Frequency Domain Method (FDFD)</b>	Uses optimal discretization to solve time harmonic versions of linearized Maxwell's equations.
<b>Finite Difference Time Domain Method (FDTD)</b>	Maxwell's Equations are linearized using finite differences. Entire volume is uniformly discretized and fields are evolved by time stepping. Transient analysis of sharp edges increases resolution and computational time.
<b>Finite Element Method (FEM)</b>	Entire volume is non-uniformly discretized into homogeneous sub-regions. Field are computed by minimizing energy functions.
<b>Finite Integration Technique (FIT)</b>	Integral version of Maxwell's equations is solved in a non-uniformly meshed volume with very high resolution.
<b>Finite Volume Time Domain Method (FVTD)</b>	Entire volume is non-uniformly discretized and fields are evolved by time stepping.

<b>Generalized Multipole Technique (GMT)</b>	Surface charges and currents are used to determine frequency domain analytical field solutions using method of weighted residuals.
<b>Geometrical Optics (GO)</b>	Used for exact ray tracing for light wave propagation in optical media.
<b>Geometrical/ Uniform Theory of Diffraction (GTD/ UTD)</b>	Used for high frequency ray tracing and asymptotic solutions are used for solving diffraction problems.
<b>Hybrid Lumped Circuit and Quasi Transmission Line Method</b>	A hybrid method to accurately model lumped elements in microwave applications.
<b>Method of Moments (MoM)</b>	Wire mesh currents and patch surface currents are used to analyze complex inhomogeneous structures through the method of weighted residuals.
<b>Partial Element Equivalent Circuit Method (PEEC)</b>	A circuit of small electrical elements is used to approximate PCB radiation patterns.
<b>Shooting Bouncing Rays (SBR), Physical Optics (PO), Physical</b>	Planar surfaces are irradiated with electromagnetic field by transmitters. Receivers use detected radiation to compute local field.

<b>Theory of Diffraction (PTD)</b>	
<b>Singularity Expansion Method (SEM)</b>	Laplace transform with complex frequencies is used to detect characteristic resonance of complex scatterers.
<b>Spectral Domain Approach (SDA)</b>	Spatial Fourier transform is used to solve fields in spectral domain.
<b>Transmission Line Method (TLM)</b>	Complex nonlinear materials can be modeled using virtual transmission lines. The voltage and current inform about the fields.
<b>Vector Parabolic Equation Technique (VPE)</b>	Useful in radio communication systems.

After this brief review of computational electromagnetics, the next section discusses finite difference time domain method which will be used to simulate nonlinear, anisotropic, inhomogeneous magnetic transmission lines.

#### 4.2. INTRODUCTION TO FINITE DIFFERENCE TIME DOMAIN METHOD

Finite difference time domain method (FDTD) or K. Yee's method (1966) is a differential numerical modeling technique for computational electrodynamics [62], [63], [53], [55], [58], [57]. Finite difference time domain method [41] discretizes space into a grid of small elements called Yee lattice (1966) [62], [63], [57], [58]. One such element is shown in Figure 4.1. Each element can have a different conductivity, permittivity and permeability [58], [53].

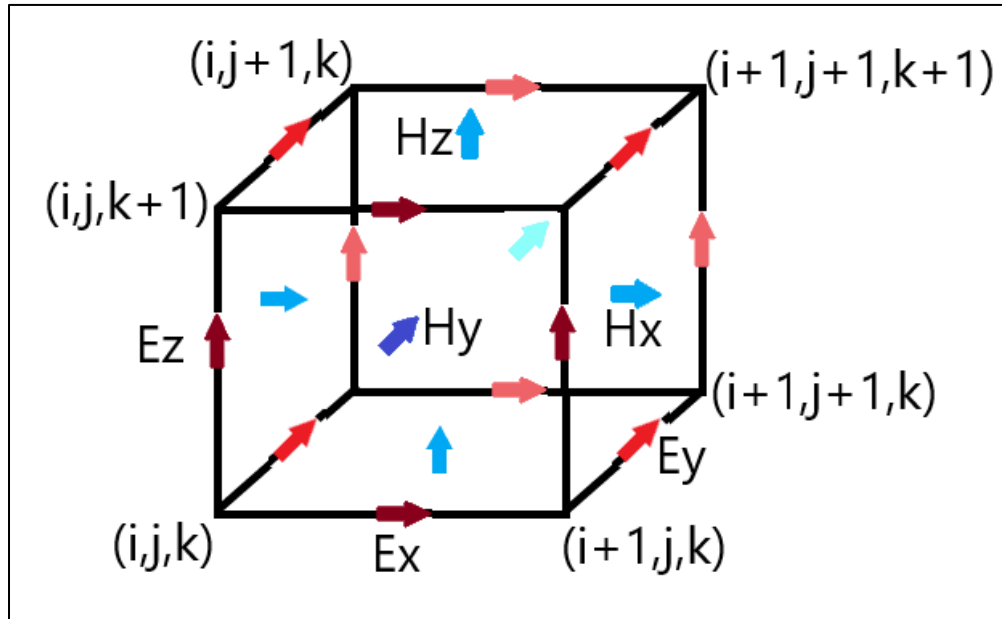


Figure 4.1 Location of Different Field Components in a Yee Cell

Maxwell's equations (1861) [24] are discretized using central difference approximations to the space and time partial derivatives. For example, Faraday's law in

Equation 4.1 and Equation 4.2 can be discretized as in Equation 4.3, Equation 4.4 and Equation 4.5.

$$\nabla \times \mathbf{E} = -\frac{d\mathbf{B}}{dt} \quad (4.1)$$

$$\nabla \times \mathbf{E} = \left( \frac{\Delta E_z}{\Delta y} - \frac{\Delta E_y}{\Delta z} \right) \mathbf{a}_x + \left( \frac{\Delta E_x}{\Delta z} - \frac{\Delta E_z}{\Delta x} \right) \mathbf{a}_y + \left( \frac{\Delta E_y}{\Delta x} - \frac{\Delta E_x}{\Delta y} \right) \mathbf{a}_z \quad (4.2)$$

$$\frac{\Delta E_y}{\Delta z} - \frac{\Delta E_z}{\Delta y} = \mu \frac{\Delta H_x}{\Delta t} \quad (4.3)$$

$$\frac{\Delta E_z}{\Delta x} - \frac{\Delta E_x}{\Delta z} = \mu \frac{\Delta H_y}{\Delta t} \quad (4.4)$$

$$\frac{\Delta E_x}{\Delta y} - \frac{\Delta E_y}{\Delta x} = \mu \frac{\Delta H_z}{\Delta t} \quad (4.5)$$

Similarly, Ampere's law in Equation 4.6 and Equation 4.7 can be approximated as in Equation 4.8, Equation 4.9 and Equation 4.10.

$$\nabla \times \mathbf{H} = \sigma \mathbf{E} + \frac{d\mathbf{D}}{dt} \quad (4.6)$$

$$\nabla \times \mathbf{H} = \left( \frac{\Delta H_z}{\Delta y} - \frac{\Delta H_y}{\Delta z} \right) \mathbf{a}_x + \left( \frac{\Delta H_x}{\Delta z} - \frac{\Delta H_z}{\Delta x} \right) \mathbf{a}_y + \left( \frac{\Delta H_y}{\Delta x} - \frac{\Delta H_x}{\Delta y} \right) \mathbf{a}_z \quad (4.7)$$

$$\frac{\Delta H_z}{\Delta y} - \frac{\Delta H_y}{\Delta z} = \sigma E_x + \varepsilon \frac{\Delta E_x}{\Delta t} \quad (4.8)$$

$$\frac{\Delta H_x}{\Delta z} - \frac{\Delta H_z}{\Delta x} = \sigma E_y + \varepsilon \frac{\Delta E_y}{\Delta t} \quad (4.9)$$

$$\frac{\Delta H_y}{\Delta x} - \frac{\Delta H_x}{\Delta y} = \sigma E_z + \varepsilon \frac{\Delta E_z}{\Delta t} \quad (4.10)$$

The different field components at a grid location are stored in the edges and faces of a cubic element called Yee cell. The fields are evolved in discrete time steps  $t_n = n\Delta t$  [62], [63] using leap frog method.

$$\left( \frac{E_y \Big|_{i,j,k+\frac{1}{2}}^n - E_y \Big|_{i,j,k-\frac{1}{2}}^n}{\Delta z} \right) - \left( \frac{E_z \Big|_{i,j+\frac{1}{2},k}^n - E_z \Big|_{i,j-\frac{1}{2},k}^n}{\Delta y} \right) = \mu_{i,j,k} \left( \frac{H_x \Big|_{i,j,k}^{n+\frac{1}{2}} - H_x \Big|_{i,j,k}^{n-\frac{1}{2}}}{\Delta t} \right) \quad (4.11)$$

$$\left( \frac{E_z \Big|_{i+\frac{1}{2},j,k}^n - E_z \Big|_{i-\frac{1}{2},j,k}^n}{\Delta x} \right) - \left( \frac{E_x \Big|_{i,j,k+\frac{1}{2}}^n - E_x \Big|_{i,j,k-\frac{1}{2}}^n}{\Delta z} \right) = \mu_{i,j,k} \left( \frac{H_y \Big|_{i,j,k}^{n+\frac{1}{2}} - H_y \Big|_{i,j,k}^{n-\frac{1}{2}}}{\Delta t} \right) \quad (4.12)$$

$$\left( \frac{E_x \Big|_{i,j+\frac{1}{2},k}^n - E_x \Big|_{i,j-\frac{1}{2},k}^n}{\Delta y} \right) - \left( \frac{E_y \Big|_{i+\frac{1}{2},j,k}^n - E_y \Big|_{i-\frac{1}{2},j,k}^n}{\Delta x} \right) = \mu_{i,j,k} \left( \frac{H_z \Big|_{i,j,k}^{n+\frac{1}{2}} - H_z \Big|_{i,j,k}^{n-\frac{1}{2}}}{\Delta t} \right) \quad (4.13)$$

$$\left( \frac{H_z \Big|_{i,j+\frac{1}{2},k}^n - H_z \Big|_{i,j-\frac{1}{2},k}^n}{\Delta y} \right) - \left( \frac{H_y \Big|_{i,j,k+\frac{1}{2}}^n - H_y \Big|_{i,j,k-\frac{1}{2}}^n}{\Delta z} \right) = \sigma \Big|_{i,j,k}^n (E_x \Big|_{i,j,k}^n) + \varepsilon_{i,j,k} \left( \frac{E_x \Big|_{i,j,k}^{n+\frac{1}{2}} - E_x \Big|_{i,j,k}^{n-\frac{1}{2}}}{\Delta t} \right) \quad (4.14)$$

$$\left( \frac{H_x \Big|_{i,j,k+\frac{1}{2}}^n - H_x \Big|_{i,j,k-\frac{1}{2}}^n}{\Delta z} \right) - \left( \frac{H_z \Big|_{i+\frac{1}{2},j,k}^n - H_z \Big|_{i-\frac{1}{2},j,k}^n}{\Delta x} \right) = \sigma \Big|_{i,j,k}^n (E_y \Big|_{i,j,k}^n) + \varepsilon_{i,j,k} \left( \frac{E_y \Big|_{i,j,k}^{n+\frac{1}{2}} - E_y \Big|_{i,j,k}^{n-\frac{1}{2}}}{\Delta t} \right) \quad (4.15)$$

$$\left( \frac{H_y \Big|_{i+\frac{1}{2},j,k}^n - H_y \Big|_{i-\frac{1}{2},j,k}^n}{\Delta x} \right) - \left( \frac{H_x \Big|_{i,j+\frac{1}{2},k}^n - H_x \Big|_{i,j-\frac{1}{2},k}^n}{\Delta y} \right) = \sigma \Big|_{i,j,k}^n (E_z \Big|_{i,j,k}^n) + \varepsilon_{i,j,k} \left( \frac{E_z \Big|_{i,j,k}^{n+\frac{1}{2}} - E_z \Big|_{i,j,k}^{n-\frac{1}{2}}}{\Delta t} \right) \quad (4.16)$$

The location of field components and the central difference operations implicitly enforce the two Gauss's laws [24].

The finite region of space must always be terminated with some boundary conditions. Some examples include Bloch-periodic boundaries, metallic walls and perfectly matched layers.

Bloch-periodic boundaries are used for simulation of periodic structures  $f(x) = f(x + L)e^{-jkL}$ . Periodic Bloch boundaries copy the field component at one cell's edge and reinject them at a neighboring cell's edge.

At metallic walls, all fields are forced to be zero hence it is a perfect reflector with zero absorption and zero skin depth.

Perfectly matched layers allow all the fields to pass through with minimal reflection. These absorbing boundary conditions (ABCs) absorb almost all of the incident field.



### 4.3. INTRODUCTION TO MEEP SIMULATOR

This section gives a brief introduction to MEEP [64] simulator designed for solving the Maxwell's equations [24] using discrete time stepping. MEEP [64] is a script based simulator for modeling the time domain [53] and frequency domain behavior of a variety of arbitrary materials. A fully scriptable open source C++ interface is provided for generating optimized algorithms. The use of normalized units for solving Maxwell's equations provides exceptional resolution in frequency and time domain. The simulator can be run on multicore supercomputers to speed up execution and transient analysis. A material library with sample data for several materials is provided in libraries for building accurate test structures. A wide variety of electric or magnetic soft current sources can be simulated. The fields can be printed as image or video files through data visualization features. G. Green's Functions (1835) give the field patterns from a localized point source at a particular frequency  $\omega$ . A frequency domain solver is also provided for multidimensional Fourier transformation (1822) and the decomposition of fields into travelling modes [68]. The 3-dimensional discrete Fourier transform (1822) of the response to a short impulse can give useful information about the transmitted power and losses [1], [2], [68], [23], [55]. Averaging, symmetry and integration are allowed in cylindrical and rectangular three dimensional coordinates. Hence different homogeneous/inhomogeneous structures can be built inside the space. Electric and magnetic energy density, Poynting flux etc. can be evaluated. The transmitted power can be computed using the integral of Poynting vector; over a surface on the far end of the transmission line. Transmitted power and incident power can be used to find power losses in transmission line.

$$P(\omega) = Re \left\{ \hat{n} \cdot \int E_{\omega}(x)^* \times H_{\omega}(x) d^2x \right\} \quad (4.17)$$

MEEP [64] can simulate anisotropic, dispersive [35], [38], non-linear [45] and gyrotropic media [49].

For anisotropic media, a non-diagonal susceptibility tensor shown in Equation 4.18 and Equation 4.19 is used to relate polarization/ magnetization and electric/ magnetic field intensity.

$$\mathbf{P} = \begin{bmatrix} \chi_{\perp} & -j\eta & 0 \\ j\eta & \chi_{\perp} & 0 \\ 0 & 0 & \chi_{\parallel} \end{bmatrix} \mathbf{E} \quad (4.18)$$

$$\mathbf{M} = \begin{bmatrix} \chi_{\perp} & -j\eta & 0 \\ j\eta & \chi_{\perp} & 0 \\ 0 & 0 & \chi_{\parallel} \end{bmatrix} \mathbf{H} \quad (4.19)$$

Drude-Lorentzian model (1900) models frequency dependent permittivity and permeability [35], [38]. It explains the electrodynamic properties of metals by regarding conduction band electrons as non-interacting electron gas. When the material is excited by an external source of resonant frequency, the material absorption loss increases greatly. electromagnetic energy is converted into other forms of energy. Flux densities contain terms for infinite frequency response and frequency dependent polarization vector [35].

$$\mathbf{D} = \varepsilon_{\infty} \mathbf{E} + \mathbf{P} \quad (4.20)$$

$$\mathbf{B} = \mu_{\infty} \mathbf{H} + \mathbf{M} \quad (4.21)$$

$\varepsilon$  and  $\mu$  are represented as a sum of harmonic resonances [35], [37] and a term for frequency independent electric conductivity as in Equation 4.22 and Equation 4.23.

$$\varepsilon(\omega, \mathbf{x}) = (1 + \frac{j\sigma_D}{\omega})(\varepsilon_{\infty}(\mathbf{x}) + \sum_N \frac{\sigma_n(\mathbf{x})\omega_n^2}{\omega_n^2 - \omega^2 + j\omega\gamma_n}) \quad (4.22)$$

$$\mu(\omega, \mathbf{x}) = (1 + \frac{j\sigma_B}{\omega})(\mu_{\infty}(\mathbf{x}) + \sum_N \frac{\sigma_n(\mathbf{x})\omega_n^2}{\omega_n^2 - \omega^2 + j\omega\gamma_n}) \quad (4.23)$$

$\sigma_D/\sigma_B$  is the electrical/magnetic conductivity.  $\sigma_n$  is the oscillator strength,  $\omega_n$  is the angular resonance frequency,  $\gamma_n$  is a damping factor.

The Pockels and Kerr non-linearity model (1875) explains how  $\varepsilon$  and  $\mu$  can change as a function of the field intensity [45], [33]. Ferromagnetic materials are non-linear [33], [46], [53] as their permeability varies with the strength of applied field intensity. At high magnetic field intensity, the material saturates, limiting further increase of magnetic flux [33]. Hence, the susceptibility decreases rapidly.

$$\mathbf{D} = (\varepsilon_{\infty}(\mathbf{x}) + \chi^{(2)}(\mathbf{x}).diag(\mathbf{E}) + \chi^{(3)}(\mathbf{x}).|\mathbf{E}|^2)\mathbf{E} + \mathbf{P} \quad (4.24)$$

$$\mathbf{B} = (\mu_{\infty}(\mathbf{x}) + \chi^{(2)}(\mathbf{x}).diag(\mathbf{H}) + \chi^{(3)}(\mathbf{x}).|\mathbf{H}|^2)\mathbf{H} + \mathbf{M} \quad (4.25)$$

$\chi^{(2)}$  sum is the Pockels effect constant; whereas  $\chi^{(3)}$  sum is the Kerr effect constant.

For gyrotropic media, Landau-Lifshitz-Gilbert model (1955) describes the precessional motion of saturated magnetic dipoles in a magnetic field [34], [49].

$$\frac{d\mathbf{M}}{dt} = \mathbf{b}_0 \times \left( -\sigma \mathbf{H} + \omega_0 \mathbf{M} + \alpha \frac{d\mathbf{M}}{dt} \right) - \gamma \mathbf{M} \quad (4.26)$$

$\mathbf{M}$  describes the linear deviation of magnetization from its static equilibrium value. Precession occurs around this unit bias vector  $\mathbf{b}_0$ .  $\sigma$  represents oscillator strength,  $\omega_0$  is the angular resonance frequency,  $\gamma$  is the oscillator damping factor and  $\alpha$  is the phenomenological Gilbert damping factor.

MEEP uses normalized units for solving Maxwell's equations. A scheme for conversion from SI units to MEEP units is shown in the table below.

Table 4.2 Conversion from SI Units to MEEP Units

Property	Symbol	Reference Scale in SI Units	SI to MEEP Conversion Factor
Length	$a_0$	$1.00000 \times 10^{-4} \text{ m}$	$\frac{1}{a_0} = 1.00000 \times 10^4$
Speed of Light	$c_0$	$2.99792 \times 10^8 \frac{\text{m}}{\text{s}}$	$\frac{1}{c_0} = 3.33564 \times 10^{-9}$
Current	$I_0$	1.00000 A	$\frac{1}{I_0} = 1.00000$
Time	$t_0$	$\frac{a_0}{c_0} = 3.33564 \times 10^{-13} \text{ s}$	$\frac{1}{t_0} = 2.99792 \times 10^{12}$
Frequency	$f_0$	$\frac{c_0}{a_0} = 2.99792 \times 10^{12} \text{ Hz}$	$\frac{1}{f_0} = 3.33564 \times 10^{-13}$
Permittivity	$\epsilon_0$	$8.85418 \times 10^{-12} \frac{\text{F}}{\text{m}}$	$\frac{1}{\epsilon_0} = 1.12940 \times 10^{11}$
Permeability	$\mu_0$	$1.25663 \times 10^{-6} \frac{\text{H}}{\text{m}}$	$\frac{1}{\mu_0} = 7.95774 \times 10^5$
Electric Field Intensity	$E_0$	$\frac{I_0}{a_0 \epsilon_0 c_0} = 3.76730 \times 10^6 \frac{\text{V}}{\text{m}}$	$\frac{1}{E_0} = 2.65441 \times 10^{-7}$
Electric Flux Density	$D_0$	$\frac{I_0}{a_0 c_0} = 3.33564 \times 10^{-5} \frac{\text{C}}{\text{m}^2}$	$\frac{1}{D_0} = 2.99792 \times 10^4$
Magnetic Field Intensity	$H_0$	$\frac{I_0}{a_0} = 1.00000 \times 10^4 \frac{\text{A}}{\text{m}}$	$\frac{1}{H_0} = 1.00000 \times 10^{-4}$

<b>Magnetic Flux Density</b>	$B_0$	$\frac{I_0}{a_0 \varepsilon_0 c_0} = 1.25663 \times 10^{-2} \frac{Wb}{m^2}$	$\frac{1}{B_0} = 7.95774 \times 10^1$
<b>Electric Conductivity</b>	$\sigma_0$	$\frac{\varepsilon_r \varepsilon_0 c_0}{a_0} = 2.65441 \times 10^1 \frac{A}{Vm}$	$\frac{1}{\sigma_0} = 3.7673 \times 10^{-2}$
<b>Electric Current Density</b>	$J_0$	$\frac{I_0}{a_0 a_0} = 1.00000 \times 10^8 \frac{A}{m^2}$	$\frac{1}{J_0} = 1.00000 \times 10^{-8}$
<b>Energy Density</b>	$U_0$	$\frac{I_0 I_0}{a_0 a_0 \varepsilon_0 c_0} = 1.25663 \times 10^2 \frac{J}{m^3}$	$\frac{1}{U_0} = 7.95774 \times 10^{-3}$
<b>Poynting Vector</b>	$S_0$	$\frac{I_0 I_0}{a_0 a_0 \varepsilon_0 c_0} = 3.76730 \times 10^{10} \frac{W}{m^2}$	$\frac{1}{S_0} = 2.65441 \times 10^{-11}$
<b>Courant Factor</b>	$S_{c0}$	$\frac{1}{c_0} = 3.33564 \times 10^{-9} \frac{s}{m}$	$\frac{1}{S_{c0}} = 2.99792 \times 10^8$

This chapter discussed the different time domain and frequency domain methods for solving Maxwell's equations [24], [55], [53], [67] with special focus on the finite difference time domain method; which was used for simulating magnetic transmission lines in MEEP simulator [64].

## 5. MAGNETIC TRANSMISSION LINE SIMULATION

This chapter presents simulations of magnetic transmission lines for studying the transient response of ferromagnetic materials. The results of the transmission line model were verified against simulation results in MEEP [64].

The electromagnetic simulations were carried out in MEEP [64] simulator which is a script based finite difference time domain [62], [63], [57], [58], [41] electromagnetic simulator for solving Maxwell's equations [24].

Lumped circuits [54] were used for studying linear, time invariant, distributed systems like magnetic transmission lines [4], [5], [6], [7], [8]. The distributed parameters were calculated using mathematical formulas. MATLAB was used for modeling the time and frequency domain behavior of magnetic transmission lines [4], [5], [6], [7], [8] in terms of simplified lumped circuits.

Finite difference time domain [62], [63], [57], [58], [41] electromagnetic field MEEP [64] simulations were carried out for dispersive [35], [38] magnetic transmission lines [4], [5], [6], [7], [8] in anisotropic, inhomogeneous, non-linear media [45], [69], [53]. The magnetic transmission lines [4], [5], [6], [7], [8] were constructed using Drude-Lorentz susceptibility models for ferromagnetic conductors like Manganese-Zinc alloy. The transmission lines were excited using continuous point sources. The terminations were modeled by perfectly matched layers for surge impedance loading; or as perfect reflectors for no load test. Some applications of the simulations include wideband transformer [70], [69], [71], [56], [28], [1], [2] and transmission line transformer [72], [73].

### 5.1. SIMULATION OF DISPERSIVE MAGNETIC TRANSMISSION LINE

In order to study their frequency response to continuous sources, finite difference frequency domain [67] electromagnetic field MEEP [64] simulations were carried out. The multi-dimensional Fourier transform and mode decomposition were used for this study [74]. In order to simplify analysis, the distributed system was linearized to obtain a lumped model. The frequency domain behavior was studied using transfer function of equivalent T-model transmission line circuit.

Multi-conductor transmission lines introduce many complexities like capacitive/inductive coupling. MEEP [64] simulations and MATLAB lumped circuit calculations [54] were carried out for studying cross talk between conductors of multi-wire magnetic transmission lines.

As in the case of electric transmission lines, power flow equations were used for magnetic transmission lines [4], [5], [6], [7], [8] in terms of lumped parameters; like per unit length transverse impedance and the per unit length longitudinal admittance. The results were also verified using electromagnetic simulations.

The electromagnetic MEEP [64] simulations helped to probe the stored electric/magnetic energy density, geometric parameters, per unit length losses and transmission efficiency of magnetic transmission lines. Among the different magnetic materials, the best alloy can be chosen based on desired performance metrics. A suitable candidate must exhibit minimal radiation and line losses. The transverse impedance and longitudinal admittance dictate the propagation of wave modes in magnetic transmission lines [4], [5], [6], [7], [8]. Simulations were used to estimate per unit length transverse inductance and longitudinal capacitance [11], which contribute to the transverse impedance and



longitudinal admittance respectively. These parameters are pivotal in determining the lumped model of the distributed transmission line system.

The magnetic transmission lines [4], [5], [6], [7], [8] was excited by continuous sources to examine their frequency response. The Fourier transform decomposed the fields into the various travelling wave modes. This can aid the study of the effects of magnetic hysteresis [33], [30], [31], [32] and saturation on power quality [41]. The T-model equivalent magnetic circuits [54] and coupled equations were used to simplify analysis of the transient [41] and steady state behavior. According to theory, magnetic transmission lines [4], [5], [6], [7], [8] must exhibit the behavior of a high pass filter, blocking all DC signals. DC signals produce the most severe transients in electric transmission lines [41]; which behave like a low pass filter. However, this also implies that magnetic transmission lines [4], [5], [6], [7], [8] must be operated at higher frequencies than electric transmission lines. Poorly designed magnetic transmission lines [4], [5], [6], [7], [8] may amplify high frequency noise which can be damaging for the power system. The imaginary part of transmission line magnetic reluctance, which is a strong function of frequency, contributes to line losses. Hysteresis losses [33], [30], [31], [32] also increase significantly at higher frequencies [3], [41], [1], [2]. Hence, an appropriate frequency must be chosen, considering the complex nature of the magnetic material.

The study of capacitive/ inductive coupling in multi-conductor transmission lines can provide useful knowledge about the radiated/ conducted emissions and susceptibility. The generator-receptor model is well suited for studying electromagnetic interference and electromagnetic compatibility of magnetic transmission lines [4], [5], [6], [7], [8]. The results can be compared with mathematical formulas to build linear circuit models [54] for

cross talk between magnetic transmission lines [4], [5], [6], [7], [8]. The aim will be to minimize electromagnetic radiation; that can be picked up by intentional receivers like radio and television; or unintentional receivers like digital computers. This will prevent malfunction of the sensitive electronic equipment.

Power flow equations for magnetic transmission lines [4], [5], [6], [7], [8] can help to compare the electromagnetic and magnetic circuit models. The power flow can be represented in the form of magnetic displacement current and magnetic voltage for circuit model. For the electromagnetic model, the power flow can be represented in the form of magnetic field and electric field. Accurate estimation of lumped parameters; like per unit length transverse impedance and the per unit length longitudinal admittance is necessary for producing a valid lumped magnetic circuit [54] for magnetic transmission lines [4], [5], [6], [7], [8].

The overview of the simulation algorithm is shown in Figure 5.1.

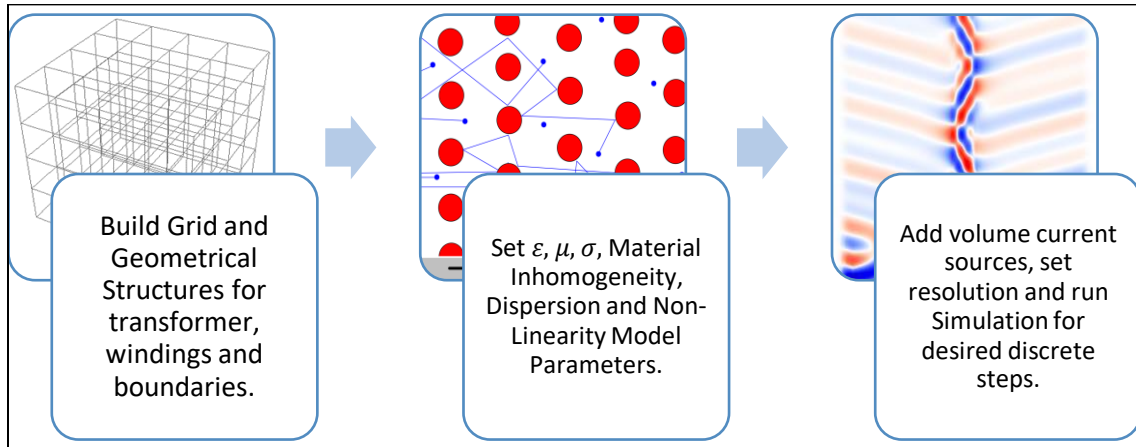


Figure 5.1 Overview of MEEP Algorithm for Simulation of Magnetic Transmission Line

The magnetic transmission line [4], [5], [6], [7], [8] was constructed for studying inhomogeneous, dispersive [35], [38], non-linear [45] ferromagnetic substances [46] like manganese-zinc alloy. The Transmission Lines was excited using continuous current

sources. The terminations were modeled by perfectly matched layers for complete absorption; or as perfect reflectors for no load.

The relative permittivity of the magnetic transmission line was 10 and the electric conductivity was  $5 \times 10^{-3} S/m$ . The magnetic permeability was a non-linear function of frequency as in Equation 5.1.

$$\mu_r(\omega, x) = \left( \mu_{r\infty} + \frac{\sigma \omega_0^2 (\omega_0^2 - \omega^2 + j\omega\gamma)}{(\omega_0^2 - \omega^2 + j\omega\gamma)^2 - \omega^2 b^2} \right) \quad (5.1)$$

where  $\mu_{\infty}(x) = 1$ ,  $\sigma_0(x) = 10000$ ,  $\omega_0 = 1.73 \text{ MHz}$ ,  $\gamma_0 = -0.0033$

The geometry of the simulated magnetic transmission line is shown in Figure 5.2 below. The electric current source is represented by a current loop. The magnet flux and magnetic displacement current flows in the z-direction.

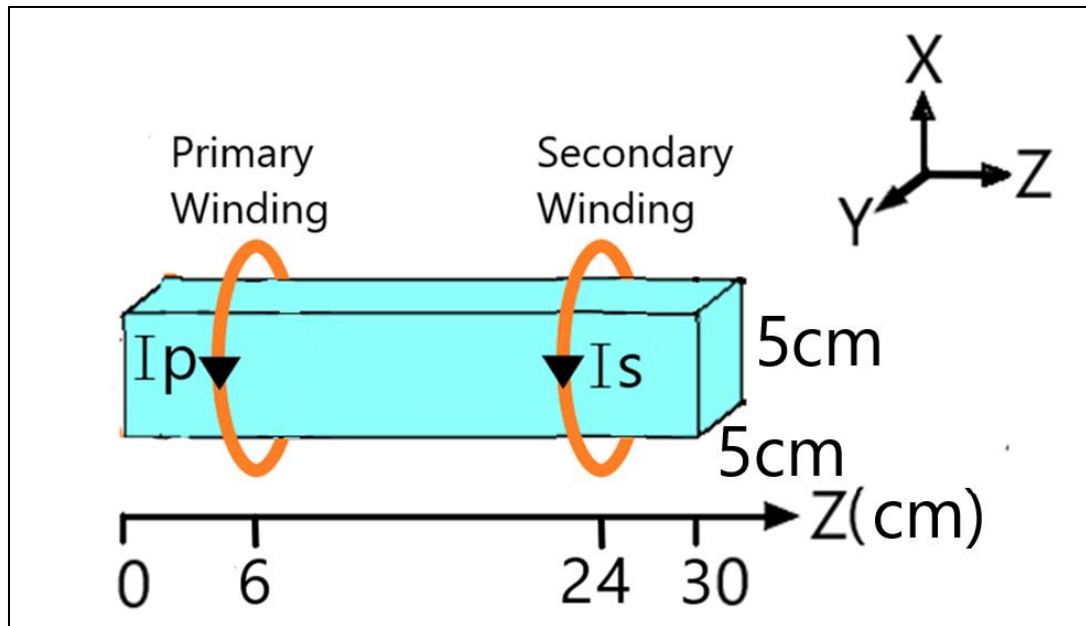
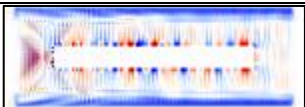
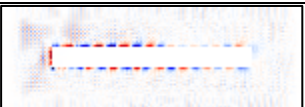
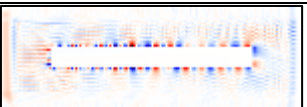
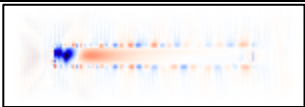
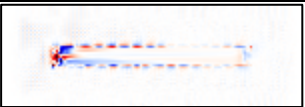
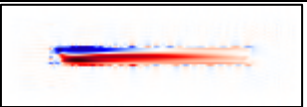

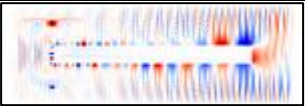
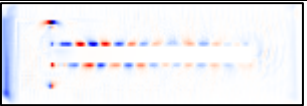

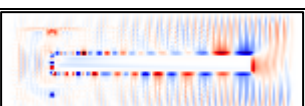
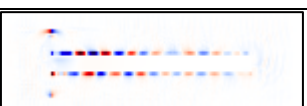


Figure 5.2 Geometry of Simulated Magnetic Transmission Line and Current Source

### 5.1.1. Visualization Of Electromagnetic Fields

The Longitudinal Fields of the simulated transmission line are shown in the Table 5.1 below.

Table 5.1 Longitudinal Field Components



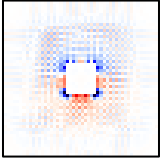
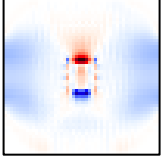
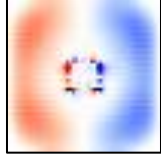
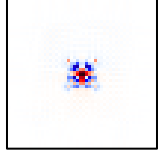
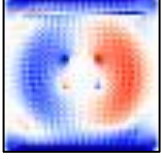
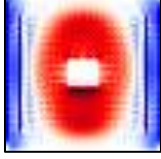
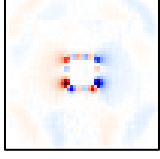
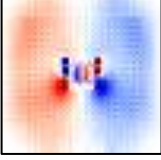

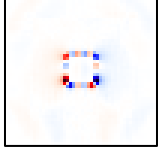
	Component		
Field	X	Y	Z
<b>H</b>			
<b>B</b>			
<b>E</b>			
<b>D</b>			

The magnetization fields  $H_x$ ,  $H_y$  and  $H_z$  are almost zero inside the magnetic transmission line due to high magnetic permeability of the ferromagnetic material. The longitudinal magnetic field  $B_z$  is very intense inside the transmission line as a large amount of flux flows through it. The intense longitudinal  $H_x$  field around the transmission line

results due to magnetic flux leakage. The transverse  $E_x$ ,  $E_y$ ,  $D_x$  and  $D_y$  show that electric fields encircle the transmission line.

The Transverse Fields of the simulated transmission line are shown in the Table 5.2 below.

Table 5.2 Transverse Field Components

	Component		
Field	X	Y	Z
<b>H</b>			
<b>B</b>			
<b>E</b>			
<b>D</b>			

The magnetization fields  $H_x$ ,  $H_y$  and  $H_z$  are almost zero inside the magnetic transmission line due to high magnetic permeability of the ferromagnetic material. Intense Transverse  $H_x$  and  $H_y$  fields show that H field radiates out from the magnetic transmission

line in straight paths. The Magnetic Flux Density  $B_z$  is mainly confined inside the transmission Line.  $B_x$  and  $B_y$  components result from the magnetic leakage flux. The transverse  $E_x$ ,  $E_y$ ,  $D_x$  and  $D_y$  show that electric fields encircle the transmission line.

### 5.1.2. Variation Of Permeability With Frequency

The magnetic permeability was modeled using Drude-Lorentzian function as in Equation 5.1.

$$\mu_r(\omega, x) = \left( \mu_{r\infty} + \frac{\sigma \omega_0^2 (\omega_0^2 - \omega^2 + j\omega\gamma)}{(\omega_0^2 - \omega^2 + j\omega\gamma)^2 - \omega^2 b^2} \right) \quad (5.1)$$

where  $\mu_{\infty}(x) = 1$ ,  $\sigma_0(x) = 10000$ ,  $\omega_0 = 1.73 \text{ MHz}$ ,  $\gamma_0 = -0.0033$

The dispersion of permeability from datasheet and simulation is shown in the Figure 5.3.

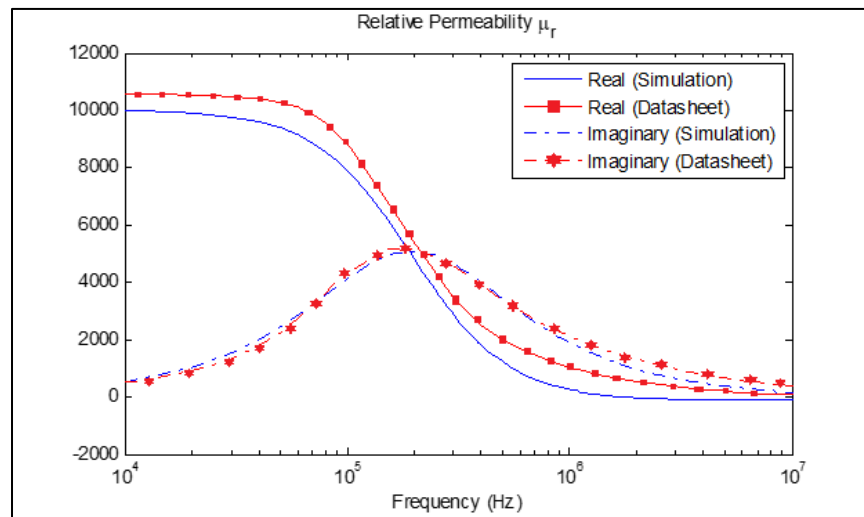


Figure 5.3 Variation of Relative Permeability with Applied Magnetic Field Frequency



The relative permittivity of the magnetic transmission line was 10 and the electric conductivity was  $5 \times 10^{-3} S/m$ . The MEEP code is given in Appendix A.

The discrete Fourier transform of the soft magnetic Gaussian pulse is shown in Figure 5.4 below. The Gaussian pulse is centered at 5 GHz with a bandwidth of 10 GHz.

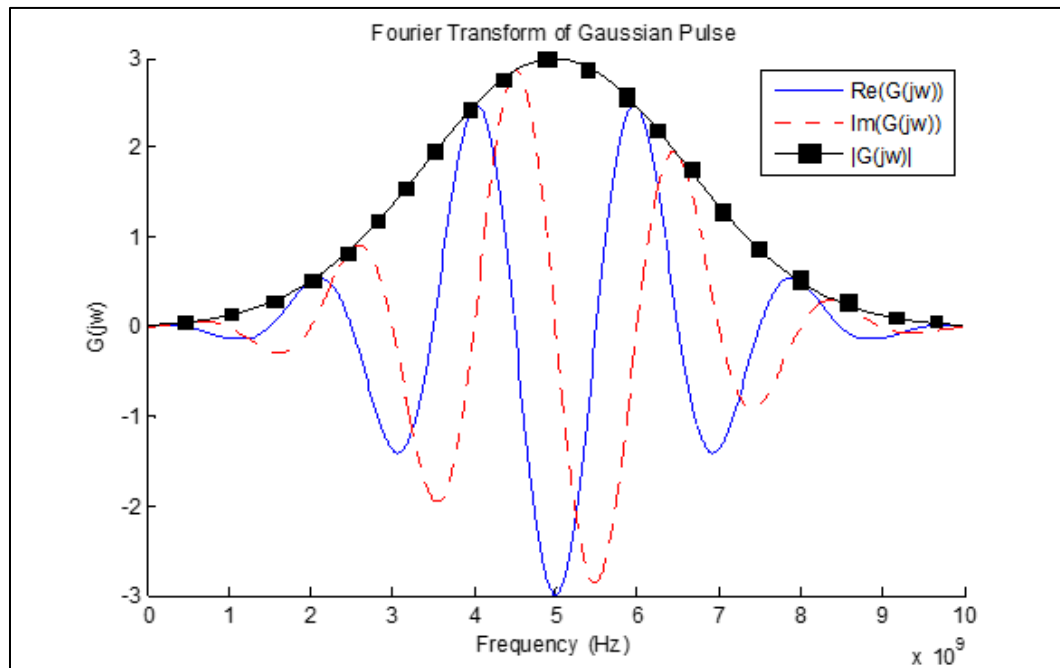


Figure 5.4 Discrete Fourier Transform of Gaussian Pulse

### 5.1.3. Attenuation Of Magnetic Field Along The Direction Of Propagation

The Figure 5.5 below shows the decay of magnetic field along the length of the magnetic path. The wave front of the axial magnetic field evolves over time, spreading across the length of the line. The field is plotted in logarithmic scale to show the decay of the wave front as it propagates. When the wave front hits the opposite end, it is reflected so the final profile approaches a standing wave of constant magnitude.

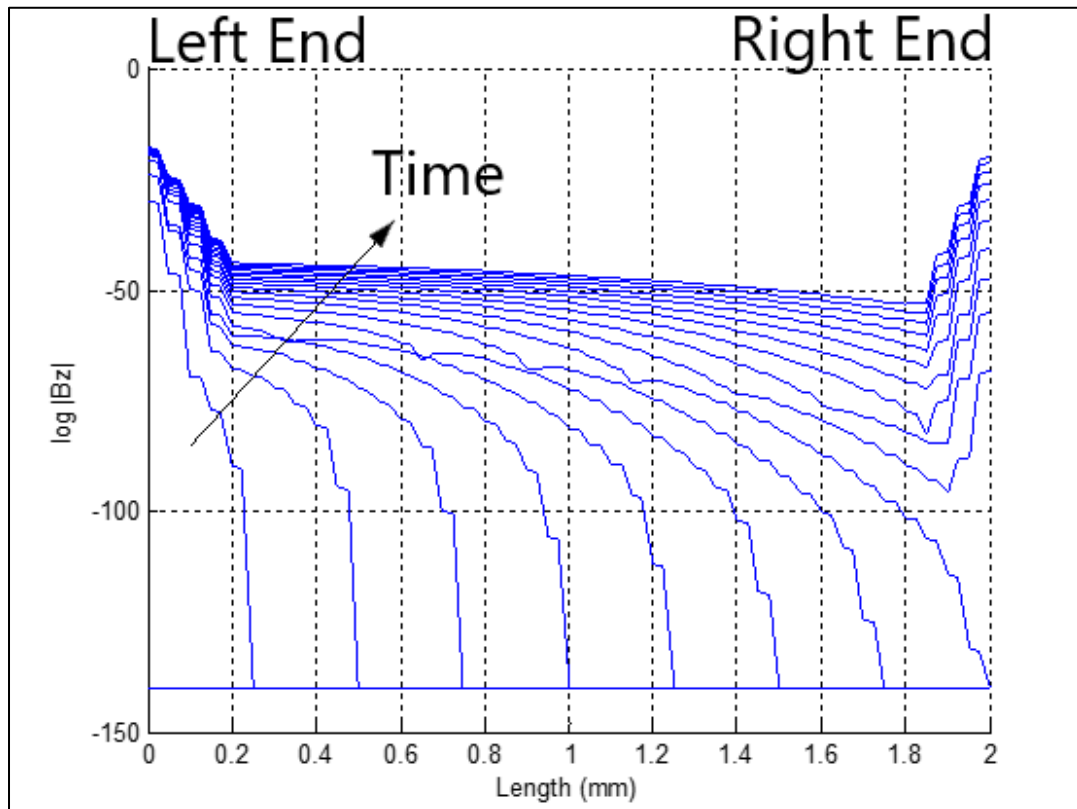


Figure 5.5 Evolution of Pulse Wave front Across the Length of Transmission Line

#### 5.1.4. Skin Effect In Magnetic Transmission Line

The electromagnetic fields decay very strongly inside the lossy transmission line due to skin effect.

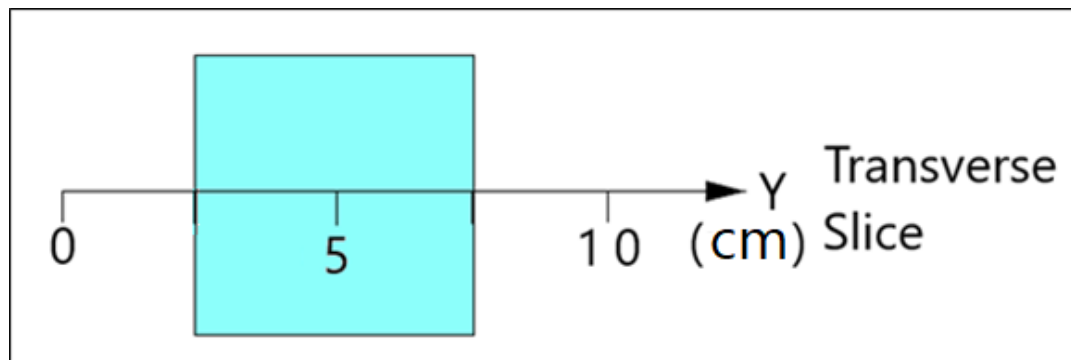


Figure 5.6 A Transverse Slice of the Magnetic Transmission Line

The amplitudes of fields are plotted for a transverse slice of the ferromagnetic material in Figure 5.7. The fields attenuate exponentially inside the ferromagnetic material. The attenuation increases at high frequencies.

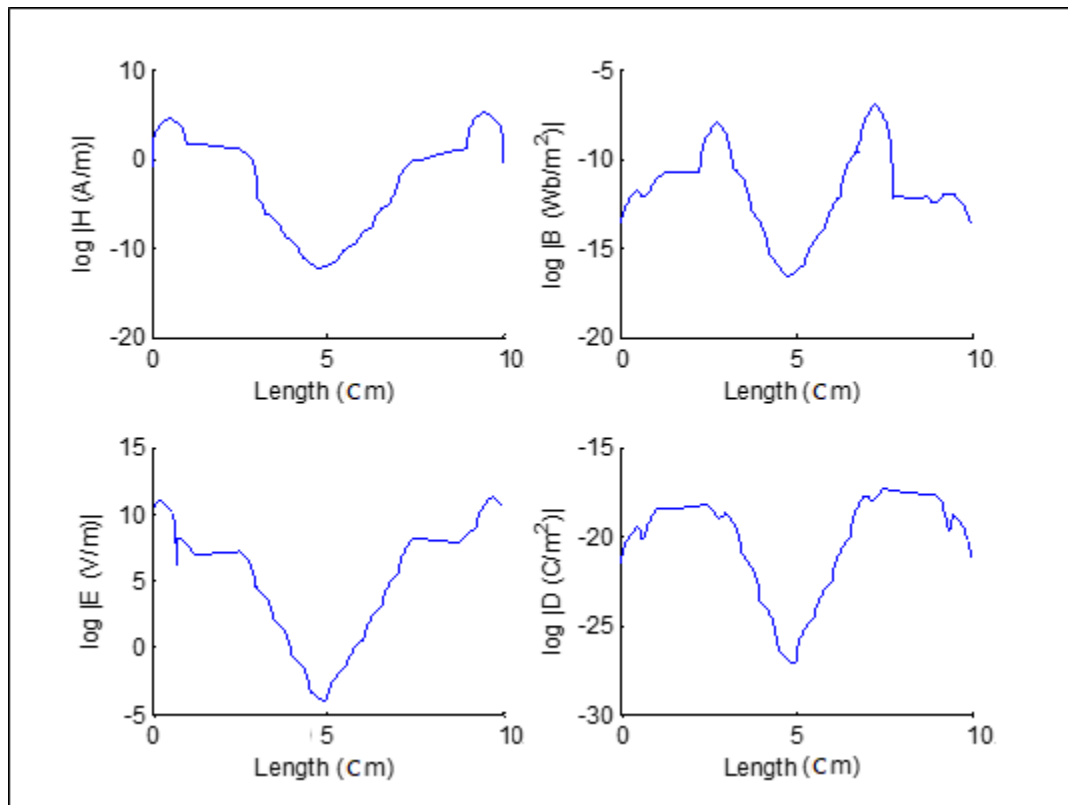


Figure 5.7 Decay of Electromagnetic Fields inside Lossy Magnetic Material

### 5.1.5. Evolution Of Magnetic Displacement Current And Voltage

The magnetic voltage was calculated using Equation 3.29:

$$V_m = \int_a^b \mathbf{H}_r \cdot d\mathbf{r}$$

The line integral of radial magnetic field was evaluated from an arbitrary point (assumed to be at zero magnetic voltage) which is far from the transmission line, to the surface of the transmission line, along the radial direction. It is assumed that the radial magnetic field is uniform along all directions.

The magnetic displacement current  $I_m$  was calculated using Equation 3.31:

$$I_m = -\frac{d\Phi_m}{dt} = \oint \mathbf{E} \cdot d\mathbf{l}$$

The closed line integral of the electric field encircling the cuboid magnetic transmission line was calculated using four discrete line integrals along a square path. The line integral of electric field along the square path encircling the transmission line gave the value of enclosed magnetic current. The MEEP code is given in Appendix A.

The evolution of magnetic voltage and current is shown in Figure 5.8.

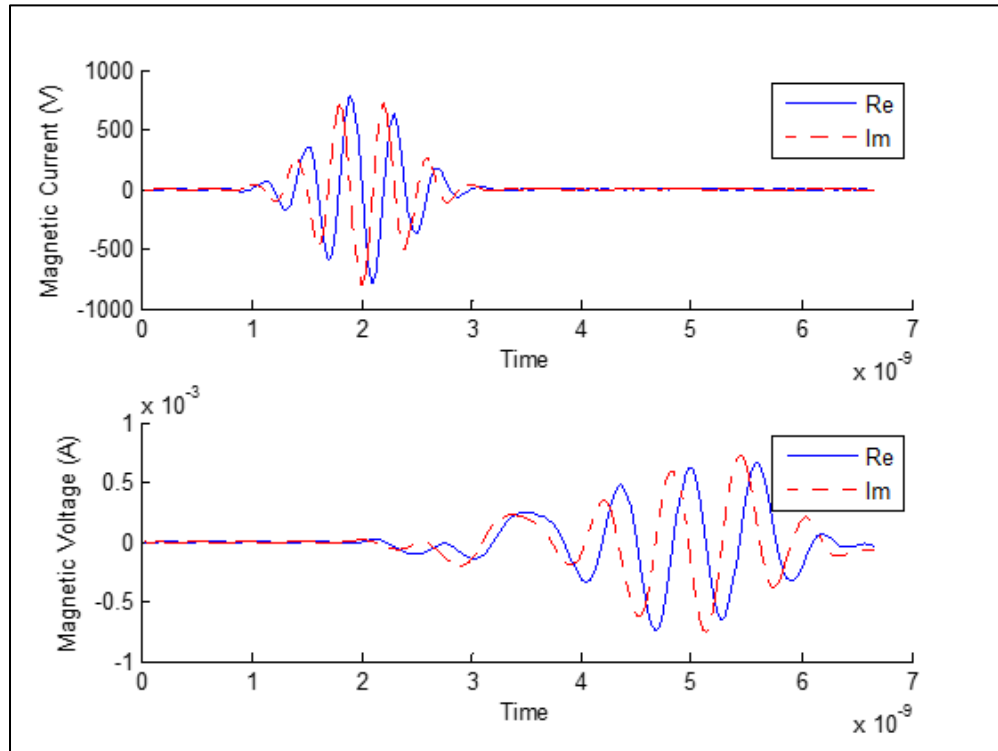


Figure 5.8 Evolution of Magnetic Displacement Current and Magnetic Voltage upon Application of Gaussian Pulse

Magnetic voltage and magnetic current are complex signals with real and imaginary components. The real and imaginary components are phase shifted to transmit active and reactive power. The magnetic voltage lags the magnetic current because the transmission line acts as an inductor which resists changes in magnetic voltage.

### 5.1.6. Intrinsic Wave Impedance Of Magnetic Transmission Line

The intrinsic wave impedance was calculated using the relationship in Equation 5.2. The dependence of intrinsic wave impedance on frequency is shown in Figure 5.9. The simulation and theory results are shown for the range 1 MHz – 1 GHz. The intrinsic wave impedance was high at low frequencies because of high magnetic permeability. At 10GHz, the relative permeability approached the value 1.0. The intrinsic impedance approached the estimated value of  $\frac{377\sqrt{\mu_r}}{\sqrt{\epsilon_r}} = \frac{377}{\sqrt{10}} = 119\Omega$ . As shown in Figure 5.9, the simulation results have a strong match with the theory results. The MATLAB code is given in Appendix B.

$$Z_w(j\omega) = \frac{E_x(j\omega)}{H_x(j\omega)} = \sqrt{\frac{j\omega L_T}{G_L + j\omega C_L}} \quad (5.2)$$

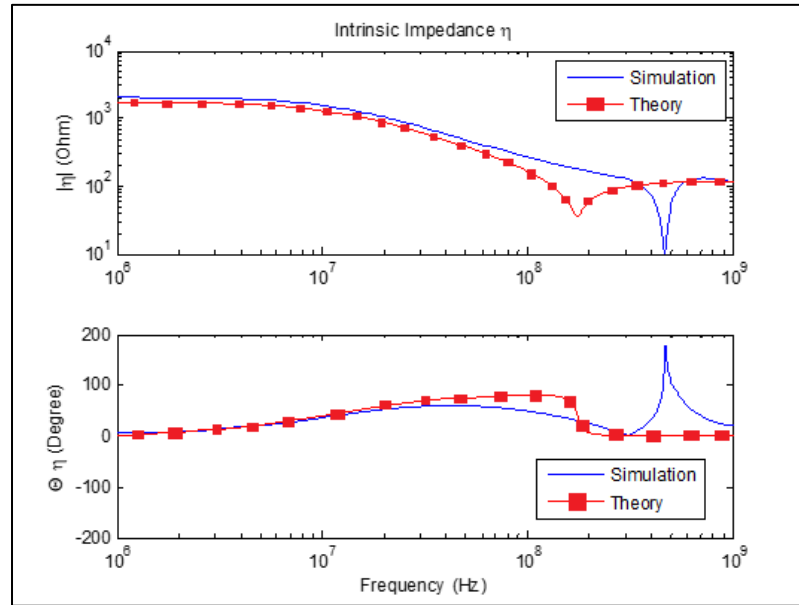


Figure 5.9 Variation of Wave Impedance Magnitude and Angle with Frequency

### 5.1.7. Attenuation Constant And Phase Constant Of Magnetic Transmission Line

The Attenuation constant was calculated using Equation 5.3. The dependence of wave propagation constant on frequency is shown in Figure 5.10. The simulation and theory results are shown for the range 1 MHz – 1 GHz. The attenuation constant increased with frequency since skin effect increases sharply at high frequencies. After 100 MHz, the permeability and magnetic conductance became very low, hence the attenuation constant dropped. As frequency increased, the phase constant dropped because the magnetic permeability decreased sharply. After 300 MHz, the effect of decreasing permeability was nullified by the increasing frequency, and the ferrite started to behave like a dielectric. The simulation results have a strong match with the theory results. The MATLAB code is given in Appendix B.

$$\gamma(j\omega) = \frac{-1}{L} \log \left( \frac{H_x(d=L)}{H_x(d=0)} \right) = \sqrt{(j\omega L_T)(G_L + j\omega C_L)} = \alpha + j\beta \quad (5.3)$$

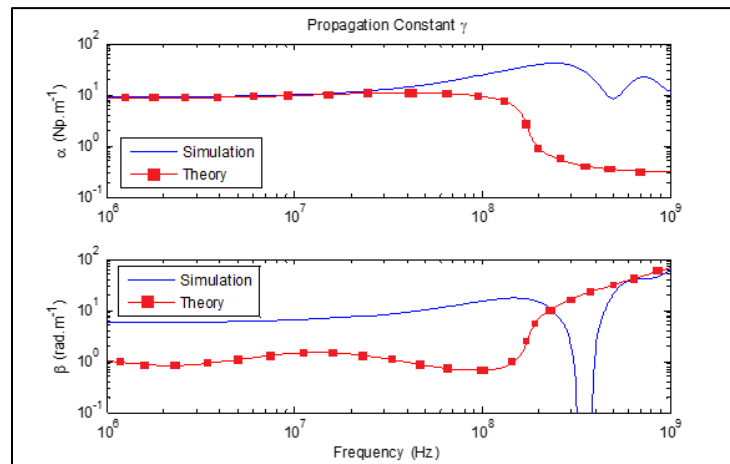


Figure 5.10 Variation of Attenuation Constant, Phase Constant and Phase Velocity with Frequency



The dependence of phase velocity on frequency is shown in Figure 5.11. The simulation and theory results are shown for the range 1 MHz – 1 GHz. Phase velocity was very small at 1 MHz due to high relative permeability. The phase velocity approached the limiting velocity  $\frac{3 \times 10^8 \text{ m/s}}{\sqrt{\mu_r \epsilon_r}} = \frac{3 \times 10^8 \text{ m/s}}{\sqrt{10}} = 9.48 \times 10^7 \text{ m/s}$  as the frequency increased and the core relative permeability approached 1.0. The phase velocity approached superluminal value near 300 MHz. The simulation results have a strong match with the theory results.

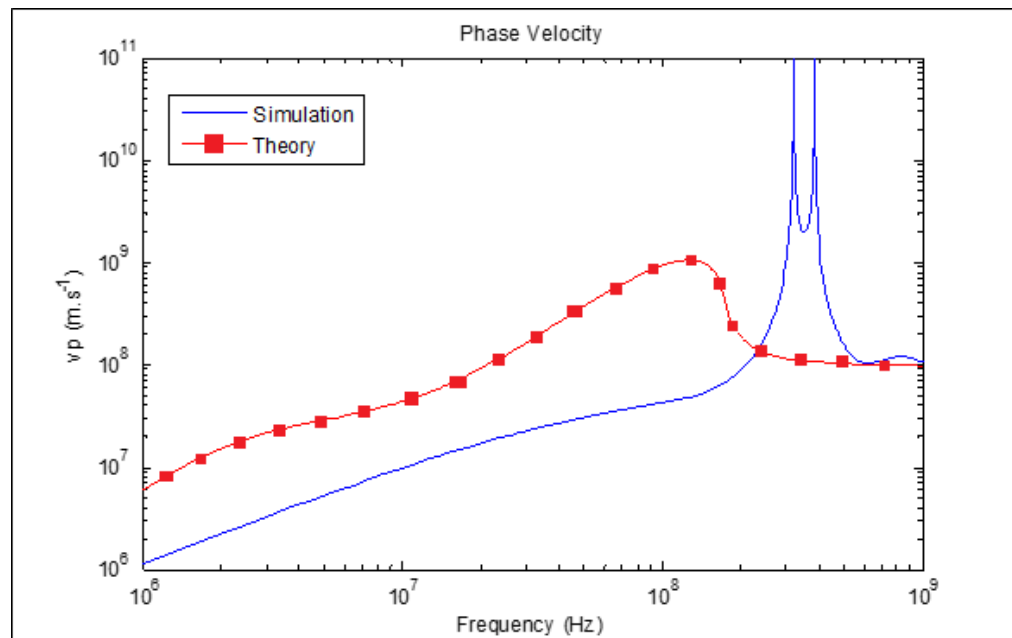


Figure 5.11 Variation of Phase Velocity with Frequency

### 5.1.8. Magnetic Admittance Of Magnetic Transmission Line

The Magnetic Admittance was calculated using the following Equation 5.4. The dependence of longitudinal admittance on frequency is shown in Figure 5.12. The simulation and theory results are shown for the range 1 MHz – 1 GHz. The magnetic conductance and magnetic susceptance were complex functions of material permittivity, permeability and geometry. The magnetic reluctance increased with frequency hence magnetic losses increased as well. The magnetic capacitance became very high at 1 GHz, hence the magnetic flux leakage increased heavily. The simulation results have a strong match with the theory results. The MATLAB code is given in Appendix B.

$$Y_L(j\omega) = \frac{\gamma(j\omega)}{Z_w(j\omega)} = \sqrt{(j\omega L_T)(G_L + j\omega C_L)} \sqrt{\frac{G_L + j\omega C_L}{j\omega L_T}} = G_L + j\omega C_L \quad (5.4)$$

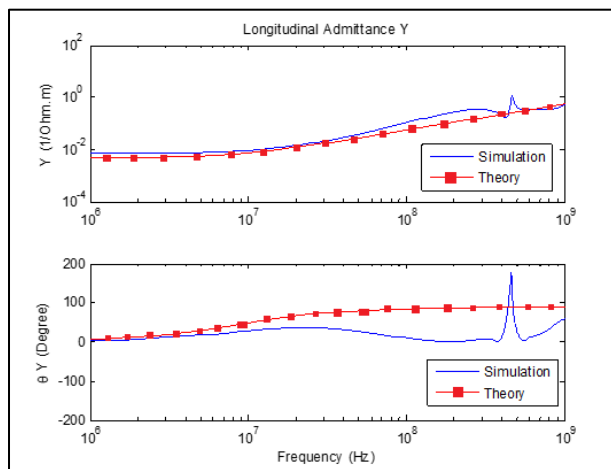


Figure 5.12 Variation of Magnetic Conductance, Magnetic Reluctance and Magnetic Capacitance with Frequency

### 5.1.9. Magnetic Impedance Of Magnetic Transmission Line

The Magnetic Impedance was calculated using Equation 5.5. The dependence of transverse impedance on frequency is shown in Figure 5.13. The simulation and theory results are shown for the range 1 MHz – 1 GHz. The Magnetic reactance was small at low frequencies. As the frequency is increased, it started increasing at first, but soon the permeability decreased and the reactance dropped. This is responsible for high frequency droop in wideband transformers. The simulation results have a strong match with the theory results. The MATLAB code is given in Appendix B.

$$Z_T(j\omega) = Z_w(j\omega)\gamma(j\omega) = \sqrt{(j\omega L_T)(G_L + j\omega C_L)} \sqrt{\frac{j\omega L_T}{G_L + j\omega C_L}} = j\omega L_T \quad (5.5)$$

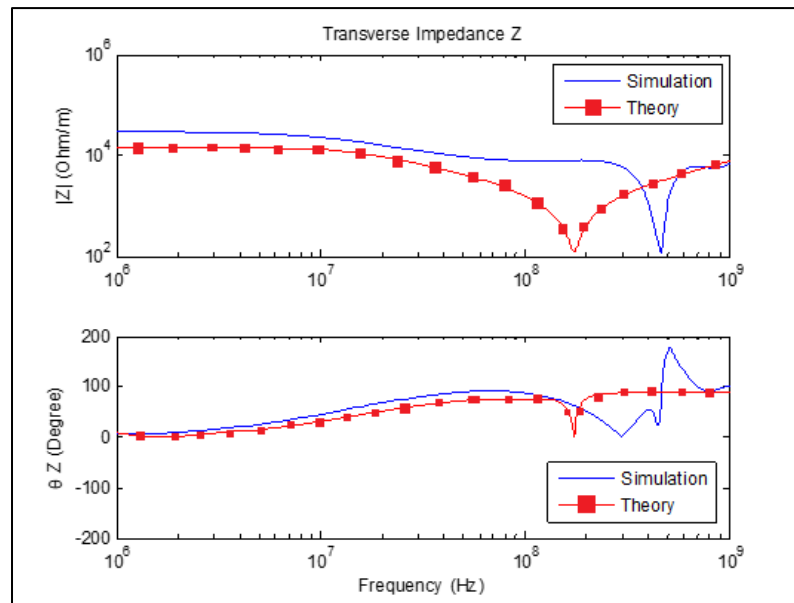


Figure 5.13 Variation of Magnetic Inductance with Frequency

## 5.2. SIMULATION OF GYROMAGNETIC TRANSMISSION LINE

In this section, a Gyromagnetic Ferrite will be presented to study the effects of frequency and Gilbert damping constant on Magnetic Transmission Lines parameters. Landau-Lifshitz-Gilbert model presented in Equation 5.6 describes the damped precessional motion of saturated magnetic dipoles in a static bias magnetic field.

$$\frac{d\mathbf{M}}{dt} = \mathbf{b} \times \left( -\sigma \mathbf{H} + \omega_0 \mathbf{M} + \alpha \frac{d\mathbf{M}}{dt} \right) - \gamma \mathbf{M} \quad (5.6)$$

$\mathbf{M}$  describes the linear deviation of magnetization from its static equilibrium value.  $\mathbf{M}$  precesses around bias field vector  $\mathbf{b}$ .  $\sigma$  couples the magnetization to the driving field  $\mathbf{H}$ ,  $\omega_0$  is the angular frequency of precession,  $\gamma$  is the oscillator damping factor and  $\alpha$  is the phenomenological Gilbert damping factor.

For ferromagnetic media biased in the z-direction, a non-diagonal susceptibility tensor, shown in Equation 5.7, is used to relate magnetization  $\mathbf{M}$  and field intensity  $\mathbf{H}$ .

$$\mathbf{M} = [\chi] \mathbf{H} = \begin{bmatrix} \chi_{11} & -j\chi_{12} & 0 \\ j\chi_{22} & \chi_{22} & 0 \\ 0 & 0 & \chi_{33} \end{bmatrix} \begin{bmatrix} H_x \\ H_y \\ H_z \end{bmatrix} \quad (5.7)$$

$$\text{where } \chi_{11} = \chi_{22} = \frac{\sigma(\omega_0 - i\omega\alpha)}{(\omega_0 - i\omega\alpha)^2 - (\omega + i\gamma)^2}, \chi_{12} = \chi_{21} = \frac{\sigma(\omega + i\gamma)}{(\omega_0 - i\omega\alpha)^2 - (\omega + i\gamma)^2}, \chi_{33} = 0, \omega_0 =$$

$$30 \text{ GHz}, \gamma = 0.001, \alpha = 0.00001, \sigma = 0.1$$

The ferrite resonates when 30 GHz signal is applied; as shown in Figure 5.14.

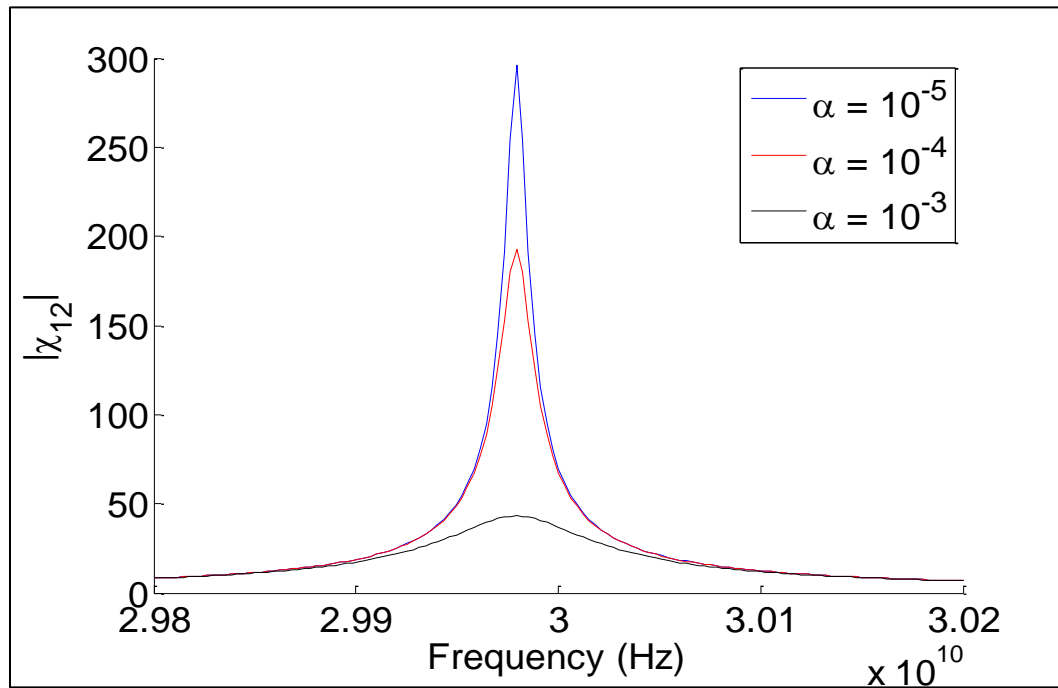


Figure 5.14 Ferromagnetic Resonance of Susceptibility Tensor Element  $\chi_{12}$

The Gyromagnetic Ferrite was excited by a 30 GHz linearly polarized sinusoid source. The Temporal and Spatial resolution was  $\Delta t = 66 \text{ ps}$  and  $\Delta x = 200 \mu\text{m}$ .

The Polarization of the linearly Polarized wave changes as it moves across the saturated ferrite. The precession of Magnetization around the bias can be seen in Figure 5.15 and Figure 5.16.

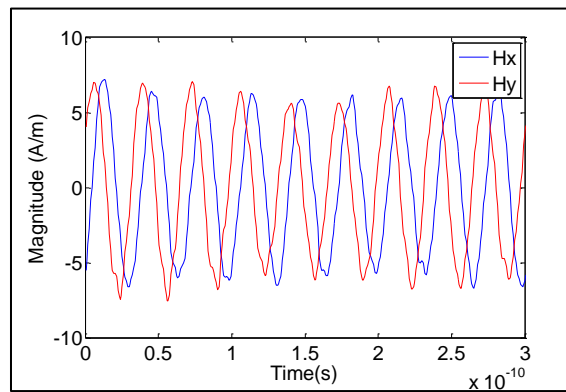


Figure 5.15 The Hx and Hy Components Precess Around the Hz Bias

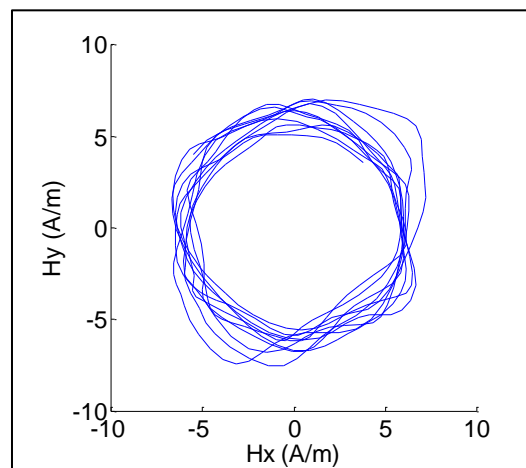


Figure 5.16 The Magnetic Field Polarization Changes from Linear to Circular

A Gaussian source was applied to find the broadband frequency response during gyromagnetic resonance. The temporal and spatial resolution was  $\Delta t = 66 \text{ ps}$  and  $\Delta x = 200 \mu\text{m}$ . The MEEP Code is given in Appendix A.

The ferrite boundaries were terminated with perfectly matched layers to absorb all the incident electromagnetic fields and to prevent unwanted reflections or disturbances to electron spins of saturated magnetic dipoles.

The Linearly polarized Gaussian pulse had a bandwidth of 60 GHz centered at 30 GHz as shown in Figure 5.17.

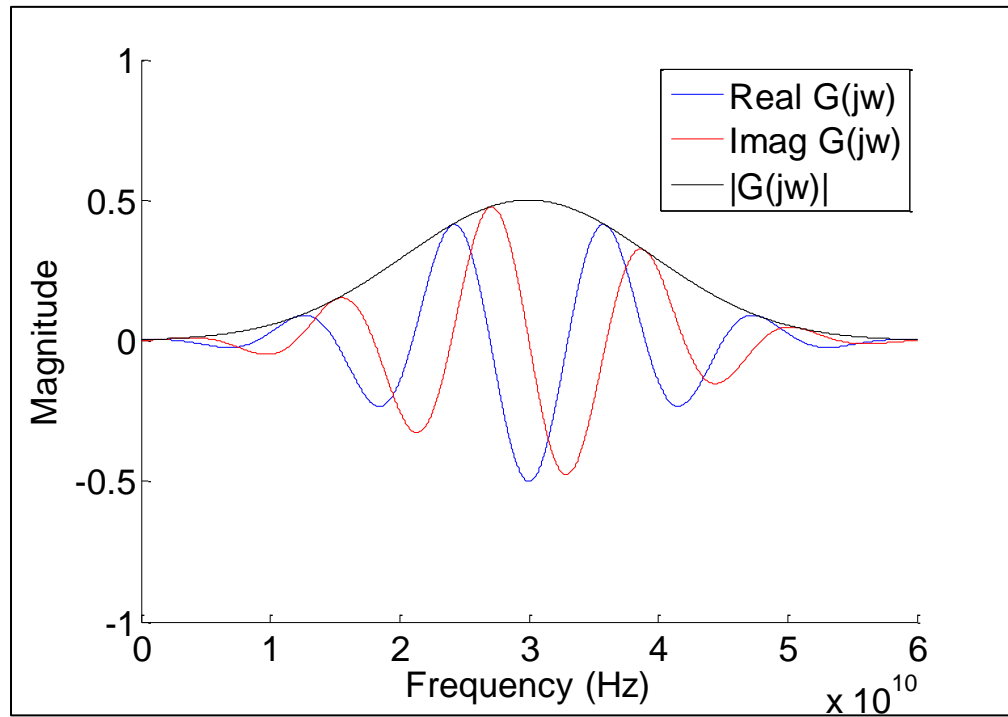


Figure 5.17 Fourier Transform of Gaussian Pulse

The various frequencies faced different degrees of rotation per unit of propagation distance. The Gaussian pulse was heavily distorted as it moved along the direction of propagation. Various frequencies rotated around the bias vector at different rates (rotation angle per unit propagation distance). Hence, the Gaussian pulse was heavily deformed as it reached the output end. The polarization of each frequency was changed from linear polarization as it moved in the direction of propagation. The resultant polarization was a linear sum of all the polarizations of the various frequencies.

The Polarization of the linearly Polarized wave changed as it moves across the saturated ferrite. The strongest resonance was due to the 30 GHz harmonic as shown in Figure 5.18 and Figure 5.19.

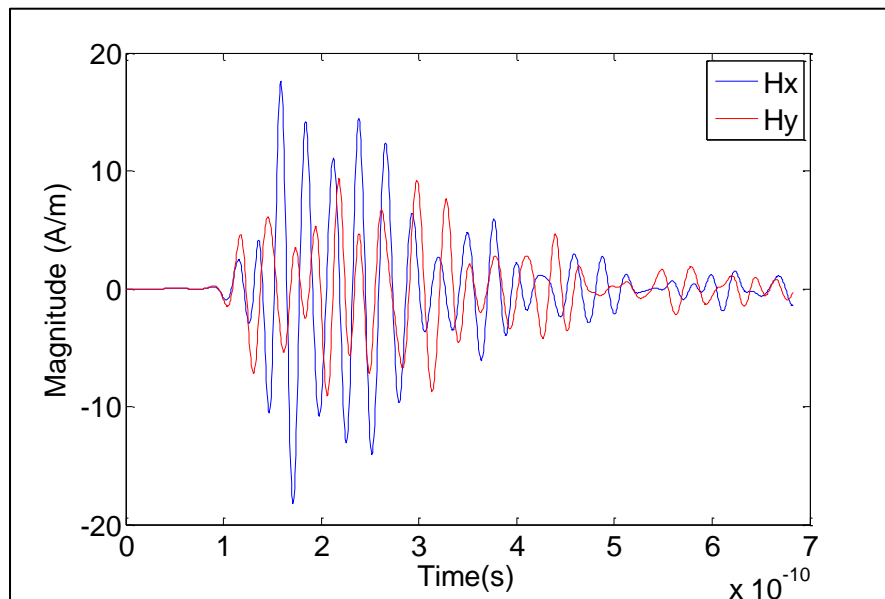


Figure 5.18 Gyromagnetic Resonance at Larmor Frequency of 30 GHz



As seen in Figure 5.19, the resultant polarization changed continuously as the various frequency components experienced different rates of rotation per unit distance of propagation.

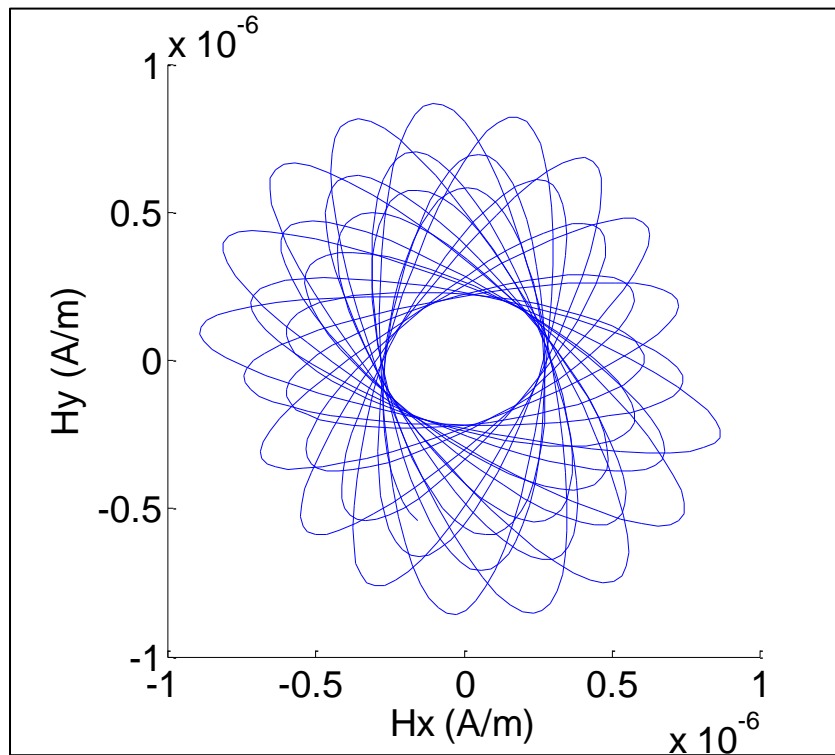


Figure 5.19 Gyromagnetic Precession Due to Gaussian Source

The 30 GHz harmonic of the incident Gaussian wave matched the Larmor frequency and gave rise to gyromagnetic resonance. The wave impedance shown in Figure 5.20 was calculated using the Fourier transform of a small window of input and output signals, during steady state of gyromagnetic resonance. The intrinsic wave impedance

spikes due to the high magnetic susceptibility and magnetic permeability during the 30 GHz gyromagnetic resonance. The huge value of intrinsic wave impedance increases the electromagnetic power losses across the saturated ferrite. It absorbs a lot of electromagnetic energy from the transverse field and starts to heat up. The intrinsic wave impedance dropped when the Gilbert damping constant was increased.

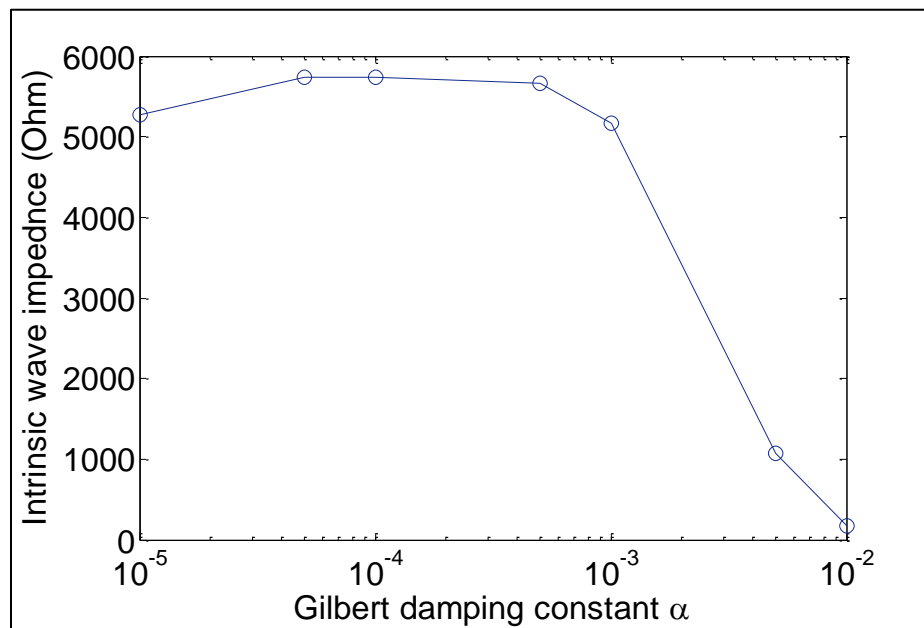


Figure 5.20 Plot of Intrinsic Wave Impedance vs Gilbert Damping Constant.

The phase constant and attenuation constant were calculated for the resultant magnetic spin wave. The calculated wave attenuation constant is shown in Figure 5.21, which was calculated by comparing the magnetic field strength at input and output sides. The output signal was heavily attenuated compared to the input signal hence the attenuation

constant was very high during the 30 GHz gyromagnetic resonance. A high quality crystal oscillator, with a small Gilbert damping constant, showed a strong peak of the electromagnetic absorption spectrum. When the Gilbert damping constant was increased, the attenuation constant and the electromagnetic absorption decreased.

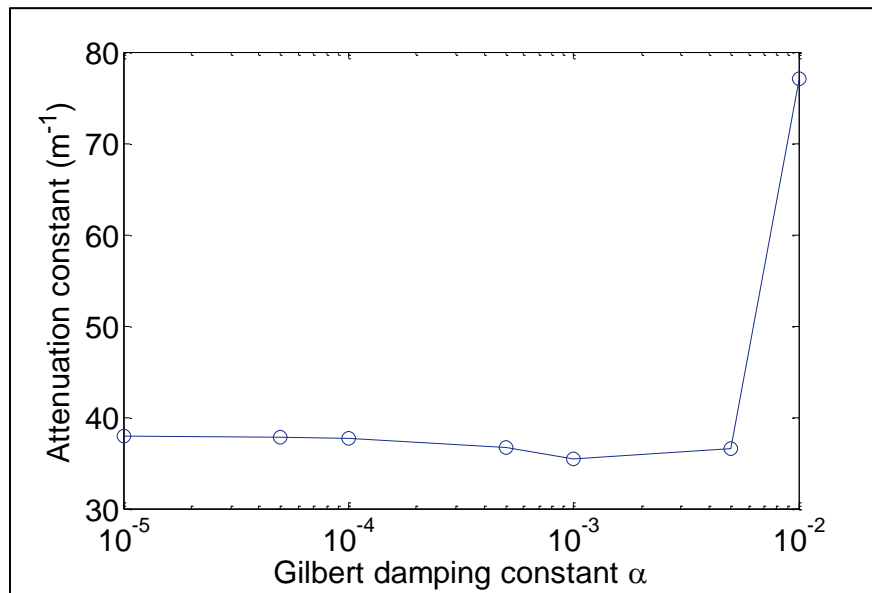


Figure 5.21 Plot of Wave Attenuation Constant vs Gilbert Damping Constant

The calculated per unit length longitudinal admittance during gyromagnetic resonance is shown in Figure 5.22. Ferromagnetic resonance leads to a severe increase in power dissipation in the ferrite sample which makes the saturated ferrite sample highly conductive to electromagnetic flux. The saturated ferrite sample absorbs a lot of electromagnetic energy and starts to heat up. The complex permittivity and magnetic permeability dictate the dielectric and magnetic losses of the resonating sample. When the

Gilbert damping constant was increased, the longitudinal magnetic admittance increased as well.

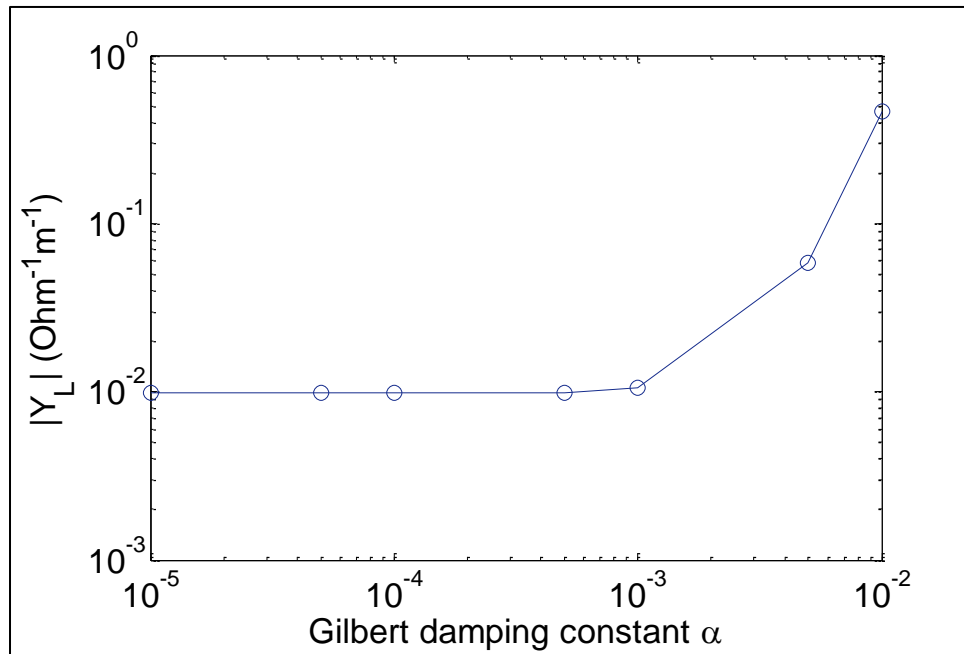


Figure 5.22 Plot of Longitudinal Magnetic Admittance vs Gilbert Damping Constant

The calculated per unit length transverse magnetic impedance during gyromagnetic resonance is shown in Figure 5.23. The 30 GHz gyromagnetic resonance leads to a severe increase in power dissipation in the ferrite sample. The magnetic flux leakage drops heavily and this makes the saturated ferrite sample highly conductive to electromagnetic flux. Ultimately, the saturated ferrite sample absorbs a lot of electromagnetic energy. When the

Gilbert damping constant was increased, the transverse magnetic impedance dropped.

This indicated an increase in the magnetic flux leakage across the magnetized ferrite.

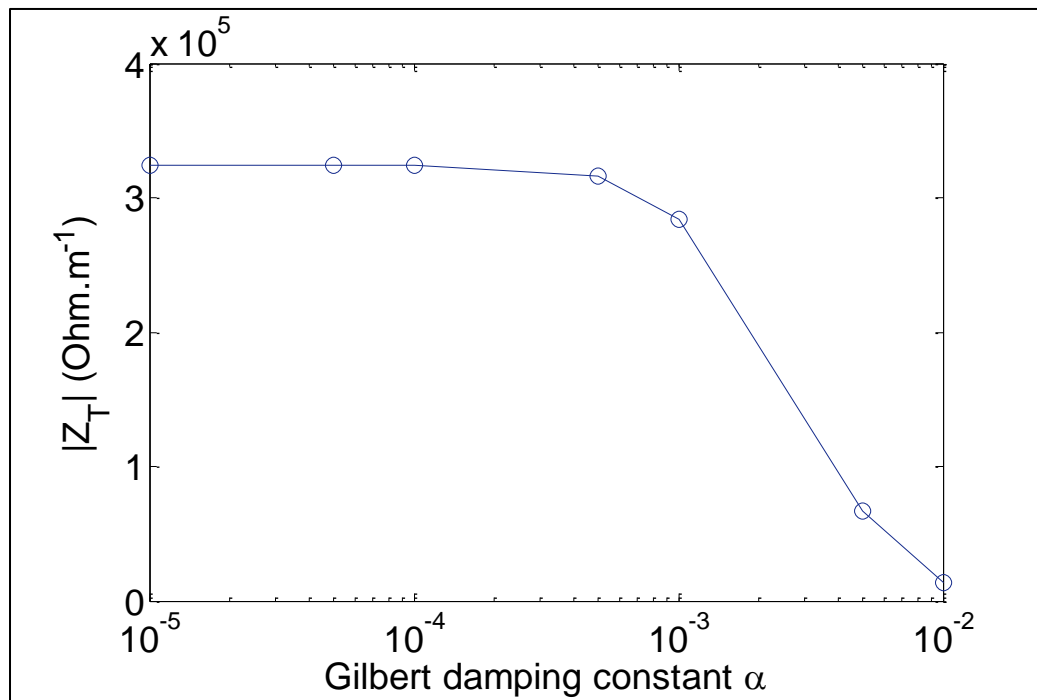


Figure 5.23 Plot of Transverse Magnetic Impedance vs Gilbert Damping Constant.

This chapter presented MEEP simulations of dispersive MnZn ferrite. The magnetic transmission line model was used to derive a system level representation for the complex magnetic circuit. The simulation results were tested against theory results for the frequency range of 1 MHz – 1 GHz.

Next, saturated gyromagnetic ferrite was simulated using the linearized Landau-Lifshitz-Gilbert model in MEEP. The MEEP code and MATLAB code is given in Appendix A and Appendix B. The magnetic transmission line model was adopted to simplify the precession of saturated magnetic dipoles in response to a wideband Gaussian pulse. The sample resonated at 30 GHz when its longitudinal admittance dropped and transverse impedance spiked. This made it highly conductive to electromagnetic flux and caused it to absorb a lot of energy from the input source.

During ferromagnetic resonance, the longitudinal magnetic admittance of the saturated ferrite dropped hence it provided a low reluctance path for magnetic flux. The magnetic flux leakage was small because the transverse magnetic impedance dropped. The nano-magnets exhibited a strong absorption of millimeter wave which resulted in a high attenuation constant.

The Gilbert damping constant was varied to simulate the effect of magnetic hardness on the ferromagnetic resonance. Gilbert damping constant depends on the crystal structure, chemical composition, ferrite grain size, structural dimensions and annealing temperature. A high quality crystal oscillator must have a very low Gilbert damping constant, so that it can absorb millimeter waves and excite spin waves efficiently [51], [34], [50], [49].

The intrinsic wave impedance and attenuation constant were a strong function of effective magnetic susceptibility. They explain the high electromagnetic power losses across the saturated ferrite when it absorbs electromagnetic energy from the input signal. When the Gilbert damping constant was increased from  $10^{-5}$  to  $10^{-3}$ , the damping for precessional motion was increased, and the excitation of spin wave modes was restrained. The low magnetic susceptibility caused the intrinsic wave impedance and attenuation constant to drop. Hence, the electromagnetic absorption of millimeter waves by nanomagnets reduced significantly. When the effective magnetic susceptibility decreased, the magnetic reluctance increased and the absorption of magnetic flux dropped. This resulted in a huge increase in the longitudinal magnetic admittance. Meanwhile, the magnetic flux leakage increased which resulted in the drop of transverse magnetic impedance. The results were affirmed by calculating the longitudinal magnetic admittance and transverse magnetic impedance for each case. The simulation results are consistent with the experimental observations [51], [34], [50], [49].

## 6. CONCLUSION

This research presented three different circuit models for ferromagnetic elements. The age-old reluctance model based on the ohm's law analogy was found to violate power invariance property. An application of modeling a DC compounded generator was presented as well and the was only suitable for steady state simulations of magnetic cores with known reluctance profile.

The permeance-capacitance model uses a nonlinear permeance to model nonlinearity and hysteresis losses of magnetic materials. It is valuable for simulating transient behavior of ferromagnetic elements like RF inductors, transformers and filters. A full bridge isolated buck converter was designed to study its response. The model can be improved as it does not feature an electric energy storage element or an energy dissipation element.

The third model was the magnetic transmission line model which is the most accurate model for modeling dispersive, inhomogeneous and lossy magnetic cores. It uses transmission line theory to predict magnetic parameters of ferromagnetic core. The MEEP simulation results for a MnZn ferrite were presented to verify magnetic transmission line theory. The model was very useful in predicting the frequency response up to 1 GHz. The model was also used to study ferromagnetic resonance of a saturated ferromagnet. The electrodynamic behavior of saturated magnetic dipoles was simulated using linearized Landau-Lifshitz-Gilbert model. It was deduced that ferromagnetic resonance leads to an increase in transverse magnetic impedance and a drop in longitudinal magnetic admittance.



This effect is much more pronounced in a high quality crystal with a low Gilbert damping constant.

The power invariant magnetic transmission line model [4], [5], [6], [7], [8] can also be used for accurate modeling of ferrite loaded micro-strip patch antennas, gyromagnetic NLTLs, magnetic transistors and spintronic devices [51], [34], [50], [49]. The MEEP simulator could not model magnetostriction, acoustic effects and relativistic effects.

Throughout this research, non-linear components were used for simulating complex effects such as DC resistance losses, skin effect losses, proximity effect losses, self-capacitance dielectric losses, self-capacitance circulating currents losses, core residual losses, core eddy current losses and core hysteresis losses [45]. Network equivalent magnetic circuits [54] and coupled equations were used to simplify analysis of the transient [41] and steady state behavior.

The magnetic coupling between magnetic transmission lines [4], [5], [6], [7], [8] results in sharing of electromagnetic energy. This division of power is very useful in design of DC and AC machines, DC converters and high frequency wideband transformers. The study of capacitive and inductive coupling in multi-conductor transmission lines provides useful knowledge about the radiated/ conducted emissions and radiated/ conducted susceptibility. Due to the versatility of the magnetic transmission line model, different transmission line structures can be simulated like shielded transmission line and multi-wire transmission lines.

## BIBLIOGRAPHY

- [1] "IEEE guide for loss evaluation of distribution and power transformers and reactors", IEEE Standard C57.120-2017 (Revision of IEEE Standard C57.120-1991), pp. 1-53, 2017.
- [2] "IEEE standard for pulse transformers", ANSI/IEEE Standard 390-1987, pp. 1-32, 1987.
- [3] R. Erickson, D. Maksimovic, *Fundamentals of Power Electronics*, 2nd Edition. Kluwer, pp. 565-584, 2004.
- [4] J. Faria, "Multimodal propagation in multiconductor transmission lines", *Journal of Electromagnetic Waves Applications*, pp. 1677-1702, 2014.
- [5] J. Faria, "Formulation of multiwire magnetic transmission-line theory", *Progress in Electromagnetics Research B*, Vol. 49, pp. 177-195, 2013.
- [6] J. Faria, "Matrix theory of wave propagation in hybrid electric/magnetic multiwire transmission line systems", *Journal of Electromagnetic Waves and Applications*, Vol. 29, No. 7, pp. 925-940, 2015.
- [7] J. Faria, "A physical model of the ideal transformer based on magnetic transmission line theory", *Journal of Electromagnetic Waves and Applications*, Vol. 27, No. 3, pp. 365-373, 2013.
- [8] J. Faria, *Electromagnetic Foundations of Electrical Engineering*, Chichester: John Wiley and Sons, pp. 335-375, 2008.
- [9] R. Slatter, "High accuracy, high bandwidth magnetoresistive current sensors for spacecraft power electronics", *2015 17th European Conference on Power Electronics and Applications (EPE15 ECCE-Europe)*, pp. 1-10, 2015.
- [10] D. Zyatkov, V. Balashov, V. Yurchenko, V. Cherepanov and Z. Kochnev, "Capacitive sensing element with a magnetic fluid for detecting of change of magnetic field", 2019

- Photonics & Electromagnetics Research Symposium - Spring (PIERS-Spring)*, pp. 1507-1510, 2019.
- [11] H. Zhao, Y. Li, Q. Lin and S. Wang, “The parasitic capacitance of magnetic components with ferrite cores due to time-varying electromagnetic (EM) field”, *2018 IEEE Energy Conversion Congress and Exposition (ECCE)*, pp. 3534-3541, 2018.
- [12] A. Khitun and A. Kozhanov, “Magnonic logic devices”, *Nanomagnetic and Spintronic Devices for Energy-Efficient Memory and Computing*, pp. 189–219, 2016.
- [13] K. Sato, E. Saitoh A. Willoughby and P. Capper, *Spintronics for next generation Innovative Devices*. John Wiley and Sons, pp. 1-76, 2015.
- [14] M. Leuenberger and D. Loss, “Quantum computing in molecular magnets”, *Nature*, Vol. 410, No. 6830, pp. 789–793, 2001.
- [15] M. Imtaar, P. Li, E. Varga, G. Csaba, G. Bernstein, G. Scarpa, W. Porod and P. Lugli, “Nanomagnetic logic devices fabrication using nanoimprint lithography”, *2013 13th IEEE International Conference on Nanotechnology (IEEE-NANO 2013)*, pp. 578-581, 2013.
- [16] M. Holynska, *Single-Molecule Magnets: Molecular Architectures and Building Blocks for Spintronics*. Newark: John Wiley and Sons, pp. 87-131, 2019.
- [17] J. Atulasimha and S. Bandyopadhyay, *Nanomagnetic and Spintronic Devices for energy-efficient memory and computing*. Chichester, West Sussex: Wiley, pp. 65-253, 2016.
- [18] S. Demokritov, *Magnonics: From Fundamentals to Applications*. Berlin: Springer, pp. 130-153, 2013.
- [19] I. Eichwald, S. Breitkreutz, G. Ziemys, G. Csaba, W. Porod and M. Becherer, “Majority logic gate for 3D magnetic computing”, *Nanotechnology*, Vol. 25, No. 33, 335202, pp. 1-8, 2014.
- [20] A. Guimaraes, *Principles of Nanomagnetism*. Cham: Springer, pp. 1-246, 2018.

- [21] P. Ripka and M. Janosek, "Advances in magnetic sensors", *2008 IEEE Sensors*, pp. 1108-1116, 2008.
- [22] G. Cividjian, "Corner 2D Capacitance", *2018 20th International Symposium on Electrical Apparatus and Technologies (SIELA)*, pp. 1-5, 2018.
- [23] M. Nitu, M. Nicola, M. Duta and M. Benea, "Methods for determining dielectric stresses in the windings of a transformer subjected to lightning impulse", *2019 International Conference on Electromechanical and Energy Systems (SIELMEN)*, pp. 1-3, 2019.
- [24] C. Paul, K. Whites and S. Nasar, *Introduction to electromagnetic fields*, 4th Edition, Boston: WCB/McGraw-Hill, pp.586-589, 1998.
- [25] S. Blundell, *Magnetism in condensed matter*. Oxford: Oxford University Press, pp. 50-80, 2014.
- [26] U. Ozgur, Y. Alivov and H. Morkoc, "Microwave ferrites, Part 2: Passive components and electrical tuning", *ChemInform*, Vol. 41, No. 36, pp. 1-153, 2010.
- [27] A. Goldman, *Modern Ferrite Technology*, New York, NY: Springer, pp. 1-226, 2010.
- [28] D. Dinulovic, M. Shousha, M. Haug and K. Shafey, "Miniaturized planar transformer embedded in ferrite substrate for isolated high-frequency low-power applications", *2019 20th International Symposium on Power Electronics*, pp. 1-5, 2019.
- [29] D. Pozar, *Microwave Engineering*, 4th Edition, Kentucky: John Wiley and Sons, pp. 1-271, 2012.
- [30] M. Luo, D. Dujic and J. Allmeling, "Modelling hysteresis of soft core materials using permeance-capacitance analogy for transient circuit simulations", *2017 19th European Conference on Power Electronics and Applications (EPE17 ECCE Europe)*, pp. 1-10, 2017.

- [31] M. Luo, D. Dujic and J. Allmeling, “Modeling frequency independent hysteresis effects of ferrite core materials using permeance–capacitance analogy for system-level circuit simulations”, *IEEE Transactions on Power Electronics*, Vol. 33, No. 12, pp. 1-15, 2018.
- [32] M. Luo, D. Dujic and J. Allmeling, “Permeance based modeling of magnetic hysteresis with inclusion of eddy current effect”, *2018 IEEE Applied Power Electronics Conference and Exposition (APEC)*, pp. 1764-1771, 2018.
- [33] J. Macías-Díaz, “Persistence of nonlinear hysteresis in fractional models of Josephson transmission lines”, *Communications in Nonlinear Science and Numerical Simulation*, Vol. 53, pp. 31–43, 2017.
- [34] J. Rossi, F. Yamasaki, E. Schamiloglu and J. Barroso, “Analysis of nonlinear gyromagnetic line operation using LLG equation”, *2017 IEEE 21st International Conference on Pulsed Power (PPC)*, pp. 1-3, 2017.
- [35] J. Xu, M. Koledintseva, Y. Zhang, Y. He, B. Matlin, R. Dubroff, J. Drewniak and J. Zhang, “Complex permittivity and permeability measurements and finite-difference time-domain simulation of ferrite materials”, *IEEE Transactions on Electromagnetic Compatibility*, Vol. 52, No. 4, pp. 878-887, 2010.
- [36] N. Tiwari, A. Jha, S. Singh and M. Akhtar, “Estimation of broadband complex permeability using SIW cavity based multimodal approach”, *IEEE Transactions on Instrumentation and Measurement*, pp. 1-11, 2020.
- [37] S. Chua, Y. Chong, A. Stone, M. Soljacic and J. Bravo-Abad, “Low-threshold lasing action in photonic crystal slabs enabled by fano resonances”, *Optics Express*, Vol. 19, No. 2, pp. 1539-1562, 2011.
- [38] T. Deng and Z. Chen, “Design of frequency-dispersive magnetic material for application of microwave attenuation”, *2016 46th European Microwave Conference (EuMC)*, pp. 588-591, 2016.
- [39] G. Nnachi, A. Akumu, C. Richards and D. Nicolae, “Estimation of no-load losses in distribution transformer design”, *2018 IEEE PES/IAS PowerAfrica*, pp. 527-532, 2018.

- [40] C. Paul, *Analysis of Multiconductor Transmission Lines*, 2nd Edition, Hoboken: Wiley-Interscience, pp. 240-342, 2008.
- [41] M. Brignone, D. Mestriner, R. Procopio, A. Piantini and F. Rachidi, "On the stability of FDTD-based numerical codes to evaluate lightning-induced overvoltages in overhead transmission lines", *IEEE Transactions on Electromagnetic Compatibility*, Vol. 62, No. 1, pp. 108–115, 2020.
- [42] C. Caloz and T. Itoh, *Electromagnetic Metamaterials: Transmission Line Theory and Microwave Applications*, Wiley-IEEE Press, pp. 27-58, 2006.
- [43] G. Antonini, "A general framework for the analysis of metamaterial transmission lines", *Progress in Electromagnetics Research B*, pp. 353–373, 2010.
- [44] S. Chapman, *Electric machinery fundamentals*. New York: McGraw-Hill, pp. 464-564, 2012.
- [45] S. Karelin, "FDTD analysis of nonlinear magnetized ferrites: application to modeling of oscillation forming in coaxial line with ferrite", *Radiofizika I Elektronika*, Vol. 22, No. 1, pp. 51–56, 2017.
- [46] J. Bragg, J. Dickens and A. Neuber, "Material selection considerations for coaxial, ferrimagnetic-based nonlinear transmission lines", *Journal of Applied Physics*, Vol. 113, No. 6, 064904, pp. 1-4, 2013.
- [47] V. Harris, "Modern microwave ferrites", *IEEE Transactions on Magnetics*, Vol. 48, No. 3, pp. 1075–1104, 2012.
- [48] A. Moryc and W. Gwarek, "An equivalent lumped circuit describing magnetized plasma and its application in FD-TD modeling", *15th International Conference on Microwaves, Radar and Wireless Communications*, pp. 75-78, 2004.
- [49] J. Parson, A. Neuber, J. Dickens and J. Mankowski, "Investigation of a stripline transmission line structure for gyromagnetic nonlinear transmission line high power microwave sources", *Review of Scientific Instruments*, Vol. 87, pp. 1-7, 2016.

- [50] I. Romanchenko, P. Priputnev and V. Rostov, “RF pulse formation dynamics in gyromagnetic nonlinear transmission lines”, *Journal of Physics: Conference Series*, Vol. 830, No. 1, 012034, pp. 1-4, 2017.
- [51] M. Ulmasculov, K. Sharypov, S. Shunailov, V. Shpak, M. Yalandin, M. Pedos and S. Rukin, “Gyromagnetic nonlinear transmission line generator of high voltage pulses modulated at 4 GHz frequency with 1000 Hz pulse repetition rate”, *Journal of Physics: Conference Series*, Vol. 830, 012027, pp. 1-6, 2017.
- [52] C. Paul, *Introduction to Electromagnetic Compatibility*, 2nd Edition, Kentucky: John Wiley and Sons, pp. 559-710, 2006.
- [53] W. Sui, *Time Domain Computer Analysis of Nonlinear Hybrid Systems*, pp. 251-283, 2018.
- [54] T. Edwards and M. Steer, *Foundations for Microstrip Circuit Design*, 4th Edition, Wiley-IEEE Press, pp. 576-607, 2016.
- [55] L. Er-Ping, “Computational electromagnetics for electromagnetic compatibility/signal integrity analysis”, IEEE EMC DL Talk, University of Missouri, pp. 1-64, 2008.
- [56] R. Darraji, M. Honari, R. Mirzavand, F. Ghannouchi and P. Mousavi, “Wideband two-section impedance transformer with flat real-to-real impedance matching”, *IEEE Microwave and Wireless Components Letters*, Vol. 26, No. 5, pp. 313–315, 2016s.
- [57] J. Schneider, *Understanding the Finite-Difference Time-Domain Method*, pp. 33-74, 2017.
- [58] Y. Li, X. Li and J. Mao, “Time domain analysis of transmission line based on WLP-FDTD”, *2013 IEEE International Wireless Symposium (IWS)*, pp. 1-4, 2013.
- [59] D. Hamill, “Gyrator-capacitor modeling: a better way of understanding magnetic components”, *Proceedings of 1994 IEEE Applied Power Electronics Conference and Exposition - ASPEC94*, Vol. 1, pp. 326-332, 1994.

- [60] J. Allmeling, W. Hammer and J. Schonberger, “Transient simulation of magnetic circuits using the permeance-capacitance analogy”, *2012 IEEE 13th Workshop on Control and Modeling for Power Electronics (COMPEL)*, pp. 1-4, 2012.
- [61] B. Anderson and R. Newcomb, “A capacitor-transformer gyrator realization”, *Proceedings of the IEEE*, Vol. 53, No. 10, pp. 1640, 1965.
- [62] A. Taflove and S. Hagness, *Computational Electrodynamics: The Finite-Difference Time-Domain Method*, 3rd Edition, Boston: Artech House, pp. 145-278, 2005.
- [63] A. Taflove, A. Oskooi and S. Hagness, *Advances in FDTD computational electrodynamics: photonics and nanotechnology*, 3rd Edition, Boston: Artech House, pp. 567-592, 2013.
- [64] A. Oskooi, D. Roundy, M. Ibanescu, P. Bermel, J. Joannopoulos and S. Johnson, “MEEP: A flexible free-software package for electromagnetic simulations by the FDTD method”, *Computer Physics Communications*, Vol. 181, pp. 687-702, 2010.
- [65] G. González and M. Ehsani, “Power-invariant magnetic system modeling”, *International Journal of Magnetics and Electromagnetism*, Vol. 4, No. 1, pp. 1–9, 2018.
- [66] I. Boldea and S. Nasar, *Linear electric actuators and generators*. Cambridge: Cambridge University Press, pp. 150-220, 1997.
- [67] H. Al-Barqawi, N. Dib and M. Khodier, “A full-wave two-dimensional finite-difference frequency-domain analysis of ferrite-loaded structures”, *Mosharaka International Conference on Communications, Propagation and Electronics*, pp. 1-6, 2008.
- [68] J. Lehr, P. Ron, *Foundations of Pulsed Power Technology*: John Wiley and Sons, pp. 63–96, 2017.
- [69] N. Shirdel, A. Akbari, H. Mirzaei and M. Abrishamian, “Three-dimensional simulation of UHF signal propagation in transformer using FDTD method”, *2011 International Conference on Power Engineering, Energy and Electrical Drives*, pp. 1-6, 2011.



- [70] E. Snelling, *Soft Ferrites: Properties and Applications*. Mendham, NJ: PSMA, pp. 1-358, 2005.
- [71] B. Gustavsen, "A hybrid measurement approach for wide-band characterization and modeling of power transformers", *2011 IEEE Power and Energy Society General Meeting*, pp. 1, 2011.
- [72] F. Grecki and B. Wunsch, "Validation of power transformer wideband modeling using standard sFRA method with VNA equipment", *2019 IEEE PES Asia-Pacific Power and Energy Engineering Conference (APPEEC)*, pp. 311-329, 2019.
- [73] R. Mack and J. Sevick, *Sevick's Transmission Line Transformers: Theory and practice*, 5th Edition, Edison, NJ: Scitech Publishing, pp. 1-25, 2014.
- [74] "IEEE Recommended Practice for Validation of Computational Electromagnetics Computer Modeling and Simulations", IEEE Standard 1597.2-2010, pp.1-124, 2011.

## APPENDICES

### APPENDIX A. MEEP CODE

```

#include <iostream>
#include <fstream>
#include <stdio.h>
#include <stdlib.h>
#include <string.h>
#include <complex>
#include "meep.hpp"
#include "ctl-math.h"
#include "ctlgeom.h"
#include "meepgeom.hpp"
#include <math.h>
#ifdef DATADIR
#define DATADIR "./"
#endif

using namespace meep;
using namespace std;
typedef std::complex<double> cdouble;

double epsr=1;
//SI Conversion Factors
double a0=1e-2;//0.1mm
double c0=2.99792458e8;//Speed of Light (m/s)
double f0=c0/a0;//300GHz
double t0=1/f0;//0.33e-12 (s)
double mu0=4*pi*(1e-7);// (H/m)
double eps0=8.854187817e-12;// (F/m)
double I0=1; //(A)
double E0=I0/(a0*eps0*c0);//Electric Field
double D0=I0/(a0*c0);//Electric Displacement Field
double B0=I0/(a0*eps0*c0*c0);//Magnetic Field
double H0=I0/(a0);//Magnetizing Field
double sigmaD0=(epsr*eps0*c0)/a0;//Electric Conductivity
double J0=I0/(a0*a0);//Electric Current Density
double u0=(I0*I0)/(eps0*c0*c0*a0*a0);//Energy Density
double S0=(I0*I0)/(eps0*c0*a0*a0);//Poynting Vector
double Sc0=1/(c0);//Courant Factor
double sig0=1e4;
double b0=0.0;

double xcen=0.0, ycen=0.0, zcen=0.0;
double dxmin=0.0, dxmax=02.5, dymin=0.0, dymax=02.5, dzmin=0.0,
dzmax=15.0;
double wcore=2.0*dymax;
double winding_thickness_p=01.0,
insulation_thickness_p=02.5,pml_thickness=1.0;

```

```

double mu_core=1.0;
int Np=1;//must be odd
int Ns=1;//must be odd
double margin=0.2;
double amplitude=1.0;
double divisions=2;
int numcoord=0;
int corecoord=0;
double k=2*pi*Np/(2*dzmin);
double theta=0.0;
double rp=(wcore/2.0)+(winding_thickness_p/2.0)+insulation_thickness_p;
double * xpcoord=new double [1000];
double * ypcoord=new double [1000];
double * zpcoord=new double [1000];
double * xscoord=new double [1000];
double * yscoord=new double [1000];
double * zscoord=new double [1000];
double * xccoord=new double [1000];
double * yccoord=new double [1000];
double * zccoord=new double [1000];

```

```

cdouble line_integral_x(fields & f, component C, double dx, double
xmin, double xmax, double y, double z)

```

```

{
    cdouble sum(0.0,0.0);
    cdouble deltax(dx,0.0);
    for (double x=xmin; x<=xmax; x=x+dx)
    {
        monitor_point p;
        f.get_point(&p, vec(x,y,z));
        cdouble dF = p.get_component(C);
        sum += dF*deltax;
    }
    return sum;
}

```

```

cdouble line_integral_y(fields & f, component C, double dy, double
ymin, double ymax, double x, double z)

```

```

{
    cdouble sum(0.0,0.0);
    cdouble deltax(dy,0.0);
    for (double y=ymin; y<=ymax; y=y+dy)
    {
        monitor_point p;
        f.get_point(&p, vec(x,y,z));
        cdouble dF = p.get_component(C);
        sum += dF*deltax;
    }
    return sum;
}

```

```

cdouble line_integral_z(fields & f, component C, double dz, double
zmin, double zmax, double x, double y)

```

```

{
    cdouble sum(0.0,0.0);

```

```

cdouble deltaz(dz,0.0);
for (double z=zmin; z<=zmax; z=z+dz)
{
    monitor_point p;
    f.get_point(&p, vec(x,y,z));
    cdouble dF = p.get_component(C);
    sum += dF*deltaz;
}
return sum;
}

cdouble compute_Im(fields & f, double z)
{
    cdouble Iyf=line_integral_y(f,Ey,0.01,ycen-
dymax,ycen+dymax,xcen+dxmax,z);
    cdouble Iyb=line_integral_y(f,Ey,0.01,ycen-dymax,ycen+dymax,xcen-
dxmax,z);
    cdouble Ixt=line_integral_x(f,Ex,0.01,xcen-dxmax,xcen+dxmax,ycen-
dymax,z);
    cdouble Ixb=line_integral_x(f,Ex,0.01,xcen-
dxmax,xcen+dxmax,ycen+dymax,z);
    cdouble Im=Ixt+Iyf-Ixb-Iyb;
    return Im;
}

cdouble compute_Ie(fields & f, double z)
{
    cdouble Iyf=line_integral_y(f,Hy,0.01,ycen-
dymax,ycen+dymax,xcen+dxmax,z);
    cdouble Iyb=line_integral_y(f,Hy,0.01,ycen-dymax,ycen+dymax,xcen-
dxmax,z);
    cdouble Ixt=line_integral_x(f,Hx,0.01,xcen-dxmax,xcen+dxmax,ycen-
dymax,z);
    cdouble Ixb=line_integral_x(f,Hx,0.01,xcen-
dxmax,xcen+dxmax,ycen+dymax,z);
    cdouble Ie=Ixt+Iyf-Ixb-Iyb;
    return Ie;
}

cdouble compute_Vm(fields & f, double z)
{
    cdouble Vz=line_integral_y(f,Hy,0.01,-25.0,0.0,xcen,z);
    return Vz;
}

cdouble compute_Ve(fields & f, double z)
{
    cdouble Vz=line_integral_y(f,Ey,0.01,-25.0,0.0,xcen,z);
    return Vz;
}

double mu(const vec &v)
{
    return 1.0;
}

```

```

double eps(const vec &v)
{
    return 1.0;
}

double conductivity(const vec &v)
{
}

double sigma(const vec &v)
{
    bool in_middle=false;

    for (int i=0; i<corecoord; i++)
    {
        double dxp=v.x() - xccoord[i];
        double dyp=v.y() - yccoord[i];
        double dzp=v.z() - zccoord[i];
        if ((dxp<=(wcore/2.0)) && (dyp<=(wcore/2.0)) && (dzp<=(wcore/2.0))) {
            in_middle=true;
        }
        double sigp=0.0;
        if(in_middle){sigp=sig0;}
        else{sigp=0.0;}
        return sigp;
    }
}

class core_material : public material_function {
public:
};

class winding_material : public material_function {
public:
};

typedef struct my_material_func_data {
    double rxInner, ryInner, rOuter;
    bool with_susceptibility;
} my_material_func_data;

void my_material_func(vector3 p, void *user_data,
meep_geom::medium_struct *m)
{
    my_material_func_data *data = (my_material_func_data *)user_data;
    bool in_middle=false;
    double dx=p.x - xcen;
    double dy=p.y - ycen;
    double dz=p.z - zcen;

    for (int i=0; i<corecoord; i++) {
        double dxp=p.x - xccoord[i];
        double dyp=p.y - yccoord[i];
        double dzp=p.z - zccoord[i];
    }
}

```

```

        if ((dyp<=(wcore/2.0)) && (dyp<=(wcore/2.0)) && (dzp<=(wcore/2.0)))
        {
            in_middle=true;}
    }

    // set permittivity and permeability
    double nn = in_middle ? sqrt(mu_core) : 1.0;
    double mm = in_middle ? sqrt(1.0) : 1.0;
    m->epsilon_diag.x = m->epsilon_diag.y = m->epsilon_diag.z = 10.0;
    m->mu_diag.x = m->mu_diag.y = m->mu_diag.z = nn*nn;
    m->E_chi2_diag.x = m->E_chi2_diag.y = m->E_chi2_diag.z = 0.0;
    m->E_chi3_diag.x = m->E_chi3_diag.y = m->E_chi3_diag.z = 0.0;
    m->H_chi2_diag.x = m->H_chi2_diag.y = m->H_chi2_diag.z = 1.0;
    m->H_chi3_diag.x = m->H_chi3_diag.y = m->H_chi3_diag.z = 1.0;

    if (in_middle)
    {
        m->D_conductivity_diag.x = m->D_conductivity_diag.y = m-
>D_conductivity_diag.z = (5e-3)/sigmaD0;
    }

    for (int i=0; i<numcoord; i++)
    {
        double dyp=p.y - ypcoord[i];
        double dyp=p.y - ypcoord[i];
        double dzp=p.z - zpcoord[i];
        double drp=sqrt(dxp*dxp+dyp*dyp+dzp*dzp);
        if ((dyp<=(winding_thickness_p/2.0)) && (dyp<=(winding_thickness_p/2.0)) &&
(dzp<=(winding_thickness_p/2.0)))
        {
            //m->D_conductivity_diag.x = m->D_conductivity_diag.y = m-
>D_conductivity_diag.z = (3.5e7)/sigmaD0;
        }
        double dxs=p.x - xscoord[i];
        double dys=p.y - yscoord[i];
        double dzs=p.z - zscoord[i];
        double drs=sqrt(dxs*dxs+dys*dys+dzs*dzs);

        if ((dxs<=(winding_thickness_p/2.0)) && (dys<=(winding_thickness_p/2.0)) &&
(dzs<=(winding_thickness_p/2.0))) {
            //m->D_conductivity_diag.x = m->D_conductivity_diag.y = m-
>D_conductivity_diag.z = (3.5e7)/sigmaD0;
        }
    }
}

class anisodisp_materialH : public material_function {
public:
    virtual void sigma_row(component c, double sigrow[3], const vec &r) {
        (void)r; // unused
        if (component_direction(c) == X) {
            sigrow[0] = sig0;
            sigrow[1] = sig0;
            sigrow[2] = sig0;
        }
    }
}

```

```

    else if (component_direction(c) == Y) {
        sigrow[0] = sig0;
        sigrow[1] = sig0;
        sigrow[2] = sig0;
    }
    else {
        sigrow[0] = sig0;
        sigrow[1] = sig0;
        sigrow[2] = sig0;
    }
}
};

```

```

int main(int argc, char *argv[]) {

    initialize mpi(argc,argv);
    const char *mydirname = "MMTL-out";
    std::ofstream Time;
    std::ofstream Space;
    std::ofstream FieldsIn;
    std::ofstream FieldsOut;
    std::ofstream Fluxes;
    std::ofstream Skin;
    std::ofstream Permeability;
    std::ofstream Permittivity;
    std::ofstream Chilinv;
    std::ofstream SourceFFT;

    Time.open ("TimeEvolution.txt");
    Space.open ("SpaceEvolution.txt");
    FieldsIn.open ("FieldEvolutionIn.txt");
    FieldsOut.open ("FieldEvolutionOut.txt");
    Fluxes.open ("Flux.txt");
    Skin.open ("Skin.txt");
    Permeability.open ("Permeability.txt");
    Permittivity.open ("Permittivity.txt");
    SourceFFT.open ("SourceFFT.txt");

    double xsize=50;
    double ysize=50;
    double zsize=50;

    k=2*pi*Np/(03.0);
    double z=-20.0;
    double x=0.0;
    double y=0.0;
    xpcoord[numcoord]=x;
    ypcoord[numcoord]=y;
    zpcoord[numcoord]=z;
    xscoord[numcoord]=x;
    yscoord[numcoord]=y;
    zscoord[numcoord]=z+40.0;
    numcoord++;

    for (double z=-dzmax;z<=30;z=z+00.1) {

```

```

    xccoord[corecoord]=xcen;
    yccoord[corecoord]=y;
    zccoord[corecoord]=z;
    corecoord++;
}

grid_volume gv = vol3d(xsize, ysize, zsize, divisions);
gv.center_origin();
structure transformer = new structure(gv, eps, pml(3.0));
transformer.set_output_directory(mydirname);
meep_geom::medium_struct my_medium_struct;
my_medium_struct.epsilon_diag.x = 1.0;
my_medium_struct.epsilon_diag.y = 1.0;
my_medium_struct.epsilon_diag.z = 1.0;
my_medium_struct.mu_diag.x=1.0;
my_medium_struct.mu_diag.y=1.0;
my_medium_struct.mu_diag.z=1.0;
my_medium_struct.H_chi2_diag.x=1.0;
my_medium_struct.H_chi2_diag.y=1.0;
my_medium_struct.H_chi2_diag.z=1.0;
my_medium_struct.H_chi3_diag.x=1.0;
my_medium_struct.H_chi3_diag.y=1.0;
my_medium_struct.H_chi3_diag.z=1.0;
my_medium_struct.E_chi2_diag.x=0.0;
my_medium_struct.E_chi2_diag.y=0.0;
my_medium_struct.E_chi2_diag.z=0.0;
my_medium_struct.E_chi3_diag.x=0.0;
my_medium_struct.E_chi3_diag.y=0.0;
my_medium_struct.E_chi3_diag.z=0.0;
my_material_func_data data;
data.with_susceptibility = true;
meep_geom::material_type default_material
=meep_geom::make_dielectric(1.0);
default_material->medium=my_medium_struct;
default_material->user_func = my_material_func;
default_material->user_data = (void *) &data;
default_material->do_averaging = false;
meep_geom::material_type my_user_material
=meep_geom::make_user_material(my_material_func, (void *)&data, false);
geometric_object objects[1];
vector3 center = {0.0, 0.0, 0.0};
vector3 center2 = {0.0, 0.0, 7.5};
double radius = 3.0;
double height = 1.0e20;
vector3 xhat1 = {1.0, 0.0, 0.0};
vector3 yhat1 = {0.0, 1.0, 0.0};
vector3 zhat1 = {0.0, 0.0, 1.0};
vector3 size2 = {wcore, wcore, 45.0};
objects[0] = make_block(my_user_material, center2, xhat1, yhat1,
zhat1, size2);
geometric_object_list g = {1, objects};
meep_geom::absorber_list al= new meep_geom::absorber_list_type;
meep_geom::material_type_list mtl= meep_geom::material_type_list();
mtl.num_items=1;
mtl.items=new meep_geom::material_type;
mtl.items[0]=my_user_material;

```



```

    cout<<"MAIN "<<mtl.num_items<<endl;
    bool use_anisotropic_averaging = false;
    bool ensure_periodicity = false;
    set_materials_from_geometry(&transformer, g, center,
    use_anisotropic_averaging,DEFAULT_SUBPIXEL_TOL,
    DEFAULT_SUBPIXEL_MAXEVAL,ensure_periodicity, default_material,al,mtl);
    anisodisp_materialH anisodispmath;
    //transformer.add_susceptibility(sigma, H_stuff,
    gyrotropic_susceptibility(vec(0.0,0.0,b0), (5.8e-5), (-0.33e-
    2)/(2*3.1459),0.01,GYROTROPIC_SATURATED));
    transformer.add_susceptibility(sigma, H_stuff,
    lorentzian_susceptibility(5.8e-5, (-0.33e-2)/(2*3.1459)));

    fields f(& transformer);
    f.use_real_fields();

    for (double fp=0.0;fp<=(1e9)/f0;fp=fp+(1e4)/f0)
    {
        double yp = 0.0;
        {
            Permeability<<(fp*f0)<<"
"<<f.get_mu(vec(0.0,0.0,0.0),fp)<<endl;
            Permittivity<<(fp*f0)<<"
"<<f.get_eps(vec(0.0,0.0,0.0),fp)<<endl;
        }
    }

    double fcen = (5e9)/f0; // ; pulse center frequency
    double df = 0.999999*((10e9)/f0); // ; df
    //continuous_src_time src(cdouble(fcen,df));
    gaussian_src_time src(fcen,df);

    for (double fp=0.0;fp<=(10e9)/f0;fp=fp+(1e6)/f0)
    {
        double yp = 0.0;
        {
            SourceFFT<<fp<<" "<<src.fourier_transform(fp).real()<<"
"<<src.fourier_transform(fp).imag()<<endl;
        }
    }

    for (int i=0;i<numcoord;i++)
    {
        theta=atan(-xpcoord[i]/ypcoord[i]);
        const volume vsrcl =volume(vec(xpcoord[i],ypcoord[i],zpcoord[i]),
        vec(xpcoord[i],ypcoord[i],zpcoord[i]));
        {
            f.add_volume_source(Hz, src, vsrcl, cdouble(amplitude,0));
        }
    }

    cout<<"Stepping"<<endl;
    f.step();f.step();f.step();f.step();f.step();
    cout<<"Okay"<<endl;
    volume vxy=volume(vec(-xsize,-ysize,0),vec(xsize,ysize,0));

```

```

volume vxz=volume(vec(-xsize,0,-zsize),vec(xsize,0,zsize));
volume vyz=volume(vec(0,-ysize,-zsize),vec(0,ysize,zsize));

int stop=0;

for(int i=1;i<=1000000;i++)
{
    if(!stop)
    {f.step();}
    if (stop)
    {i=1000001;}
    if (i<=2000)
    {
        for (double z=-dzmax;z<=dzmax;z=z+1/(2*divisions))
        {
            monitor_point pin;
            f.get_point(&pin, vec(xcen,ycen,z));
            cdouble E1i = pin.get_component(Ex);
            cdouble E2i = pin.get_component(Ey);
            cdouble E3i = pin.get_component(Ez);
            cdouble D1i = pin.get_component(Dx);
            cdouble D2i = pin.get_component(Dy);
            cdouble D3i = pin.get_component(Dz);
            cdouble H1i = pin.get_component(Hx);
            cdouble H2i = pin.get_component(Hy);
            cdouble H3i = pin.get_component(Hz);
            cdouble B1i = pin.get_component(Bx);
            cdouble B2i = pin.get_component(By);
            cdouble B3i = pin.get_component(Bz);
            FieldsIn<<i<<" , "<<z<<" , "<<H1i.real() <<" ,
"<<H1i.imag()<<" , "<<H2i.real()<<" , "<<H2i.imag()<<" ,
"<<H3i.real()<<" , "<<H3i.imag()<<" , "<<B1i.real()<<" ,
"<<B1i.imag()<<" , "<<B2i.real()<<" , "<<B2i.imag()<<" ,
"<<B3i.real()<<" , "<<B3i.imag()<<" , "<<E1i.real()<<" ,
"<<E1i.imag()<<" , "<<E2i.real()<<" , "<<E2i.imag()<<" ,
"<<E3i.real()<<" , "<<E3i.imag()<<" , "<<D1i.real()<<" ,
"<<D1i.imag()<<" , "<<D2i.real()<<" , "<<D2i.imag()<<" ,
"<<D3i.real()<<" , "<<D3i.imag()<<endl;
        }

    }

    if((i==(2000)))
    {
        stop=1;
    }

}

cout<<"Skin Effect"<<endl;
for (double y=-05.0;y<=05.0;y=y+00.001)
{
    monitor_point pin;
    f.get_point(&pin, vec(xcen,y,zcen));
    cdouble E1i = pin.get_component(Ex);

```

```

    cdouble E2i = pin.get_component(Ey);
    cdouble E3i = pin.get_component(Ez);
    cdouble D1i = pin.get_component(Dx);
    cdouble D2i = pin.get_component(Dy);
    cdouble D3i = pin.get_component(Dz);
    cdouble H1i = pin.get_component(Hx);
    cdouble H2i = pin.get_component(Hy);
    cdouble H3i = pin.get_component(Hz);
    cdouble B1i = pin.get_component(Bx);
    cdouble B2i = pin.get_component(By);
    cdouble B3i = pin.get_component(Bz);
    Skin<<H1i.real() <<" , "<<H1i.imag()<<" , "<<H2i.real()<<" ,
"<<H2i.imag()<<" , "<<H3i.real()<<" , "<<H3i.imag()<<" ,
"<<B1i.real()<<" , "<<B1i.imag()<<" , "<<B2i.real()<<" ,
"<<B2i.imag()<<" , "<<B3i.real()<<" , "<<B3i.imag()<<" ,
"<<E1i.real()<<" , "<<E1i.imag()<<" , "<<E2i.real()<<" ,
"<<E2i.imag()<<" , "<<E3i.real()<<" , "<<E3i.imag()<<" ,
"<<D1i.real()<<" , "<<D1i.imag()<<" , "<<D2i.real()<<" ,
"<<D2i.imag()<<" , "<<D3i.real()<<" , "<<D3i.imag()<<endl;
    }

    cout<<"SpaceEvolution"<<endl;
    for (double z=-dzmax;z<=dzmax;z=z+1.0)
    {
        cdouble Im=compute_Im(f,z);
        cdouble Ie=compute_Ie(f,z);
        cdouble Vm=compute_Vm(f,z);
        cdouble Ve=compute_Ve(f,z);
        Space <<Im.real()<<" , "<<Im.imag()<<" , "<<Vm.real()<<" ,
"<<Vm.imag()<<" , "<<Ie.real()<<" , "<<Ie.imag()<<" , "<<Ve.real()<<" ,
"<<Ve.imag()<<endl;
        //Im , Vm , Ie , Ve
    }

    /* f.step();
    f.output_hdf5(Hx,f.gv);
    */

    Time.close();
    Space.close();
    FieldsIn.close();
    FieldsOut.close();
    Fluxes.close();
    return 0;
}

```

## 138

[illegible]

```

t0=1/f0;%0.33e-12 (s)
mu0=4*pi*(1e-7);% (H/m)
eps0=8.854187817e-12;% (F/m)
I0=1; %(A)
E0=I0/(a0*eps0*c0);%Electric Field
D0=I0/(a0*c0);%Electric Displacement Field
B0=I0/(a0*eps0*c0*c0);%Magnetic Field
H0=I0/(a0);%Magnetizing Field
sigmaD0=(epsr*eps0*c0)/a0;

hold on;

subplot(4,1,1)
hold on;
T=t0;
Fs=1/T;
L=45;
L=2^nextpow2(L);
% NFFT=2^nextpow2(L);
% FHxi=(fft(Hx(1:L,5)*H0,NFFT)/L)();
% FHxi(2:end-1)=
% f=Fs/2*linspace(0,1,NFFT/2+1);

FHxi=(fft(Hx(1:L,2)*H0,L));
FHxi=FHxi(1:L/2+1);
%FHxi(2:end-1)=2*FHxi(2:end-1)
f=Fs*(0:L/2+1);
f=f';

FHxo=(fft(Hx(1:L,12)*H0,L));
FHxo=FHxo(1:L/2+1);
%FHxo(2:end-1)=2*FHxo(2:end-1);

Gamma=log(FHxo./FHxi)/(-(10/80)*(2e-3));

subplot(3,1,1)
hold on;%plot(mag3(mag(A13,A14),mag(A15,A16),mag(A17,A18)));%E
plot(f(2:L/2+1),real(Gamma(2:L/2+1)));
xlabel('Frequency (Hz)')
ylabel('\alpha (Np.m^-1)');
axis([0 5e11 1.32e5 1.38e5])

subplot(3,1,2)
plot(f(2:L/2+1),abs(imag(Gamma(2:L/2+1))));
ylabel('\beta (rad.m^-1)');
xlabel('Frequency (Hz)')
axis([0 5e11 1e4 1.3e4])

subplot(3,1,3)
plot(f(2:L/2+1),f(2:L/2+1)./abs(imag(Gamma(2:L/2+1))));
ylabel('vp (m.s^-1)');
xlabel('Frequency (Hz)')
axis([0 5e11 0 5e7])
% X = 1/(4*sqrt(2*pi*0.01))*(exp(-t.^2/(2*0.01)));

```

```

T=t0;
Fs=1/T;
L=45;
NFFT=2^nextpow2(L);
FEx=fft(Ex(1:L,2)*E0,NFFT)/L;
f=Fs/2*linspace(0,1,NFFT/2+1);
FHx=fft(Hx(1:L,2)*H0,NFFT)/L;
f=Fs/2*linspace(0,1,NFFT/2+1);
Z=FEx./FHx;

subplot(2,1,1)
hold on;%plot(mag3(mag(A13,A14),mag(A15,A16),mag(A17,A18)));%E
plot(f(2:NFFT/2+1),2*abs(Z(2:NFFT/2+1)));
xlabel('Frequency (Hz)');
ylabel('|Z_w (Ohm)|');
axis([0 5e11 3.3e4 3.45e4])

subplot(2,1,2)
plot(f(2:NFFT/2+1),angle(Z(2:NFFT/2+1))*(180/pi));
ylabel('\Theta Z_w (deg)');
xlabel('Frequency (Hz)');
axis([0 5e11 170 190])

XLm=(imag(Gamma(1:NFFT/2+1).*Z(1:NFFT/2+1)));
Gm=(real(Gamma(1:NFFT/2+1)./Z(1:NFFT/2+1)));
Rm=(Gm')*(-1).*(2*pi*f);%Reluctance
XCm=(imag(Gamma(1:NFFT/2+1)./Z(1:NFFT/2+1)));

subplot(4,1,1);
plot(f,(XLm(1:NFFT/2+1)));
ylabel('XLm(H/m)');
xlabel('Frequency (Hz)');
%axis([0 1e11 -5e9 5e9])

subplot(3,1,1);
plot(f(2:NFFT/2+1),(Gm(2:NFFT/2+1)));
ylabel('Conductance GL (S/m)');
xlabel('Frequency (Hz)');
axis([0 5e11 -8.5 -7.5])

subplot(3,1,2);
plot(f(2:NFFT/2+1),(Rm(2:NFFT/2+1)));
ylabel('Reluctance Rmskin (1/H.m)');
xlabel('Frequency (Hz)');
axis([0 5e11 0 3e13])

subplot(3,1,3);
plot(f(2:NFFT/2+1),(XCm(2:NFFT/2+1)));
ylabel('Susceptance XCL (S/m)');
xlabel('Frequency (Hz)');
axis([0 5e11 0 1])

```

## **VITA**

Muhammad Shamaas completed his Bachelor of Science in Electrical Engineering from Lahore University of Management Sciences (September 2014 - June 2018); with specialization in Power Engineering. He is currently enrolled as a Master of Science scholar in the Electrical Engineering program (September 2018 – June 2021) at The University of Engineering and Technology Lahore. His main subjects include Electric Drives Control, Power Electronic Converters and Advanced Power Systems. He has worked as a Research Assistant in the RF and microwave laboratory at Lahore University of Management Sciences (February 2018 – June 2018). He also worked as a Research and Development Engineer in the Power Laboratory at University of Lahore (February 2021 – September 2021).

